Bachelor's project

NTNU
Norwegian University of Science and Technology
Faculty of Engineering
Department of Energy and Process Engineering

Håkon Guddingsmo, Petter Martinussen and Daniel Stjernen

Energy Optimization for Lithium-ion Electrode Manufacturing Processes

Bachelor's project in Renewable Energy
Supervisor: Asanthi Jinasena
Co-supervisor: Odne Stokke Burheim
May 2021

NTNU
Kunnskap for en bedre verden

Håkon Guddingsmo, Petter Martinussen and
Daniel Stjernen

Energy Optimization for Lithium-ion Electrode Manufacturing Processes

Bachelor's project in Renewable Energy
Supervisor: Asanthi Jinasena
Co-supervisor: Odne Stokke Burheim
May 2021

Norwegian University of Science and Technology
Faculty of Engineering
Department of Energy and Process Engineering

NTNU
Norwegian University of
Science and Technology

Preface

One of the biggest expanding businesses is currently the electrification of the automotive sector. It is a paramount objective in achieving the goals concerning global warming. For this, sustainable and reliable batteries are important, and an increase in demand is inevitable for this decade. The main focus of this thesis is to explore areas of enhancement within manufacturing of lithium-ion batteries, optimizing the energy usage in the overall production process.

The thesis is written in collaboration of three students: Håkon Guddingsmo, Petter Martinussen and Daniel Stjernen. It is the final assignment of the three year study program *Bachelor in Engineering, Renewable Energy* at the Norwegian University of Science and Technology (NTNU), Department of Energy and Process Engineering. It accounts for 100% of the final grade in the subject TFNE3001 - Bachelor Thesis Renewable Energy.

The group would like to thank our supervisor, Postdoctoral Fellow Asanthi Jinasena, for the wholehearted support, remarkable expertise and weekly guidance during the writing of the thesis. We would also like to express our gratitude to Professor Odne Stokke Burheim for providing essential instructions and management, as well as introducing the group to key personnel working on battery science. Further, the group want to thank all the participants of the weekly seminar *NTNU Battery Lunch and Learn - Free of Charge* for insightful presentations on various subjects within the field of batteries. A special thanks is also given to family and friends for their support and motivational words during the semester.

Trondheim 20.05.2021

Håkon Guddingsmo

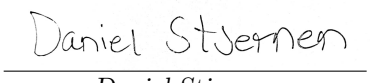

Daniel Stjernen

Petter Martinussen

Abstract

As today's society is gradually shifting towards renewable transport methods such as electric vehicles, battery production is forecasted to grow significantly. This thesis seeks to evaluate the energy consumption of the lithium-ion battery manufacturing process and address ways to improve the energy efficiency of the current manufacturing process. This also includes assessing the potential of emerging technologies within the field.

The most energy demanding steps in a conventional manufacturing process are the electrode drying process and the dry room. These areas are the main focal points for this study. The evaporation energy and drying time of the electrode drying process is simulated for different drying techniques and tested based on different initial conditions using a mathematical model. The process simulation of the required energy for airflow heating and cooling is modeled using Aspen HYSYS. Further, the dry room is modeled using Aspen Plus based on different ambient conditions. Additionally, the potential for using maximum energy recovery (MER) networks based on the pinch approach is investigated. An estimate is made towards the equivalent production of the setups tested for and further, the ratio between energy consumption and production capacity is evaluated.

The conventional convective drying process is modeled to have a load of around 2591 kW, this corresponds to an energy to produced cell capacity ratio of 32.7 Wh/Wh, and serves as the basis for comparison for the remaining designs. Radiation drying is by comparison slightly higher with a ratio of 34.4 Wh/Wh. The MER-network designs range from 18-20 Wh/Wh, implying that this design approach is highly viable compared to conventional setups. These MER-networks can also be further improved by integrating heat pumps around the pinch of the system.

The dry room energy requirements are also modeled with a resulting load of 399 kW. This correlates to a total energy to produced capacity ratio of close to 5 Wh/Wh, depending on input conditions. Alternative production methods such as semi-solid electrode structures are able to bypass the need for electrode drying and thus the majority of the energy consumption. These methods also hold potential, and the combined energy requirement is estimated to be around 10-20 Wh/Wh. Laser drying is also discussed as a promising alternative due to the high degree of control of the drying rate throughout the process.

List of Symbols

Symbol	Unit	Description
A	m^2	Area
A_h	m^2	Heat transfer area of heat exchanger
A_l	m^2	Transfer area liquid side
A_g	m^2	Transfer area gas side
C	wt%	Weight fraction of solvent
C_p	$J/kg \cdot K$	Specific heat of air
C_{p_a}	$J/kg \cdot K$	Specific heat of dry air from desiccant system
C_{p_s}	$J/kg \cdot K$	Specific heat of solvent
D	m^2/s	Diffusion coefficient
E	J	Activation energy
E_{drying}	J	Total energy consumption of drying process
E_{drying_a}	J	Energy requirement of air heating
E_{drying_s}	J	Total energy from solvent evaporation
$E_{dryroom}$	J	Total energy consumption of dry room
h	m	Thickness of film
h_t	$W/m^2 \cdot K$	Heat transfer coefficient
h_d	$W/m^2 \cdot K$	Heat transfer coefficient desiccant system
h_g	$W/m^2 \cdot K$	Heat transfer coefficient gas side desiccant system
h_l	$W/m^2 \cdot K$	Heat transfer coefficient liquid side desiccant system
L	-	Characteristic length
Le	-	Lewis number
M_s	g/mol	Molecular weight of solvent
$\dot{m}_a$	m/s	Mass flow rate of air
$\dot{m}_{evap.}$	kg/m^2s	Evaporation rate
$\dot{m}_g$	kg/h	Dry room air flow rate
$\dot{m}_l$	kg/h	Liquid desiccant flow rate
Pr	-	Prandtl number
P_a	Pa	Pressure of air
P_c	W	Total cooling load
P_h	W	Total heating load
P_s	Pa	Equilibrium partial pressure of solvent
P_{sol}	Pa	Solvent vapor pressure
P_0	Pa	Vapor pressure of pure solvent
Q	kJ/m^2	Evaporation energy
$\dot{Q}$	W	Heat load
$\dot{Q}_c$	W/m^2	Heat transfer rate
$\dot{q}_{in}$	J/m^2	Heat transfer rate
$\dot{q}_{in,con}$	J/m^2	Heat transfer rate convection

Symbol	Unit	Description
R	$\mathrm{J/kmol \cdot K}$	Universal gas constant
R_T	W/K	Total thermal resistance
Se	-	Schmidt number
T	K	Temperature of film
T_a	K	Temperature air
T_a	K	Start temperature air
$T_\mathrm{a,rad}$	K	Temperature air for radiation heating
T_b	K	Absolute surface temperature
T_b	K	Temperature of heat source
T_gi	K	Temperature of ambient air in desiccant system
T_go	K	Temperature of air at absorber gas outlet desiccant system
T_li	K	Inlet temperature of desiccant system
T_s	K	Temperature surface
T_sur	K	Surrounding temperature
t	s	Time
t_f	s	Total drying process time
t_drying	s	Total drying process time
U	$\mathrm{W/m^2 \cdot K}$	Heat transfer coefficient
V_a	m/s	Air velocity
V_p	$\mathrm{m^3}$	Volume of solid
V_s	$\mathrm{m^3}$	Volume of solvent

Symbol	Unit	Description
ϵ	-	Emissivity
γ	-	Constant empirical value
κ_c	$\mathrm{W/m^2 \cdot K}$	Heat transfer coefficient convection
κ_m	ms	Mass transfer coefficient
λ	kJ	Latent heat of evaporation of solvent
λ_W	kJ	Latent heat of evaporation of water
λ_NMP	kJ	Latent heat of evaporation of NMP
λ_a	$\mathrm{W/m \cdot K}$	Thermal conductivity
μ	$\mathrm{Ns/m^2}$	Viscosity of air
ρ_a	$\mathrm{kg/m^3}$	Density of air
ρ_f	$\mathrm{kg/m^3}$	Film density
ρ_p	$\mathrm{kg/m^3}$	Bulk density of the solid
ρ_s	$\mathrm{kg/m^3}$	Density of solvent
σ	$\mathrm{W/m^2 \cdot K^4}$	Stefan-Boltzmann constant
ϕ	%	Relative humidity of air
Φ_p	Vol%	Polymer volume fraction
Φ_s	Vol%	Solvent volume fraction
χ	-	Flory Huggins interaction parameter

Chemical symbol	**Description**
$CaCl_2$	Calcium chloride
LiBr	Lithium bromide
LiCl	Lithium chloride
$LiNiMnCoO_2$	Nickel manganese cobalt oxide (NMC622)
$LiCoO_2$	Lithium cobalt oxide
NCA	Nickel cobalt aluminium oxide
NMC	Nickel manganese cobalt oxide
NMP	N-methyl-2-pyrrolidone
PVDF	Polyvinylidene difluoride
R-22	Chlorodifluormethane
R-134a	Tetra-fluor-ethane
R-600a	Isobuthane

List of Terms and Abbreviations

Term	Definition
Active materials	The materials involved in a reaction that produces electricity
All-solid state	An electrochemical cell that utilizes a solid electrolyte
Ambient conditions	Conditions such as temperature that are external to the system regarded
Assembly line	A continuous stream of production
Batch mixers	Machines that mix a set quantity of substance collectively
Binder migration	The movement of binder materials in a slurry during drying
Calendaring	The process of applying mechanical pressure to a material in order to change its properties
Capillary effect	Intermolecular force between a solid and fluid
Carbon conductive additive	Carbon additive that is able to conduct electricity
Cathode	Part of the battery where reduction takes place
Central pin	A type of rod that material can be winded around
Coating	The process of applying a slurry to a conductive foil
Condensation energy	The energy required for a gas to change into a liquid-phase
Conductive foil	Substrate of electrode that can conduct electricity from the electrode to an external circuit
Cracking	The occurrence of fractures or hole formation
Current collectors	Part of the battery that collects and transports electrons from the electrodes
Cylindrical cell	A type of battery cell that is cylindrical in shape with poles on top and bottom
Dry room	A room that satisfies certain conditions, such as humidity and cleanness
Electroconductive particles	Small particles of a conductive material
Electrode	A conductor that serves as a collective term for the anode and cathode
Electrolyte	Part of the battery containing free ions
End-of-line testing	Testing and quality check at the end of production
Energy density	Energy per unit of volume
Evaporation energy	Latent energy required to evaporate a substance
Extrusion die	A cross-section channel that alters the shape of a material
Formatting stage	Part of the production, where the cells are charged and discharged
Galvanic cell	Cell that generates an electrical potential from a chemical reaction
Half-reaction	Either side of the reaction in a redox reaction

Term	Definition
Intercalation	Particles of a substance integrated in another material with layered structures
Isothermal expansion	Expansion with constant temperature
Laser ablation	Laser irradiation of a substance that results in removal or evaporation of mass
Lithiated substance	Substance containing lithium
MER-networks	A network using heat exchanger connections based on pinch approach to optimize energy efficiency
Oxidized	A chemical reaction resulting in the substance loosing electrons
Particle suspension	Small solid particles suspended within a fluid
Pinch approach	Design approach based on the minimum temperature difference
Porosity	Defining property for the structure of a solid, determining cavities within the material
Pouch cell	A battery cell structured like a pouch with tabs on top
Prismatic cell	Often a large cell with sandwiched and rolled electrode structure
Reactants	The substances participating in a chemical reaction
Redox reaction	Chemical reaction with oxidisation and reduction
Reduction	Chemical reaction resulting in the substance gaining electrons
Refrigeration cycle	A closed thermodynamic cycle transferring heat from low temperatures to high temperatures by inducing work
Roll pressing	Using rollers to apply pressure to, and change, the characteristics of a material
Saturated liquid	A substance that is composed of pure liquid
Saturated vapor	A substance that is composed of pure vapor
Secondary batteries	A rechargeable battery
Semi-solid state	Battery technology using solid particles suspended within the electrode
Sintering	Simultaneously applying heat and pressure to a material in order to change the characteristics
Slurry	The mixture of active materials, solvent and binder
Solvent filtration	The removal and collection of solvent from an airflow
Sonifications	Energy transfer with the use of sound
Sustainable Development Scenario	Description of the energy sector as a whole, and measures that can be made in order to achieve climate goals
Electrolytic cell	Conversion of electrical energy into chemical energy
Vapor-liquid mixture	The equilibrium between liquid- and vapor-phase
Vibrating table	A machine that induce vibrations in a material
Wet coating techniques	Coating that results in a completely wet surface
Winding mandrel	A cylindrical object that material can be winded around
Working fluid	A fluid or gas that transfers mechanical energy

Abbreviation	Meaning
CPU	Central Processing Unit
EOL	End-Of-Line
EV	Electrical Vehicle
FDM	Finite-Difference Method
FTCS	Forward Time Central Space
LIB	Lithium-Ion Battery
LMTD	Logarithmic mean temperature difference
MER	Maximum Energy Recovery
Redox	Reduction-Oxidation
USD	United States Dollars

List of Figures

List of Tables

Contents

1 Introduction

The implementation of electricity into society have drastically helped improve quality of life for mankind. Most would agree that it has become such an integrated part of the standard of living, that it is difficult to imagine a world without it. The introduction of secondary batteries also made electricity into a reliable source of portable power, and the world has since experienced a gradual shift from fossil fuels to electricity. Today, electric vehicles are considered a vital step in reducing greenhouse emissions, with plans such as the Sustainable Development Scenario and EV30@30 Campaign [1] being set into motion. This shift has rapidly increased the global demand for low-cost and energy efficient batteries.

How to sufficiently supply the increase in market demand has come into focus, and research on carbon friendly and cost efficient production methods are being prioritised. Companies within the automobile sector are showing an interest in transitioning to electric vehicles, which is set to dominate the lithium-ion battery market at the end of the decade [1]. Currently, the most energy consuming stages in a standardized battery manufacturing process is the drying of the electrodes, and the subsequent dry room needed for assembly [2]. Thus, the main focus for optimization lay within these two stages.

One of the propositions for convective drying involves the addition of a regenerator for the electrode drying process, as well as the installation of a heat pump between the drying process and dry room. Another possible solution considers a technology utilizing high viscosity processing, which consists of semi-solid electrodes, in order to pass the drying stage entirely [3].

The thesis is divided into sections that contribute towards investigating the focal point of the project. The background chapter describes battery composition and the individual steps of current battery manufacturing, as well as fundamental concepts of battery production. Additionally, the underlying equations used for modeling are presented and explained. The section references relevant literature, and looks at previous research related to alternative technologies such as laser drying and semi-solid electrode structures.

Further, the method chapter shows how the individual parts of the production process was modeled and how the results were found. This includes the initial conditions and some of the assumptions the models are based on. Models were created for the evaporation process, the convective airflow heating and cooling energy, dry room system and maximum energy recovery networks. The results from the models are presented and combined to find total power and energy consumption. These results are further investigated and compared in the discussion section. Here, all assumptions made are presented and their significance is described. In addition, the different results are also compared to one another. The most significant assessments from the discussion are presented in the conclusion of the report. Finally, ideas for future areas of interest and further work are highlighted in the future work section.

2 Background

This section covers the fundamentals, and the underlying theory for the thesis.

2.1 Battery technology

A conventional battery is a source of power that consists of either one singular or multiple electrochemical cells. There exists many types of such cells. However, they are all based on the same fundamental principle. A voltage difference between two oppositely charged poles creates a potential for electrical energy to be transferred. When the electrochemical cell is connected to an external circuit, the voltage potential between the two poles create an electric current, which can be used for numerous purposes. Essentially, an electrochemical cell is chemically stored energy which can be released as electric energy [4].

An electrochemical cell is based on the chemical reaction known as a reduction-oxidation (redox) reaction. A redox reaction is when two chemical reactions occurs simultaneously due to the difference in electrochemical potential between them. Here, one of the reactions lose an amount of electrons and become oxidized. The other reaction gains the same amount of electrons and become reduced. The transfer of electrons from one reaction to another, can be utilized in the form of electrical energy [4].

To make use of this energy, transfer of electrons must be allowed through an electric conductor. The electric conductor is connected to each of the half-reactions of the redox reaction. The half-reactions occur in their own cell. Each cell consists of an electrolyte and an electrode. The electrolyte allows ions to move freely. The electrode is the electronic-ionic junction which connects the electric conductor to the electrolyte, and is where the half-reaction occurs. The electrode is explained more thoroughly in Section 2.1.3. Each of the cells work as a pole for the electrochemical cell, and the properties of the reaction in each cell decides whether the cell is giving away electrons, or receiving them. In other words, the properties decide the polarity of the cell [4].

2.1.1 Battery uses

Batteries have gradually become the standardized form of portable energy. They see application in a multitude of shapes and sizes, most notably in technological instruments such as phones and laptops. Additionally, they have begun to see widespread commercial use in areas such as hardware tools. Larger battery packs are also beginning to see a wider appeal in various applications within the medical, construction and automotive sectors [1].

Electrical vehicles (EVs) have recently gained traction due to their many benefits compared to internal combustion engine vehicles. EVs have proven to be more energy efficient and emit less local pollution and noise, without the reliance on fossil-based fuels. Additionally, EVs are a potential enabler for cost reduction within the field of battery technology, which could support further development in other battery-based sector for a society based on clean energy [1].

2.1.1.1 The battery market

Battery manufacturing have been a heavily researched topics in the last couple years. Technologies have improved, and costs have dropped as new production methods and materials have been introduced. Using EVs as reference; the cost basis for battery packs in 2019 averaged

to 156 USD per kilowatt-hour, from the 1100 USD per kilowatt-hour price tag in 2010 [1]. The automotive industry has been the target for a large portion of new and upcoming battery manufacturers. It is a market with a seemingly screaming demand, which is likely to be be dominated by lithium-ion batteries (LIB) for the remainder of the decade [1].

2.1.1.2 Future outlook

According to the Sustainable Development Scenario, and EV30@30 Campaign [1], the EV market share is targeted to 30% by the year 2030. This scenario project a 36% annual growth in EVs, reaching 245 million vehicles in 2030, amounting to 30 times today's level. Furthermore, the EV battery capacity is set to increase from today's 170 GWh to between 1.5-3 TWh in 2030. Compared to other battery-reliant sectors, the Sustainable Development Scenario forecast the automotive industry accounting for 89% of the overall battery demand in 2030 [1].

2.1.2 Lithium-ion batteries

There are currently two categories of batteries, primary batteries and secondary batteries. A primary battery is a galvanic cell that delivers electrical power when it is connected to a closed circuit. A secondary battery serves the same purpose. However, the chemical process inside the battery can be reversed based on the electrolytic cell principle. Functionally speaking, this means the battery can be recharged after use [4].

A secondary battery is therefore also known as a rechargeable battery. In contrast to the primary battery, which exhaust its reactants into products during its lifetime, the lifetime of a rechargeable battery is much longer, limited by only a few factors. The reactants of a rechargeable battery, known as the active materials which are further described in Section 2.1.3.1, are fueled from outside the electrochemical cells and the products of the reaction are removed continuously [4].

LIBs are secondary batteries which dominate much of the current global battery market. They are known for their high specific energy and energy density, making them remarkably viable in most electronics and electric vehicles [5]. However, LIBs are expensive to manufacture. Therefore, continuous research and development is attempting to lower the overall costs.

A LIB is designed around the strong reactive forces of lithium. It is a highly reactive material that binds to other materials easily. Therefore, the electrodes in the battery are made of materials which are easy for lithium to intercalate into. When the battery is charged, electrons pass from the cell that contains lithium to the opposite cell. This creates a strong imbalance in the polarity of the battery, which causes the lithium-ions to shift over to the newly negatively charged pole, through a membrane, which only allows the passing of ions. When the battery is then used in an instrument, electrons pass over to the positively charged pole through an external circuit, which creates an electric current. The lithium-ions travel back through the membrane to the positively charged electrode, and intercalates with the material on that side [5].

Battery cells are primarily produced in three different formats. These are cylindrical, prismatic and pouch cells. Section 2.1.3.7 describes the different battery chemistries. Most manufacturers of electric vehicles utilize the pouch cell due to its high energy density and efficiency, making it lighter in terms of weight. The pouch cell consist of a stack of multiple sheets of anode, separator and cathode as shown in Figure 2.1. They are then welded and heat sealed with an aluminium-laminate film [6].

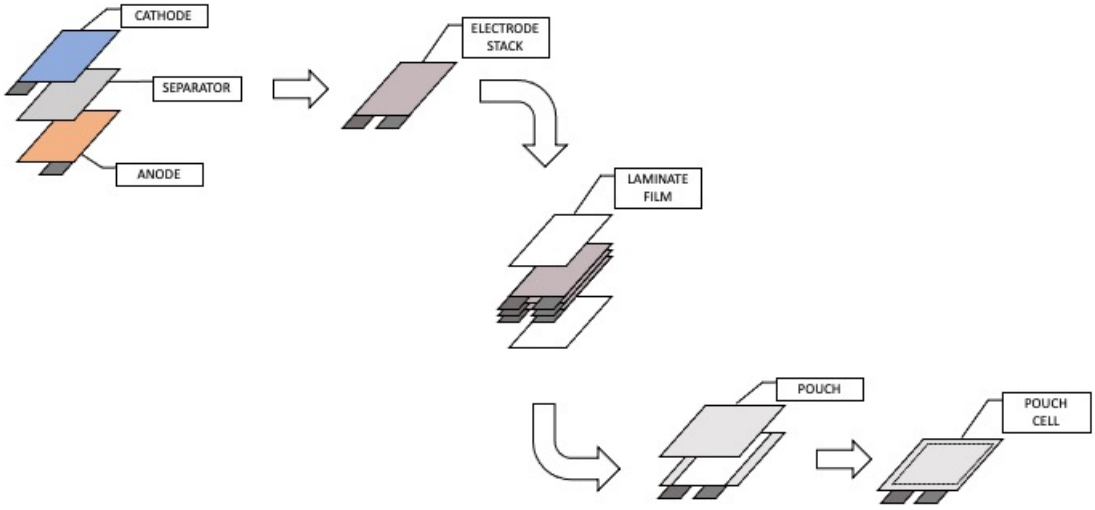

Figure 2.1: *Stacking of positive and negative electrodes with separators in a pouch cell. Pouch is then heat sealed in laminated film. Figure is adapted from [7].*

2.1.3 Battery materials

The electrodes in a LIB consist of a combination of active and inactive materials. The type of material vary between manufacturers as it is dependent on production technique. However, the base materials of the electrode remains roughly the same [5].

2.1.3.1 Active materials

The materials that electrodes consists of are referred to as active materials. The active materials in a LIB are the materials of which the ions and electrons are being transferred between. Active materials are not consumed in the processes of charging and discharging. The cathode consists of a lithiated substance, an example being lithium cobalt oxide ($LiCoO_2$), while the anode usually consist of graphite. The polarity of the electrodes is in reference to a battery discharge. An important note when designing a LIB is that under no circumstances can more than 50% of the lithium be transferred from the cathode, as it would ruin the structure of the electrode [5].

2.1.3.2 Carbon black

Carbon black is a special carbon conductor additive in the electrode. The amount of additive varies based on manufacturer. It is used to ensure that the active material is electrically connected to the conductor [5].

2.1.3.3 Binder

Binders refer to an inactive material in the electrode that creates cohesion. The binder also increase adhesion to the current collector, helping the electrode retain its structure. It does this by forming in the shape of strings which holds the coating together. A traditional binder used for LIB is polyvinylidene difluoride (PVDF) [5].

2.1.3.4 Solvent

The solvent is an inactive material that is added during mixing of the electrode materials, and then later extracted by drying. The solvent aids in the mixing process, lowering viscosity and distributing the materials more thoroughly. The name of the final mixture, consisting of the active and the inactive materials, is called slurry [5].

Due to PVDF not being soluble in water, N-methyl-2-pyrrolidone (NMP) can be used as an organic solvent. However, due to NMP's toxic and environmentally harmful nature, it must be removed during the drying process. This is further explained in Section 2.6.2. This problem mainly applies to the cathode, as water is commonly used as solvent for the anode [5].

2.1.3.5 Separator

A separator is used to avoid electrical current flowing between anode and cathode, which would cause short circuit and a potential thermal runaway. Commercial separators have a melting point of 135-160°C, and a ceramic coating can be used for greater temperature stability [5].

2.1.3.6 Electrolyte

An electrolyte is a substance primarily used for transporting ions between the electrodes. For a LIB, the electrolyte is characterized by three material classes and their combination. These classes are the conducting salts, the organic aprotic solvents and the additives. The electrolyte also need to address functionality, safety and economics. For instance, it needs to deliver high conductivity across a wide temperature range, show stability after thousands of charge cycles, and be chemically compatible with the electrode [5].

2.1.3.7 Battery chemistry

As the anode is typically made of graphite, the battery can be categorized by its cathode chemistry. The most notable are nickel manganese cobalt oxide (NMC) and nickel cobalt aluminium oxide (NCA). The abbreviation can be followed by a set of numbers signifying the atomic structure used for the cathode chemistry. NMC622 therefore has an atomic structure of $LiNi_{0.6}Mn_{0.2}Co_{0.2}O2$ [5].

NMC was the most common cathode chemistry used in electric vehicles in 2020 [1]. It is also preferred for power tools and electric bikes due to its high specific energy. Increasing the amount of nickel increases the energy density [1].

NCA offer similar characteristics as NMC, although with a lower nickel content. The trade off being lower energy density for longer cycle life and better stability [5]. NMC111 is considered the standard in NMC. However, it is likely that the future generation of LIB technology will use either low nickel NCA or NMC811 cathodes [1]. The capacity of a single cell of NMC111 and NCA is estimated by Nelson et al. [8] to be 108 Wh, while NMC811 is estimated to 109 Wh.

2.1.3.8 Binder migration and cracking

Some of the complications that can arise during the drying of electrodes include binder migration and cracking. These phenomena can occur when utilizing an aqueous slurry solution. Binder migration can also occur with electrodes using other solvents of organic composition, such as

NMP, however this is less common. Binder migration means that as the solvent evaporates, and the film thickness decreases, the binder and active material are brought to the top of the electrode by the means of capillary transport forces. The consequence of this is that the binder, which is supposed to hold the electrode together, is transported away from the substrate. This results in a lower adhesion force between the slurry and the electric conductive film. Cracking is another phenomenon that can occur with a particularly high drying rate and drying temperature, and the severity of the cracks is also shown to worsen with an increase in the electrode thickness. Cracks can then form in the structure of the electrode, which leads to a reduction in its efficiency. Cracks are formed during the capillarity force driven phase of the electrode drying. [9, 10, 11].

2.2 Lithium-ion battery manufacturing process

The production of LIB contains several subsequent steps where the end result ensures a battery that satisfies the manufacturer's standard. The following sections describe the process steps, and is designed to follow each other sequentially in an assembly line. The process could differ between factories in regards to battery design and drying method, but the overall principles and order remains the same. In the following sections, a pouch cell design is chosen as reference, using a convective solvent drying method. The flow chart in Figure 2.2 depicts a standardized manufacturing process. All stages from separation to degassing are performed in the dry room, which is further explained in Section 2.5.

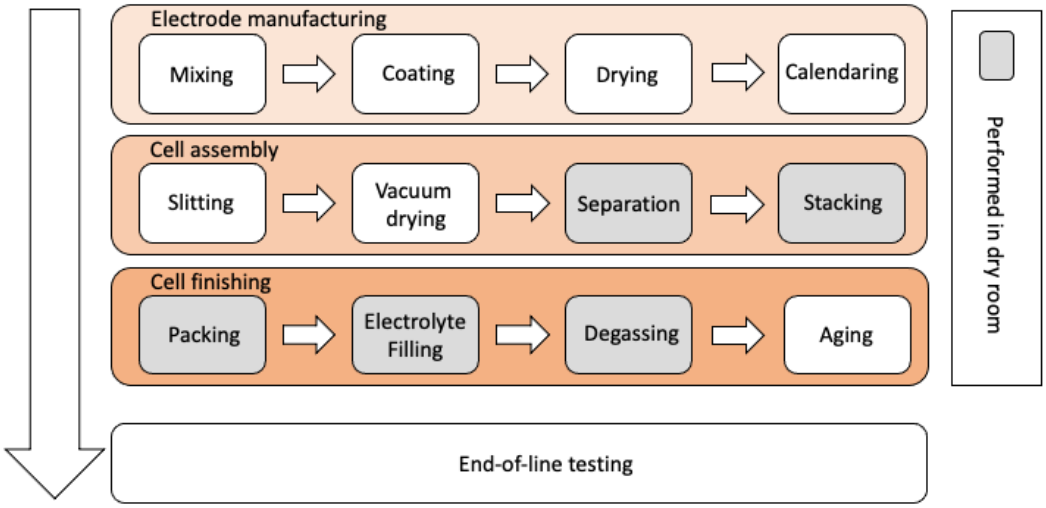

Figure 2.2: *Flowchart for a standardized battery manufacturing process. The steps of the process that are colored gray is performed in the dry room. Figure is inspired by [2].*

2.2.1 Current manufacturing process

There are currently several different manufacturing processes being practiced and researched such as convective drying, radiation drying and semi-solid technology. Out of these, convective drying is the most conventional. The semi-solid principle is an emerging technology and is further explained in Section 2.3.1. However, wet coating techniques and liquid electrolytes are still the most widespread approach in industrial production facilities [3, 2]. The following chapters detail the steps used in a generalized production process.

The energy requirement for the different manufacturing steps varies by a considerable margin. Jinasena et al. [2] estimates that the drying process and the dry room process accounts for 96% of the total energy used in production, meaning only 4% of energy is needed for the remaining production steps. An illustration of this is shown in Figure 2.3. Generally, the ratio between the energy required for production and the produced capacity is used to compare factory setups. According to further research by Jinasena et al., this value is usually 30-60 Wh/Wh for energy efficient factories [2].

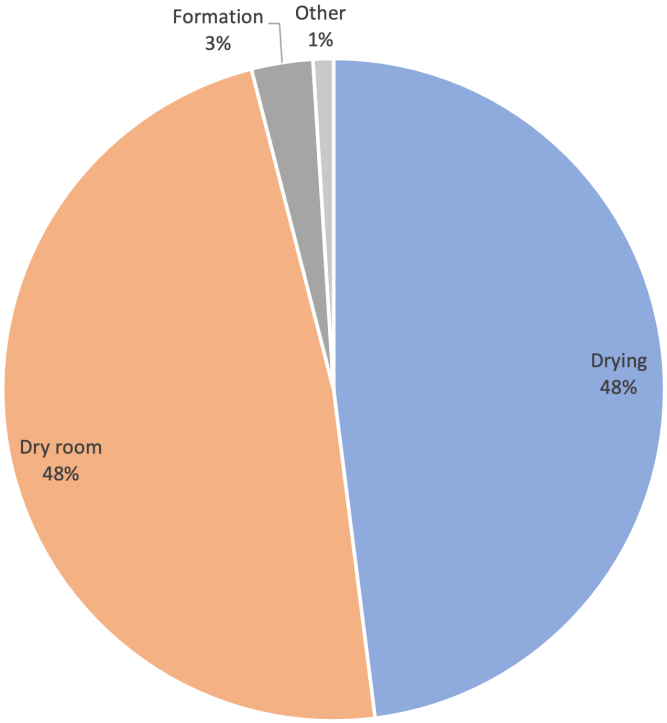

Figure 2.3: *The energy demand of the manufacturing process. Illustration is based on [7].*

2.2.2 Mixing

Mixing is the first step of a conventional battery manufacturing process. The materials involved in the manufacturing of the anode and cathode are separately mixed to avoid cross contamination. For industrial use, either batch- and continuous mixers are utilized. The finalized mix is called a slurry, and consist of the active material, solvent, binder and a conductive material. These materials are normally acquired from external producers. The performance of the electrodes are deeply dependent on their structure. Therefore, thorough mixing is important. The mixing duration is normally between 30 minutes and 5 hours when conducted at room temperature with a protective gas atmosphere [2, 7].

2.2.3 Coating

During coating, the mixed slurry is applied directly onto a conductive foil. The type of foil changes depending on whether the slurry is anode or cathode. The conductive foil is transported on an assembly line, with the slurry being coated continuously or intermittently depending on the manufacturer [7].

2.2.4 Drying

The drying process commences by transferring the electrode films into a high temperature chamber. This practice can be executed either in the form of batch drying, or continuously as shown in Figure 2.4. The film is then heated in order to evaporate the solvent from the newly coated slurry. Conventionally, the drying is performed using convective heat transfer and high temperature air circulating over the electrode films. Alternatively this can also be performed using radiation drying. Drying rate and drying time differ depending on solvent used and the temperature inside the chamber. The drying rate and temperature also need to be closely regulated, seeing as overly rapid drying can result in cracks and weaknesses in the electrode's structure [2]. In conventional battery manufacturing, this is one of the most energy consuming steps. It is therefore also a stage where a lot of energy can be saved through optimization. After the film is removed from the chamber, it is cooled to room temperature and ready for further processing [2, 7].

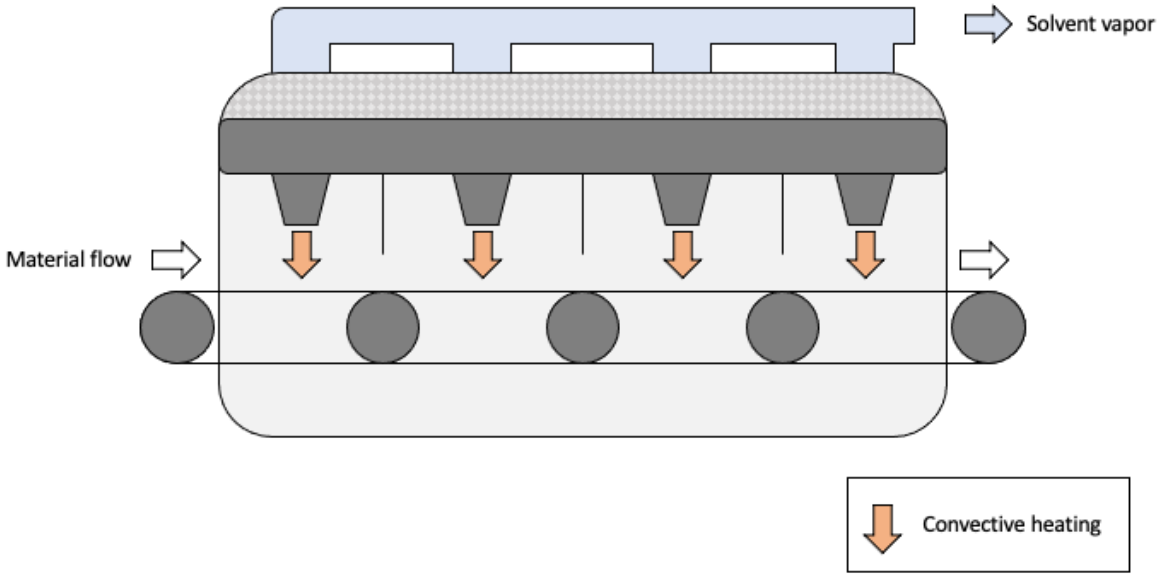

Figure 2.4: *Visualization of a continuous convective drying process. Adapted from [7].*

To reduce the amount of energy consumed during drying, a multi-stage drying process can potentially be utilized. This alternative drying process can consist of splitting the drying chamber into multiple sections with different temperatures, ranging from low heat to high heat. Alternatively, the temperature can be controlled in intervals when utilizing a batch dryer. This will reduce the overall heating load in comparison to a single-stage heating process, as it will reduce the amount of air that needs to be heated. The slurry moves through the multi-stage heating process as to maintain a constant drying rate. According to Oppegård et al. [12], using a multi-stage drying will not only lower the heating load, but will also decrease the drying time of the slurry due to increased drying rate [7].

2.2.5 Calendaring

Calendaring ensures the dimensions and quality of the newly dried film. To achieve this, the film is removed of any static charge, cleaned, compressed, measured and rolled. The compression process enables control over the porosity of the electrode substance [2, 7]. As an alternative, sintering, or heat pressing, can be used as alternative technologies. This entails using normal compression techniques in addition to applying heat to the material. This results in even more control over the porosity and shape of the final electrode geometry. This can also impact the energy density of the resulting cell [13].

2.2.6 Slitting

During slitting, the film is cut along its movement axis, creating separate smaller rolls. A set of rolling knives or laser cutters are commonly used for this stage. However, the rolling knives are subject to mechanical wear, while laser cutting need to take heat-affected zones into account. The cut quality and subsequent cleaning is also an important factor to the performance of the finalized battery as chipped-off electroconductive particles can damage the separator and cause short circuit [5, 2, 7].

2.2.7 Vacuum drying

The newly made rolls then need to undergo a second drying process before entering the dry room for further processing. They can either be stored as coils in a vacuum container, or dried as sheets. The goal of this step is to remove the residual solvent from the main drying process. A compressor is required to remove the air containing solvent from the vacuum drying chamber, and into the NMP recovery unit. However, the drying rate needs to be controlled properly during the vacuum drying to avoid rapid movement of binder particles resulting in cracks [9]. Therefore this is normally only used as a supplement to the actual drying process. The storage time for vacuum drying is usually between 12 to 30 hours, and the storage units can function as airlocks before entering the dry room [5, 7].

2.2.8 Separation and stacking

The separation step is exclusively for pouch cells. During separation the rolls are unwound and shaped to a desirable form by a punching tool, creating separate sheets of both the anode and cathode films. The cell is then built layer by layer with a repeated cycle of anode, separator, cathode, separator. Prismatic and cylindrical cells are instead wound together with the separator roll around a winding mandrel or a central pin respectively [2, 7].

2.2.9 Packing

During the packing stage, the current collectors are welded and the stacked cells are inserted into a corrosion-resistant packaging foil, which is then partially sealed. The packages are then ready to be filled with electrolyte [5, 2].

2.2.10 Electrolyte filling

The electrolyte filling process consist of two steps; filling and wetting. The partially sealed pouch is first filled in vacuum conditions with a liquid electrolyte substance by a high precision dosing needle. Pressure is then applied, activating a capillary effect, which completely fills the

cell. This process is called wetting. Filling and evacuating may be repeated a number of times depending on the manufacturer. Additionally, roll pressing can be performed on the pouch cell in order to ensure optimal wetting. A vibrating table may be used for prismatic and cylindrical cells. This stage needs to be performed in a dry room condition, since the electrolyte essentially condenses onto the electrodes. Introducing water condensate onto the cell is highly undesirable [2, 7].

2.2.11 Degassing

During the formatting stage, the cells are charged and discharged for the first time. The cells are stacked in a chamber, and connected to a power source with defined current and voltage profiles. During this process, the cell exhaust a certain amount of gas which is collected in a dead space, called a "gas bag", attached to the cell packaging foil. This bag is subsequently removed from the cell [7].

2.2.12 Aging

Before the finalized battery can be distributed, it undergoes a process called aging. Aging involves monitoring the batteries over a period of up to three weeks. This is done under various temperature conditions. The open circuit voltage, capacity and impedance is also measured at regular intervals. This stage ensures that the battery cell satisfies the quality of the manufacturer, and is used for detecting defect battery cells [2, 7].

2.2.13 End-of-line testing

After the aging period, the cells are brought into a lab for an end-of-line (EOL) testing. The battery cells are discharged to their shipping state-of-charge, and various testing is done to ensure they meet the customers expectations. The cells are then sorted by grade, and packed. The battery cells are then ready for shipping [2, 7].

2.3 Emerging technologies in battery production processes

The following sections describe some of the emerging technologies within the battery manufacturing sector. These include a different electrode composition, the transition from liquid to solid electrolyte, as well as some alternative drying methods. These are alternatives to the conventional process described in Section 2.2.

2.3.1 Semi-solid batteries

Semi-solid batteries offers a novel alternative to the traditional production process. These batteries utilize the principle of having small particles of active material suspended within the electrode. This entails using small solid-state particles suspended within a high viscosity fluid as the electrode. The solid active materials generally have a higher energy density compared to a respective fluid-based composition. This process suggests using extrusion based processing and thus bypasses the need for electrode drying, since the slurry does not contain NMP. The concept was first developed and applied to redox-flow batteries with a lithium-ion chemistry in Chiang et al. [14]. The concept was further developed and applied towards traditional lithium-ion batteries by some of the same researchers, in a patented technology. The patent suggests that the electrode would consist of 50-70 Vol% of these suspension particles within the electrode [3].

Further, the size of the suspension particles is estimated to be around $1 - 10$ μm. The patent also presents a concept of introducing salts to the slurry, prior to extrusion, in order to achieve the desired viscosity of the electrode [3].

The production process for a semi-solid battery is still not described in detail. However, the underlying patent [3], lists a number of concepts related to production of the electrodes. The flow chart explaining the individual production steps is shown in Figure 2.5 and is adapted from the explanation in the patent [3]. The suspension particles will either have to be crushed from raw material on site, or be acquired in an already crushed state. Further, all the materials are mixed together using conventional methods, but no solvents are added to this mixing process. The slurry will also hold slightly different properties to a conventional slurry and is highly viscous in addition to containing solid particles.

After mixing, there are two possible alternatives to the molding and insertion of the slurry into the electrode canisters. The first possibility is using high viscosity processing and extruding the semi-solid electrode material through an extrusion die. It is worth noting that this process can be time consuming depending on the viscosity and rheological properties of the semi-solid. Still, using an extrusion die enables a high degree of control over the thickness of the electrode. Previous studies by Wood et al. [15], suggests that this has the potential to increase the energy density of the cell, and therefore also decrease the required energy per battery capacity. Further, another published patent by Chiang et al. [16] suggests using an asymmetrical cell structure, with the cathode being thicker than the anode. This also has the potential to increase the energy density, seeing as the anode can be considered the bottleneck in this scenario. As a second alternative, using nozzles to discharge the semi-solid electrode into the canister is also possible. The patent also mentions possibilities of using post processing methods, such as mechanical vibrations, centrifuging or sonifications, in order to increase the degree of uniform distribution of suspension particles within the semi-solid substance [3]. Finally, the electrolyte filling is added. This is done by standard methods, consisting of introducing the electrolyte in a gaseous state, and having the substance condense onto the electrode.

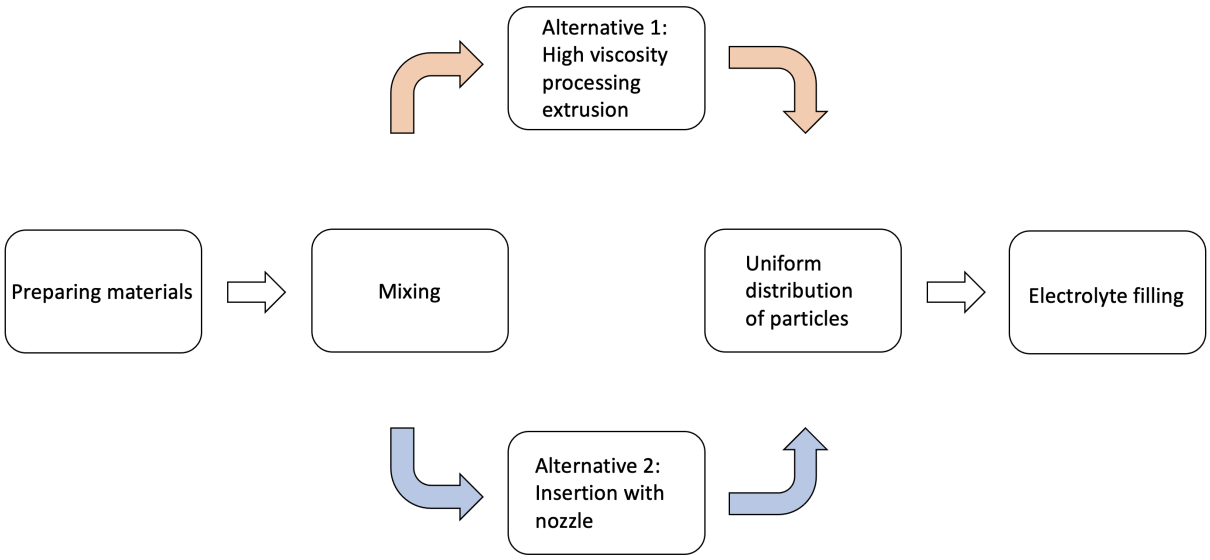

Figure 2.5: *Flow chart showing the individual steps in the production process of a semi-solid battery. Adapted from the description in [3].*

This process is noticeably different from traditional methods of production, and removes the need for a drying step altogether. As an alternative, it uses high viscosity processing through a flat extrusion die. This concept is depicted in Figure 2.6. The figure shows the extrusion die and a close up of a possible cathode structure with the solid suspension particles included. Verdier et al. [17] presents some of the challenges and benefits of using extrusion based processing for conventional chemistries and cell structures and also mentions that a solvent-free extrusion process can be less time consuming and more scalable than conventional manufacturing. However, it is difficult to predict how the properties of the semi-solid structure will affect the extrusion process in regards to the viscous and rheological properties.

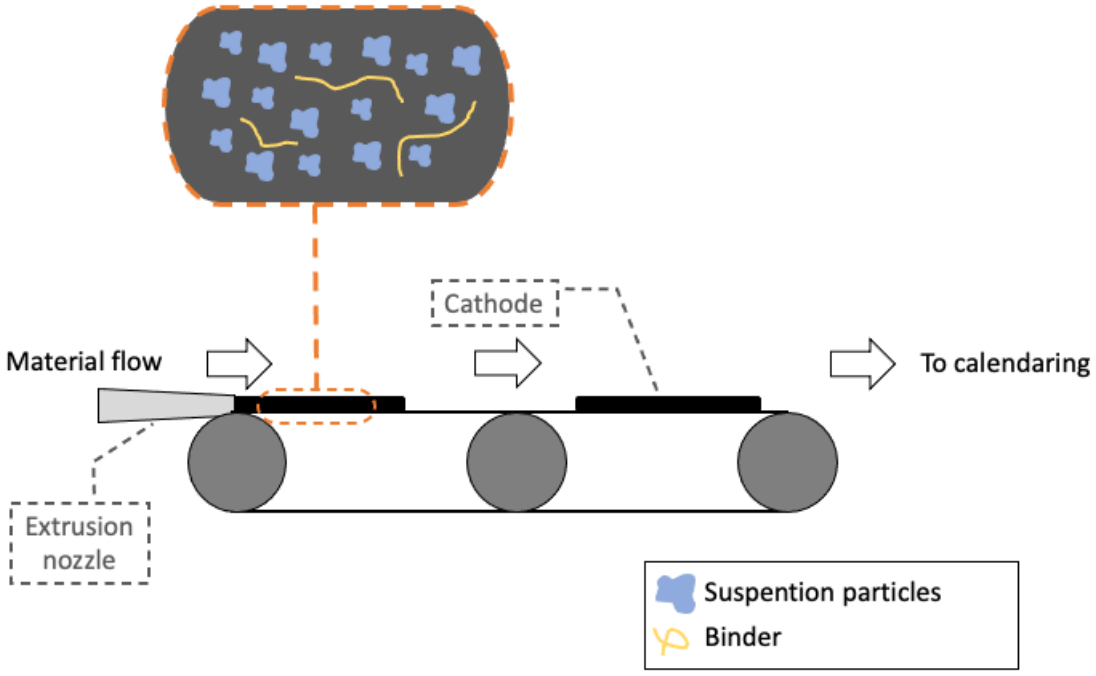

Figure 2.6: *Illustration of the extrusion process using semi-solid state technology. Adapted from the description in [3].*

2.3.2 Solid-state batteries

All-solid batteries consist of not only solid electrodes, but also a solid electrolyte solution. Due to solid electrolytes not requiring extensive drying, it will have the potential to minimize the amount of time spent in the dry room. Applying the electrolyte is normally a time consuming process that requires the specific atmosphere and controlled environment that the dry room provides. In this regard, the energy requirement for operating the dry room would potentially decrease. Additionally, a solid electrolyte would be much more facile to incorporate into a battery cell [18].

The use of solid electrolytes in battery production would in theory minimize the dry room requirements and the ambient conditions where the electrolyte is applied, seeing as the electrolyte is solid and does not need to condense onto the electrode surfaces when being applied. Thus, this makes the energy consumption of the dry room system less significant. Despite this, the technology is still mainly experimental and presents a series of challenges, like high flammability or electrolytic decomposition [18].

2.3.3 Laser drying

The use of lasers for battery production is an interesting alternative to conventional manufacturing techniques. Lasers can be used for both cutting of the electrodes and for electrode drying [19]. Using lasers for electrode drying specifically has the potential of reducing the energy required for production. The process is in theory able to bypass the need for heating the ambient

air and heats the slurry directly instead. Laser heating offers a high degree of precision and control over the heating of the material. In the medical sector, lasers are often operated with very short pulses to limit the amount of heat that defuses into the material [20]. This same principle can in theory be applied to the heating of battery electrodes. In order to limit the risk of cracks and damages during the drying of the electrode slurry, the frequency of these pulses can be altered throughout the drying process. For example, this would use high frequency pulses in the initial part of the drying process, limiting the diffusion rate throughout the material and thus also limiting the drying rate to avoid cracks. Later in the process, the frequency of the pulses can be decreased, increasing the heat applied to the slurry and keeping the drying rate constant. Using lasers in electrode production also has the potential to positively impact the quality of the electrode when there is such a high degree of control over the process. Vedder et al. [21] tested the impact of laser drying without altering frequency, and saw little difference in the resulting cell quality but a reduction energy consumption for production. Laser drying is still mostly in the experimental phase and the availability of lasers specifically for electrode manufacturing is limited.

2.4 Mathematical modelling of battery manufacturing

The following sections presents the theoretical equations needed for describing and simulating the battery manufacturing processes of convection drying and radiation drying. This includes the evaporation energy, drying time and heat source capacity.

2.4.1 Electrode drying methods

This section explains two of the different drying methods available; convection and radiation. As well as how their respective mathematical equations are derived.

2.4.1.1 Convection drying

Heat transfer by convection implies energy transfer from one location to another through the use of fluid currents [22]. The rate of which energy is transferred ($\dot{Q}_\mathrm{c}$) can be described by the empirical equation 2.1, which is known as Newton's law of cooling [23].

$$\dot{Q}_\mathrm{c} = h_\mathrm{t} A (T_\mathrm{s} - T_\mathrm{a}) \tag{2.1}$$

Here T_s and T_a represents the temperatures of the electrode surface and air, respectively. A is the surface area, and h_t is the heat transfer coefficient. Convection can be classified as either forced or free depending on the use of external forces in order to cause the fluid motion. The heat transfer coefficient of Equation 2.1 is an empirical parameter, meaning its value mainly stems from observations rather than mathematical theory. The value of h_t include the heat transfer relationship, fluid properties, flow patterns and geometry [23].

Alternatively the heat transfer coefficient for forced convection can be determined based on air velocity of turbulent flow, which results in Equation 2.2 [24]. Here, the heat constant k_c replaces h_t of Equation 2.1, and $\dot{q}_\mathrm{in,con}$ is measured in J/m^2.

$$\dot{q}_\mathrm{in,con} = \kappa_\mathrm{c} \cdot (T_\mathrm{s} - T_\mathrm{a}) \tag{2.2}$$

The heat transfer coefficient κ_c is defined by Equation 2.3, where V_a is the air velocity, μ is the air viscosity, ρ_a is the air density, λ_a is the thermal conductivity of the air, L is the characteristic length and Pr is the Prandtl number. This is an empirically derived equation [12].

$$\kappa_{\mathrm{c}} = 0.037 \cdot {V_{\mathrm{a}}}^{0.8} \cdot \left(\frac{\mu_{\mathrm{a}}}{\rho_{\mathrm{a}}}\right)^{-0.8} \cdot Pr^{\frac{1}{3}} \lambda_{\mathrm{a}} L^{-0.2} \tag{2.3}$$

2.4.1.2 Radiation drying

Thermal radiation is energy transported in the form of electromagnetic waves, also referred to as photons. This energy is emitted as a result of changes in a substance's electronic structure, and can travel without the help of any medium. All gases, liquids and solid objects either emit, absorb or transmit thermal radiation at a rate which is described by the Stefan-Boltzmann equation 2.4 [23].

$$\dot{Q}_{\mathrm{c}} = \epsilon \sigma A {T_{\mathrm{b}}}^4 \tag{2.4}$$

Where $\dot{Q}_{\mathrm{c}}$ is the rate which energy is being emitted, ϵ is the emissivity, which is a measurement of an objects ability to emit energy as thermal radiation, A is the surface area, T_{b} is the absolute surface temperature and σ is the Stefan-Boltzmann constant which is defined as $\sigma = 5.67 \cdot 10^{-8}$ $\mathrm{W/m^2 \cdot K^4}$ [23].

Expanding on Equation 2.4 it is possible to determine the net energy transfer between a surface and its surroundings. This net rate of energy by thermal radiation ($\dot{q}_{\mathrm{in,rad}}$) is described by Equation 2.5 where $T_{\mathrm{sur.}}$ is the surrounding temperature [23].

$$\dot{q}_{\mathrm{in,rad}} = \epsilon \sigma A [{T_{\mathrm{b}}}^4 - {T_{\mathrm{sur.}}}^4] \tag{2.5}$$

2.4.2 Required energy for drying

The drying time and energy required for evaporating a solvent from an electrode in the drying process of battery manufacturing can be mathematically determined using functions for the decreasing film thickness and solvent content, as well as the increasing film temperature being warmed by a constant heat source. The following sections show how such a model can be derived similarly to the one developed by Oppegård et al. [12]. However, it is important to note that this is just the evaporation energy and does not regard the energy required for heating and cooling of the airflow.

2.4.2.1 Fluxes and diffusion coefficient

By assuming uniformity in the x- and y-direction of a control volume, as well as a constant velocity in the y-direction, the resulting fluxes of the control volume will be defined by the z-direction [12, 25]. The constant velocity in the y-direction representing the speed of the conveyor belt of the manufacturing process. In the case of drying a solvent, the fluxes due to diffusion can be expressed by the one-dimensional equation 2.6, where C is the weight fraction of the solvent and D the diffusion coefficient. This is known as the heat diffusion equation and is a differential equation applicable to heat transfer in any material [12].

$$\frac{\partial C}{\partial t} = D \frac{\partial^2 C}{\partial z^2} \tag{2.6}$$

The diffusion coefficient (D) of Equation 2.6 is a function of the polymer volume fraction and temperature, given by Equation 2.7 [12, 25].

$$D = D_0 \cdot \left(\frac{1 - \Phi_{\mathrm{p}}}{1 + \Phi_{\mathrm{p}}}\right)^{\gamma} \cdot \exp\left(\frac{-E}{RT}\right) \tag{2.7}$$

Here D_0 represents the mutual diffusion coefficient, Φ_p is the polymer volume fraction, γ is a constant empirical value, E is the activation energy, R is the universal gas constant and T is the temperature of the film [12, 25]. The mutual diffusion coefficient will vary based on composition of the slurry [12].

2.4.2.2 Implementing boundary conditions

The boundary conditions are defined by implying zero flux at the bottom of the film, meaning at $z = 0$ the flux $\frac{\partial C}{\partial z} = 0$. Meanwhile, at the top of the film, the boundary condition is dependent on the mass transfer from the solvent to the surrounding air. This loss of mass causes a shrinkage of the film, which is taken into account as $z = h(t)$, where h is the thickness of the film. The boundary condition can thus be defined as shown in Equation 2.8, which is based on the ideal gas law [12, 25].

$$D\frac{\partial C}{\partial z} + C\frac{\mathrm{d}h}{\mathrm{d}t} = -\frac{\kappa_m M_s}{\rho_s R} \cdot \left(\frac{P_s}{T} - \frac{P_a}{T_a}\right) \tag{2.8}$$

Here, M_s is the molecular weight of the solvent, ρ_s is the density of the solvent, P_s is the equilibrium partial pressure of the solvent, P_a is the pressure in the air and T and T_a is the temperature of the film and the heated air, respectively [12].

$$\kappa_m = \frac{\kappa_c}{\rho_a Cp} \cdot \mathrm{Le}^{\frac{-2}{3}} \tag{2.9}$$

The mass transfer coefficient (κ_m) is as shown in Equation 2.9, with Le being the Lewis number, ρ_a representing the density of the air, and Cp depicting the specific heat of the air [24]. The heat transfer coefficient, κ_c, is described by Equation 2.3. The Lewis number is shown in Equation 2.10, expressed as the relation between the Prandtl number (Pr) and Schmidt number (Sc).

$$\mathrm{Le} = \frac{\mathrm{Sc}}{\mathrm{Pr}} = \frac{\lambda}{\rho_a Cp D} \tag{2.10}$$

The solvent vapor pressure (P_{sol}) can be expressed using Flory Huggins theory for polymeric solutions, which is shown in Equation 2.11, where P_0 is the vapor pressure of the pure solvent, χ representing the Flory Huggins interaction parameter, Φ_s being the solvent volume fraction, and V_s and V_p represent the volume of solvent and solid, respectively [12].

$$P_{sol} = P_0 \cdot \exp\left(\Phi_p^2 \cdot \chi + ln(\Phi_s) + \left(1 - \frac{V_s}{V_p}\right)\Phi_p\right) \tag{2.11}$$

The vapor pressure (P_a) of the ambient air can be approximated using the Antoine equation 2.12, where ϕ is the relative humidity of the air and T_a is the air temperature [12].

$$P_a = \phi \cdot 133.332 \cdot 10^{7.54826 - \frac{1979.68}{222.2 + (T_a - 273.15)}} \tag{2.12}$$

2.4.2.3 Applying mass balance

By applying mass balance to the boundary conditions set in Equation 2.8, a formula for the thickness of the film can be found. This thickness is shown in Equation 2.13 [12].

$$\frac{\mathrm{d}h}{\mathrm{d}t} = -\frac{\kappa_m M_s}{\rho_f R} \cdot \left(\frac{P_s}{T} - \frac{P_a}{T_a}\right) \tag{2.13}$$

Here, ρ_f represents the overall film density, expressed through Equation 2.14 with ρ_p being the bulk density of the solid. The equation assumes a linear correlation [12].

$$\rho_{\mathrm{f}} = \rho_{\mathrm{s}} \cdot C + (1 - C) \cdot \rho_{\mathrm{p}} \tag{2.14}$$

2.4.2.4 Evaporation energy and energy balance

The energy required to evaporate a solvent is given by Equation 2.15, where Q is the evaporation energy and t_{f} the total drying process time [12].

$$Q = \int_0^{t_f} \dot{m}_{\mathrm{evap.}} \lambda \cdot \mathrm{d}t \tag{2.15}$$

The evaporation rate ($\dot{m}_{\mathrm{evap.}}$) is expressed by Equation 2.16, and is further derived from the ideal gas law [12].

$$\dot{m}_{\mathrm{evap.}} = \frac{\kappa_{\mathrm{m}} M_{\mathrm{s}}}{R} \cdot \left(\frac{P_{\mathrm{s}}}{T} - \frac{P_{\mathrm{a}}}{T_{\mathrm{a}}} \right) \tag{2.16}$$

Also, λ is the latent heat of evaporation of the solvent. This value can be approximated using the second degree polynomial Equations 2.17 or 2.18 for water and NMP, respectively. These equations are derived empirically from experimentation. [12].

$$\lambda_{\mathrm{W}} = -3.345 \cdot T^2 - 259.3 \cdot T + 2.817 \cdot 10^6 \tag{2.17}$$

$$\lambda_{\mathrm{NMP}} = 6.991 \cdot T^2 - 6193 \cdot T + 1.848 \cdot 10^6 \tag{2.18}$$

Modifying Equation 2.13 further by neglecting the relatively small contributions of sheer stress and surface tension, gives a final energy balance expression for the film shown in Equation 2.19. Here $\dot{q_{in}}$ is the heat flux applied to the material surface [12].

$$h\frac{\mathrm{d}T}{\mathrm{d}t} + T\frac{\mathrm{d}h}{\mathrm{d}t} = -\frac{\kappa_{\mathrm{m}} M_{\mathrm{s}} \lambda}{\rho_{\mathrm{f}} R} \cdot \left(\frac{P_{\mathrm{s}}}{T} - \frac{P_{\mathrm{a}}}{T_{\mathrm{a}}} \right) + \frac{\dot{q_{in}}}{\rho_{\mathrm{f}} C_p} \tag{2.19}$$

2.4.2.5 Air heating

For convective drying, the energy required for heating the air in the drying process can be described through Equation 2.20 below. Here, $\dot{m}_{\mathrm{a}}$ is the mass flow rate of the air through the heating chamber [12].

$$E_{\mathrm{drying}_a} = \dot{m}_{\mathrm{a}} c_{p_{\mathrm{a}}} (T_{\mathrm{a}} - T_{\mathrm{a}_0}) t_{\mathrm{drying}} \tag{2.20}$$

For radiation drying, the ambient air temperature will increase as a function of time. This temperature change can be modeled using Equation 2.21, where T_{b} is the temperature of the heat source [12].

$$\frac{\mathrm{d}T_{\mathrm{a}}}{\mathrm{d}t} = \frac{\kappa_{\mathrm{c}}(T_{\mathrm{b}} + T - 2T_{\mathrm{a}}) + \dot{m}_{\mathrm{evap.}} C\mathrm{p_s}(T - T_{\mathrm{a}})}{\rho_{\mathrm{a}} C_{\mathrm{p_a}}} \tag{2.21}$$

2.4.2.6 Total energy consumption for drying

The total energy consumption for convective heating can be approximated to the sum of the energy required by the solvent evaporation and the air heating. This is given by Equation 2.22, where E_{drying} is the total energy consumption of the drying process. The values for $E_{drying_{\mathrm{a}}}$ and $E_{drying_{\mathrm{s}}}$ are the individual energy contributions from the heat source and solvent evaporation, respectively. [2, 12].

$$E_{drying} = E_{drying_a} + E_{drying_s} \tag{2.22}$$

2.4.2.7 Conversion into dimensionless model

In order to create a dimensionless model of the drying process, the variables need to be expressed as dimensionless, with values ranging from 0 to 1. This is done by dividing these parameters by their end value, thus resulting in the desired value range. This is done for ease of solution of the model [12]. The new variables become as follows:

$$\widetilde{t} := \frac{t}{t_0} \qquad \widetilde{z} := \frac{z}{h} \qquad \widetilde{L} := \frac{h}{h_0}$$

$$\widetilde{T} := \frac{T}{T_0} \qquad \widetilde{C} := \frac{C}{C_0} \qquad \widetilde{D} := \frac{D}{D_0}$$

Replacing the variables of the previously described equations for changes in solvent fraction, thickness and temperature, results in Equation 2.23, 2.24 and 2.25, respectively [12].

$$\frac{\partial \widetilde{C}}{\partial \widetilde{t}} = \frac{\widetilde{D} D_0 t_0}{(\widetilde{L} h_0)^2} \frac{\partial^2 \widetilde{C}}{\partial \widetilde{z}^2} \tag{2.23}$$

$$\frac{d\widetilde{L}}{d\widetilde{t}} = -\frac{\kappa_m M_s t_0}{\rho_f R h_0} \cdot \left(\frac{P_s}{\widetilde{T} T_0} - \frac{P_a}{T_a} \right) \tag{2.24}$$

$$\frac{\mathrm{d}\widetilde{T}}{\mathrm{d}\widetilde{t}} = -\frac{\kappa_m M_s \lambda t_0}{\rho_f C_p R \widetilde{L} h_0} \cdot \left(\frac{P_s}{\widetilde{T} {T_0}^2} - \frac{P_a}{T_a T_0} \right) - \frac{\widetilde{T}}{\widetilde{L}} \frac{\mathrm{d}\widetilde{L}}{\mathrm{d}\widetilde{t}} + \frac{t_0}{\rho_r C_p \widetilde{L} h_0 T_0} \dot{q}_{in} \tag{2.25}$$

The boundary conditions for $\widetilde{z} = 0$ is shown in Equation 2.26 and for $\widetilde{z} = 1$ in Equation 2.27, and the initial conditions are displayed in Equation 2.28 [12].

$$\frac{\partial \widetilde{C}}{\partial \widetilde{t}} = 0 \tag{2.26}$$

$$\frac{\widetilde{D} D_0 C_0}{\widetilde{L} h_0} \frac{\partial \widetilde{C}}{\partial \widetilde{t}} + \frac{\widetilde{C} C_0 h_0}{t_0} \frac{\mathrm{d}\widetilde{L}}{\mathrm{d}\widetilde{t}} = -\frac{\kappa_m M_s}{\rho_s R} \left(\frac{P_s}{\widetilde{T} T_0} - \frac{P_a}{\mathrm{T_a}} \right) \tag{2.27}$$

$$\widetilde{C}(0, \widetilde{z}) = 1 \qquad \widetilde{T}(0) = 1 \qquad \widetilde{L}(0) = 1 \tag{2.28}$$

2.4.2.8 Finite-difference method and forward time central space differential scheme

The finite-difference method (FDM) is used for solving differential equations of one-dimensional systems. The approach include approximation of derivatives with finite differences, hence the name. A continuous domain is discretized for space and time, and the differential terms are converted into linear algebraic equations [26].

Anderson et al. [27] describes the FDM as an approximation of the derivatives using the finite part of the Taylor Series expansion, and the forward time central space (FTCS) differential scheme as shown in Equation 2.29 and 2.30 [12].

$$\frac{\mathrm{d}f}{\mathrm{d}\widetilde{t}} = \frac{f^{i+\Delta\widetilde{t}} - f^i}{\Delta\widetilde{t}} \tag{2.29}$$

$$\frac{\partial^2 f}{\partial \widetilde{z}^2} = \frac{f_{j+\Delta\widetilde{z}} - 2f_j + f_{j-\Delta\widetilde{z}}}{\Delta\widetilde{z}^2} \tag{2.30}$$

2.5 Dry room

A dry room is an enclosure with low humidity and a certain level of cleanness. It is an essential part for processes that require a dry and clean environment, such as the cell assembly stages in a battery manufacturing process. Liquid electrolyte filling is highly sensitive to water vapor, requiring surroundings with moisture-levels of less than 100 parts per million by volume [28]. ISO standards usually guidelines the dryness and the control of contamination for dry rooms [29, 30].

By design, a dry room is made leak-proof with few points of entry. The room's volume and the moisture concentration are key parameters in construction, and impacts the total energy requirement significantly [28]. For LIB manufacturing, the dry room can account for almost half the total energy usage [2]. Desiccant systems, explained in Section 2.5.1 and 2.5.2, are tools that can be used in order to dehumidify the inlet air of a dry room.

2.5.1 Liquid desiccant system

A liquid desiccant system is a mechanism that removes humidity and sensible heat from the air through the use of a liquid desiccant material and thermal energy [31, 32]. Commonly used desiccant materials includes lithium chloride (LiCl), calcium chloride ($CaCl_2$), and lithium bromide (LiBr) [32].

The basic configuration of a liquid desiccant system is depicted in Figure 2.7. Here, the absorber- and regenerator columns are connected through the use of piping that circulate the liquid desiccant. The cooled desiccant is sprayed from the top of the absorber column, dehumidifying the ambient air blowing from below. The dehumidified dry air is then expelled at the top of the column. As the liquid desiccant absorbs water, it becomes diluted and pools at the bottom of the absorber column. This diluted solution is then heated and pumped to the regenerator column. Fresh air is injected at the bottom of the column, extracting some of the water molecules. The moisturised air is then expelled at the top of the column, while the concentrated desiccant is collected at the bottom before being cooled and pumped back into the absorber column, closing the loop [32]. Desiccant systems often operate at high pressure ranges, and the pressure of the airflow entering the absorber column therefore needs to increased by a compressor. Around 5-20 bar is standard for larger industrial scale desiccant systems [33]. A heat exchanger can be added for regeneration between the two streams significantly reducing energy demand [28].

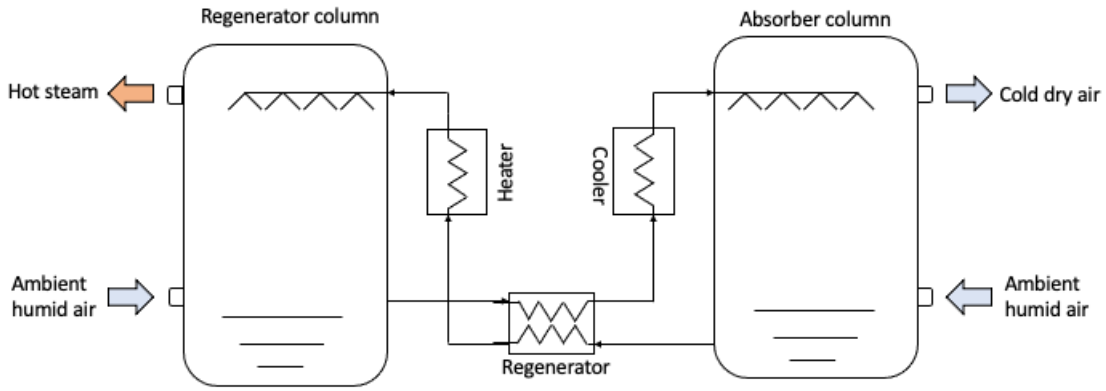

Figure 2.7: *A basic liquid desiccant system. Left side is the desiccant regenerator and the right side is the water absorption column. The liquid desiccant is circulated between the two columns through the heat exchangers. Figure is inspired by [34].*

2.5.2 Solid desiccant system

The solid desiccant system utilize a solid hygroscopic material, such as silica gel, zeolite or solid lithium chloride, to dehumidify a passing airflow. There are different configurations depending on purpose. However, the rotating desiccant wheel system is considered superior due to its low pressure drop, simplicity and easy maintenance. Figure 2.8 depicts a zeolite desiccant wheel [31].

A desiccant wheel operates at slow rotational speed with intake air blowing at a given portion. The solid desiccant absorbs the humidity from the passing air, which is further cooled by a heat exchange wheel and then supplied to the designated area. The returning air pass through the same wheels in opposite order, with hot air blowing at the remaining portion of the solid desiccant wheel, removing the previously absorbed humidity [32].

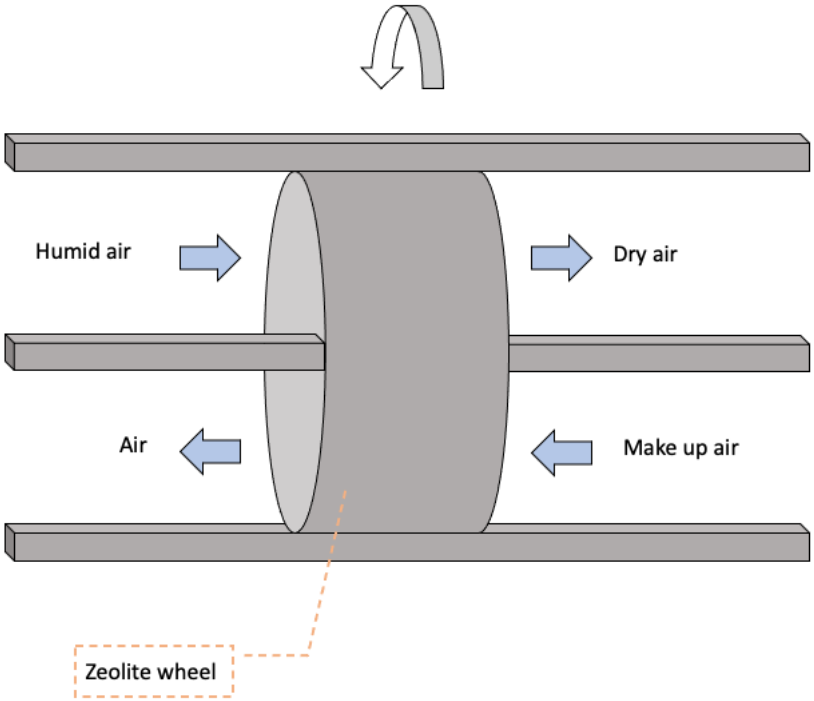

Figure 2.8: *Depiction of a Zeolite wheel in a solid desiccant system. Adapted from [35].*

These systems are usually applied to areas of high humidity, and has seen implementation in large scale commercial buildings [31]. They can also be used in the removal of hazardous materials, like the removal of solvents such as NMP in battery manufacturing [35]. This is further explained in Section 2.6.2.

2.5.3 The fundamentals of a liquid desiccant system

The energy requirement for a dry room utilizing a liquid desiccant absorption system in order to regulate the humidity of the ambient environment of the dry room can be mathematically approximated. Firstly, a heat transfer coefficient ($\mathrm{h_d}$) is derived empirically from the expression presented by Coulson et al. [36], which is displayed in Equation 2.31 [2].

$$\mathrm{h_d} = \frac{d}{a}\dot{\mathrm{m}}_\mathrm{l}^{e}\dot{\mathrm{m}}_g^{f} \tag{2.31}$$

Here, d, e and f are empirical constants whose value depend on the composition the liquid desiccant and the gas or air. For a dry room, the dry air flow rate ($\dot{\mathrm{m}}_\mathrm{g}$) can be selected using ISO standards [30]. Similarly, $\dot{\mathrm{m}}_\mathrm{l}$ represent the liquid desiccant flow rate, which is found from the selected liquid desiccant absorption tower system design [2]. These flow rates are given in $\mathrm{kg/m^2s}$. Furthermore, the desiccant system is also used in order to determine the interfacial area per unit volume (a), as well as the parameters A_l and A_g used in Equation 2.32 [2].

Equation 2.32 is used in order to determine the total resistance (R_T) of the process. Here, A_l and A_g is the transfer area of liquid desiccant side and gas side, respectively. h_l represents the liquid heat transfer coefficient and h_g represents the gas heat transfer coefficient [2].

$$\frac{1}{R_\mathrm{T}} = \frac{1}{h_\mathrm{l} + A_\mathrm{l}} + \frac{1}{h_\mathrm{g} + A_\mathrm{g}} \tag{2.32}$$

This total resistance can then be used in order to determine the total cooling load (P_c), which is shown in Equation 2.33. T_{gi} represent the ambient air temperature, while T_{li} is the inlet temperature for the liquid desiccant system, which is found from the absorber design [2, 36].

$$P_c = (T_{gi} - T_{li})R_T \tag{2.33}$$

In order to calculate the total heating load (P_h) required, the temperature of the air at the absorber gas outlet (T_{go}) needs to be determined. This is found using Equation 2.34 and the values of the parameters previously found [2].

$$T_{go} = T_{gi} - \frac{P_c}{h_g + A_g} \tag{2.34}$$

The total heating load is then found using Equation 2.35. This equation is standard for all temperature difference energies and can be used to calculate the heat exchanger duty. On Figure 2.7, this corresponds to the energy required for heating the airflow after being processed by the desiccant system. Here, T_{dr} is the required air temperature of the dry room, and Cp_a is the specific heat capacity of the dry air [2].

$$P_h = \dot{m}_g Cp_a (T_{dr} - T_{go}) \tag{2.35}$$

Thus, an equation for the total energy required for maintaining the dry room standards can be derived. This is shown in Equation 2.36. The parameter $t_{dryroom}$ represents the time used in order to complete the process steps inside the dry room [2].

$$E_{dryroom} = (P_h + P_c)t_{dryroom} \tag{2.36}$$

These equations do not account for losses in the heat exchangers or the required energy for pumping.

2.6 Heat pump and solvent removal

This section explains the principles of heat pumps, as well as how solvent is removed and recovered from the drying process.

2.6.1 Heat pumps

A heat pump is a system that transfers energy between two thermal reservoirs of different temperatures. The system is based on the Carnot vapor power cycle or the Carnot vapor refrigeration cycle, depending on whether the goal of the cycle is to increase or decrease temperature [23].

A basic heat pump is depicted in Figure 2.9 and consists of four parts; the evaporator, compressor, condenser and turbine or expansion valve. At the inlet of the evaporator, the circulating fluid of the cycle is a vapor-liquid mixture. When passing through the evaporator, some of this liquid evaporates to vapor-phase using the energy extracted from the cold reservoir. The fluid is then run through a compressor, which increases the pressure of the fluid from two phase vapor fluid mix, to saturated vapor. The liquid then flows through a condenser which extracts energy by changing the fluid's phase from saturated vapor to saturated liquid. In this process, the energy is released in the form of heat, which is then transported into the hot reservoir. The fluid is then expanded adiabatically through a turbine which returns it to the same state as at the inlet of the evaporator, closing the loop [23].

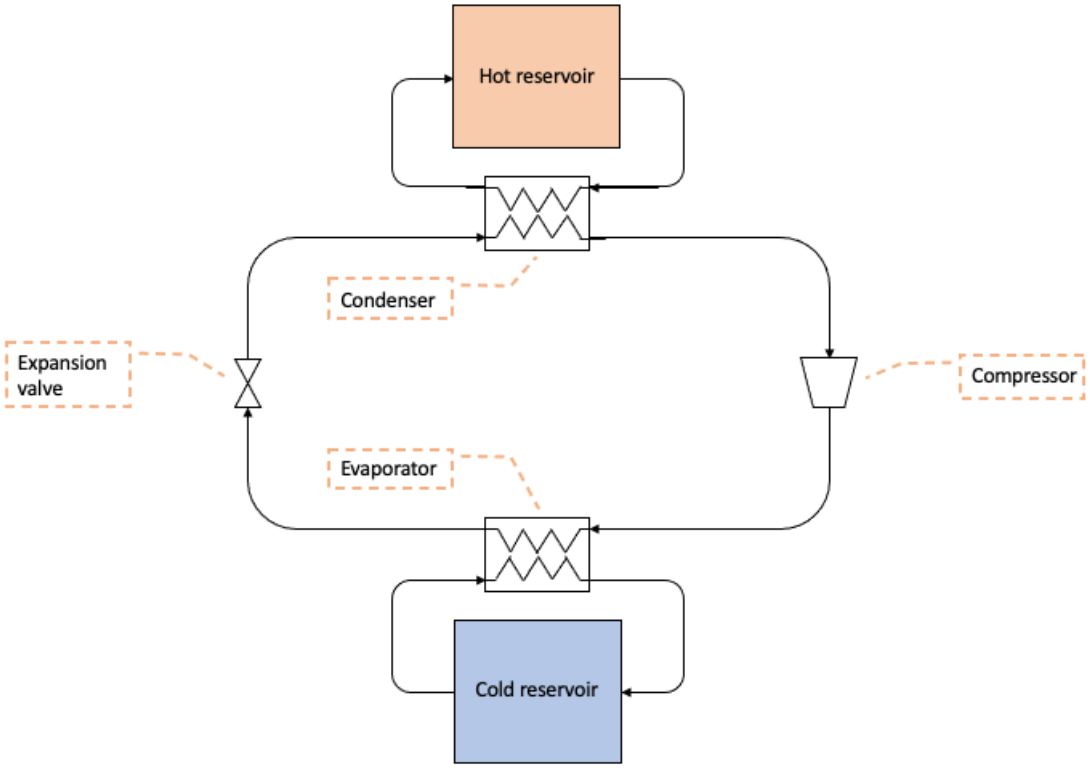

Figure 2.9: *Component schematic of a basic heat pump design.*

2.6.1.1 Heat exchanger

A heat exchanger is a system which seeks to transfer heat from one fluid to another. A heat exchanger transfers heat either by convection or conduction. The fluid used in a heat exchanger can be either a gas or a liquid depending on its area of use. Heat exchangers are often part of larger systems such as heat pumps to transfer and make use of residual energy efficiently [23].

A type of heat exchanger commonly used for industrial purposes is the shell-and-tube heat exchanger. It consists of a large amount of tubes with an outer shell structure, utilizing crossing fluid streams in order to transfer energy.

The cross sectional heat transfer area (A_h) of a heat exchanger is described by Equation 2.37. Here, $\dot{Q}$ is the heat load in watt, U is the overall heat transfer coefficient, and ΔT is the logarithmic mean temperature difference (LMTD) between the two sides of the heat exchanger.

$$A_h = \frac{\dot{\mathrm{Q}}}{\mathrm{U} \cdot \Delta \mathrm{T}} \tag{2.37}$$

The LMTD is the temperature difference between the fluids in the heat exchanger. This value can be vary depending on the type of heat exchanger being used. A typical value for heat exchangers is 10 °C. This is because this value represents a good balance between were the heat exchanger is efficient but at the same time has reasonable size in terms of heat exchanger area. A lower temperature difference than this will require a larger heat exchanger. A higher temperature difference will in term require a smaller heat exchanger which will decrease the amount of heat being transferred [37].

2.6.1.2 Compressor

A compressor is a device which seeks to increase the pressure of a gas or vapor. When saturated vapor is compressed, it allows for isothermal expansion which will increase the internal energy of the working fluid. Because of this, compressors are commonly used in heat pumps and refrigeration systems [23].

2.6.1.3 Expansion valve

An expansion valve decreases the pressure in a working fluid. It is often placed before the evaporator in a heat pump or refrigeration cycle. The pressure is decreased by forcing the working fluid through a small orifice. This transforms the working fluid into a saturated liquid-vapor mix, which allows the liquid to absorb energy in the evaporator, making it superheated [23].

2.6.2 NMP recovery process

In LIB manufacturing, NMP is a water soluble that can be used as solvent in the mixing of the electrodes. Due to the polluting and hazardous nature of NMP, it is recovered and recycled during the drying process, effectively reducing emission as well as avoiding replacement cost [35].

Recycling of NMP during the LIB manufacturing process is increasingly becoming an essential part of the industry as it matures. The current market price for NMP is also making it expensive, which means that any amount of NMP recovered during the manufacturing process has a potential to save total production cost [38]. However, a NMP recovery system requires a high amount of energy to recover the solvent. The total energy requirement for the filtration and extraction is estimated to be 45 times that of the evaporation energy of the NMP [35].

Figure 2.10 shows a schematic of an NMP removal system used in LIB manufacturing. After the electrode drying, the heated and solvent-moisturised air pass through a regenerator before being cooled further in a condenser. Here, most of the solvent is removed as condensate and stored. However, not all the NMP turns to a liquid state during the condensation. The remaining air is therefore dehumidified with the use of a solid desiccant system, depicted in Figure 2.10 as a zeolite wheel, and finally a scrubber. The solvent absorbed by the solid desiccant wheel is recycled into the drying process, being preheated in the regenerator. This heating and cooling process is the reason why NMP removal is so energy intensive. The evaporation energy during drying is almost negligible compared to the energy required for heating and cooling of the airflow [35].

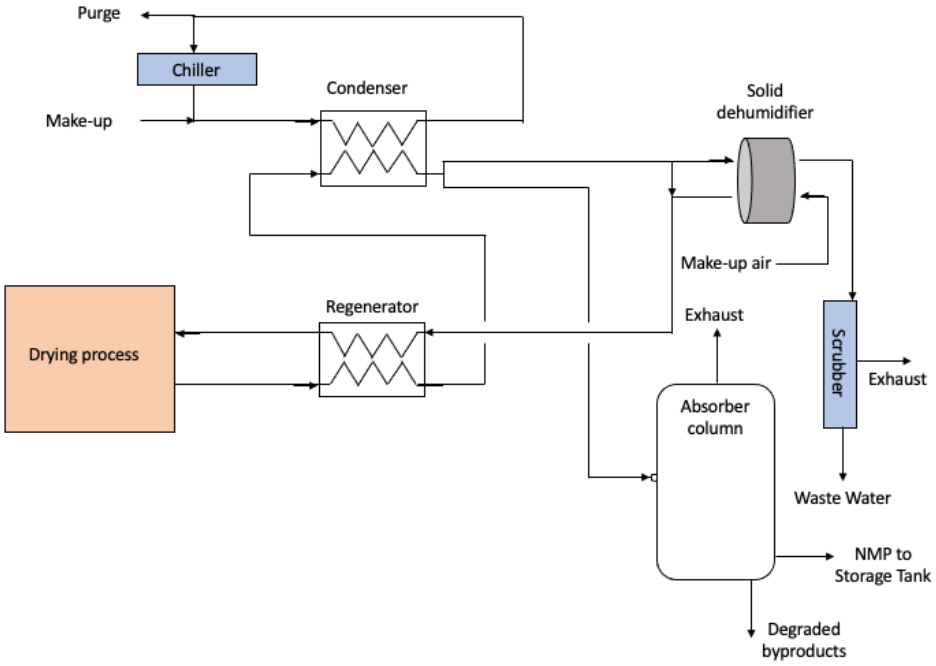

Figure 2.10: *NMP removal system depicting the recovery and recycling of NMP in LIB manufacturing. Illustration based on [35].*

2.7 Pinch analysis

A pinch analysis is used for systematically determining the minimum amount of energy required for a process through the laws of thermodynamics. With optimal design of heating, cooling and heat recovery systems, the process can achieve a noticeable enhancement in efficiency. The application of a pinch analysis on a system often involves choosing between multiple designs that favor different factors in the system. These factors can be operating costs, installation cost or heat exchanger area. This means that when performing a pinch analysis on a system, the final design is heavily affected by which factors is deemed most important [39].

By performing a pinch analysis on a system, two graphs called the composite curve and grand composite curve can be made. These graphs depicts the areas of improvement present in the system. The graphs are described in following sections. Pinch analysis essentially identifies the so called bottleneck of the stream network [39].

2.7.1 Composite curves

A temperature-enthalpy diagram is commonly used to illustrate the heat exchange between hot and cold streams. Diagrams for multi-stream processes containing several of these streams are called composite curves. Adding the heat loads for all the separate hot streams results in a single composite stream, called a hot composite curve. A similar procedure for the cold streams results in a cold composite curve. When comparing the hot and cold composite curves in a single diagram, the pinch is observed at the point where ΔT_{min} between the two streams is at its lowest, in other words the bottleneck of the system [39].

The hot and cold composite curves can be shifted horizontally to find the lowest ΔT_{min} required for the system. However, it is not possible to shift the composite curves vertically as this would

interfere with the temperature ranges of the system. Figure 2.11 shows the pinch of an arbitrary system. The area above pinch is called the net heat sink. Here, external heating is required. Similarly, net heat source is located below pinch, which require external cooling. The heat flow across pinch is zero. The composite curve also describes the size of the heat exchangers required to heat the streams by calculating the area between the inflection points of the hot and cold composite curves [39].

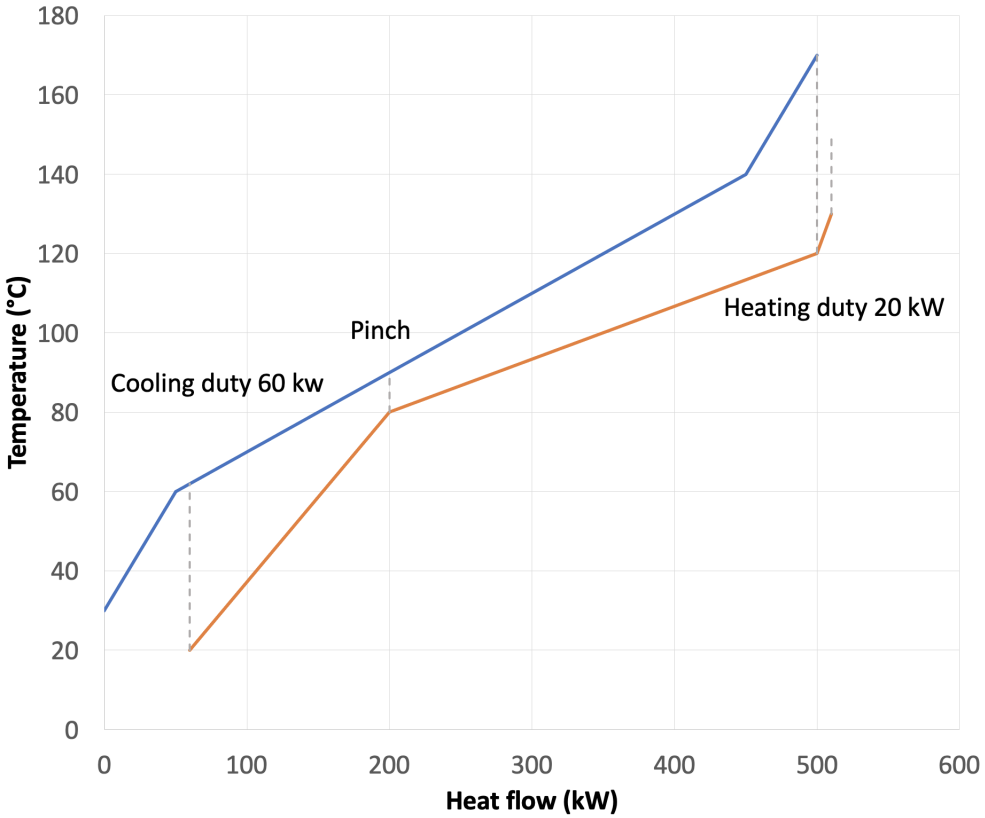

Figure 2.11: *The composite curve of an arbitrary system. Illustration is based on [39].*

2.7.2 Grand composite curves

The grand composite curve shows the relationship between available heat and required heating at any instance above and below pinch. The grand composite curve exist as a supplement to the composite curve. As shown in the grand composite curve in figure 2.12, the pinch point is located in the point where the graph touches the temperature axis, signifying that there is no heat exchange across pinch. In the graph, the heat sink is shown to be between the temperature axis and the highest temperature in the system. In this case, the heating duty is 20kW. Similarly the heat source is placed at the bottom of the graph and is equal to 60kW. The parts of the graph where heat is allowed to transfer are isolated either above or below pinch in the parts where the graph overlaps. From these values, the size of the heat exchangers can be calculated [39]. How the size of a heat exchanger is found is presented in Section 2.6.1.1. Generally, the size of a heat exchanger is correlated to the cost. Thus, the resulting heat exchanger size is also be considered when evaluating the resulting network in a design. The grand composite curve contains energy pockets around the pinch temperature. This is an area with residual heat, but a heat exchanger cannot be used since the temperature ranges are not sufficient [40].

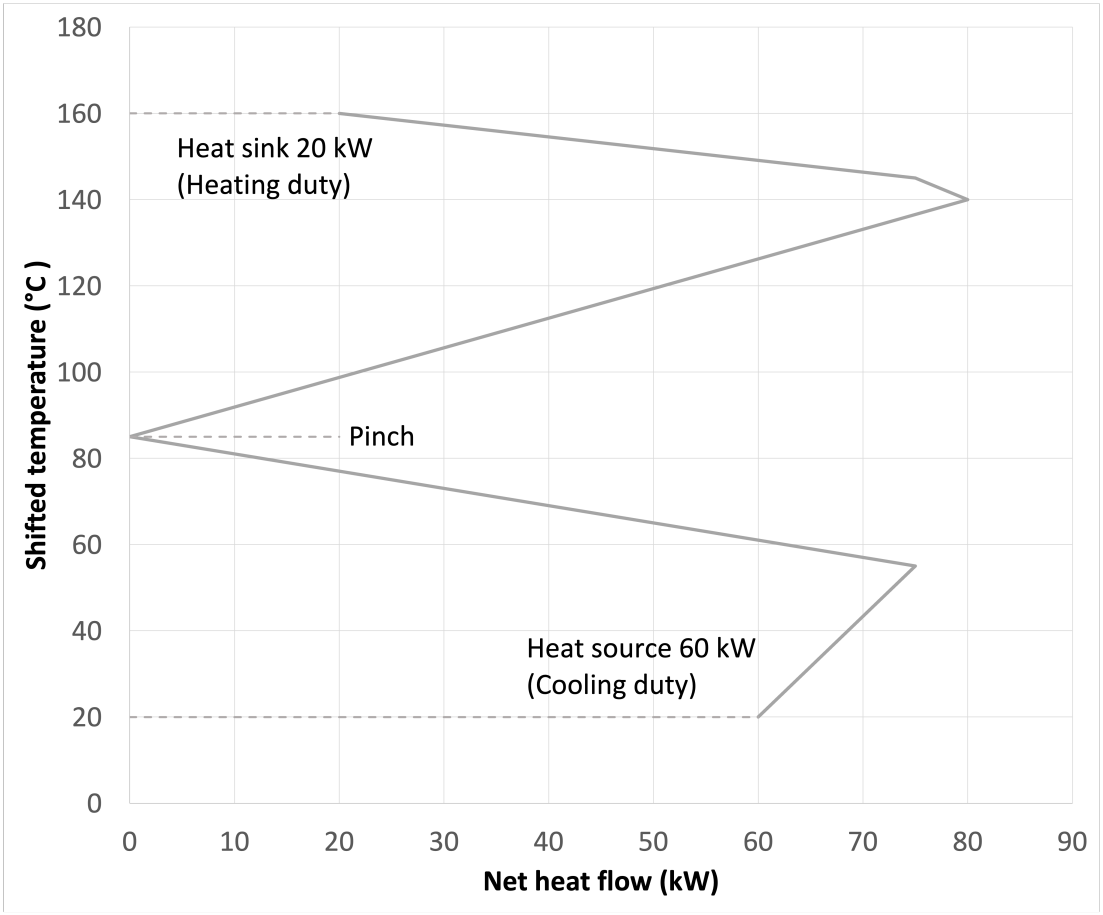

Figure 2.12: *A grand composite curve of an arbitrary system. Illustration based on [39].*

2.7.3 MER-networks

A Maximum Energy Recovery (MER) network is a system that is based on pinch analysis and consists of a network of heat exchangers optimally placed for maximum energy recovery. An arbitrary MER-network is illustrated in Figure 2.13. The horizontal lines represent the material streams snd the vertical lines connecting the streams represent heat exchangers. The temperatures of the streams range from source temperature to target temperature, with the hot streams moving from left to right, and the cold streams moving from right to left. The cold utility stream is positioned at the top of the network, and the hot utility stream is positioned at the bottom of the network. The utility streams cover any residual heating or cooling load. Between the material and utility streams are circles with lines between them, representing heat exchangers. The load of the heat exchangers is visible at the top of each heat exchanger. This gives a visual representation of where the heat exchangers are positioned in the system, and the size of each one of them [39].

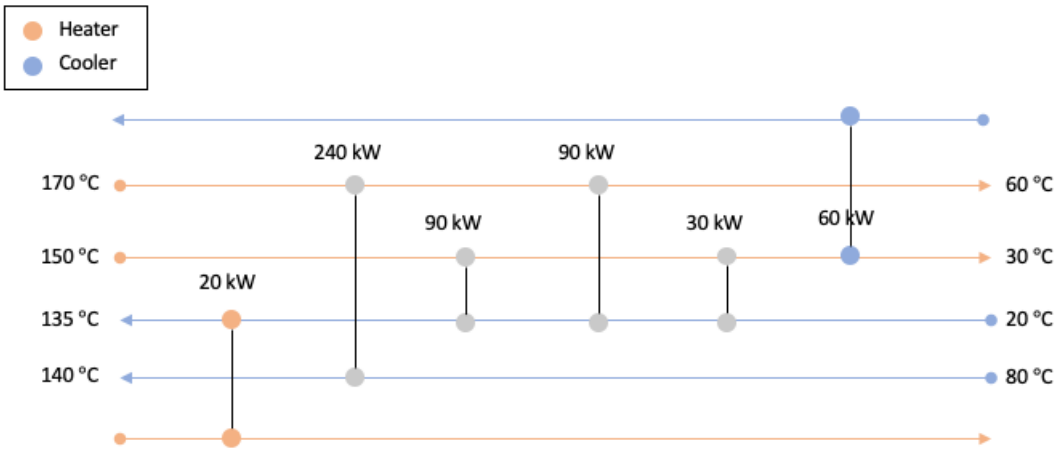

Figure 2.13: *A MER-network of an arbitrary system. Illustration is based on [39].*

While the rules of pinch analysis on a heat exchanger network prohibit heat transfer across pinch, this does not prevent a heat pump from being implemented in the system. A heat pump will effectively transfer heat from below pinch to above pinch. A heat pump can be added between the energy pocket centered around the pinch point. Placing a heat pump only inside the below-pinch range or above-pinch range will result in an increase in cold utility or hot utility, respectively. A heat pump is only correctly placed when waste heat is recycled from below pinch to above pinch. This effectively utilises the energy pocket around the pinch temperature as seen in Figure 2.12 [40].

3 Methodology

This section describes the approaches used, based on the underlying theory of Section 2.

3.1 Model description

The model was divided into four separate sections. These sections were the electrode dryer, the heating and cooling of air with solvent regeneration, dry room dehumidification and the heat pump system for energy recovery. The MER-networks are separate, and regard all the material streams combined. The approach for this is further explained in Section 3.9. The software Aspen HYSYS was chosen as the main simulation program due to its ability to calculate essential values for streams with different material flow. As such, Aspen HYSYS was used for the modeling of air heating and the heat pump system. The actual electrode drying and solvent evaporation process proved more complex in terms of structure, and was thus modeled in the computing software MATLAB. However, some of the results from the computing were used in the main simulation platform. Furthermore, the model for dry room dehumidification system was simulated in Aspen Plus due to the required material properties not being available in the Aspen HYSYS library. Aspen Plus is a very similar software to Aspen HYSYS. The main difference being that Aspen Plus is process focused, while Aspen HYSYS is flow based. The results from Aspen Plus was transferred to HYSYS for the modeling of the convective airflow and heat pump, connecting the air heating with solvent regeneration and dry room dehumidification.

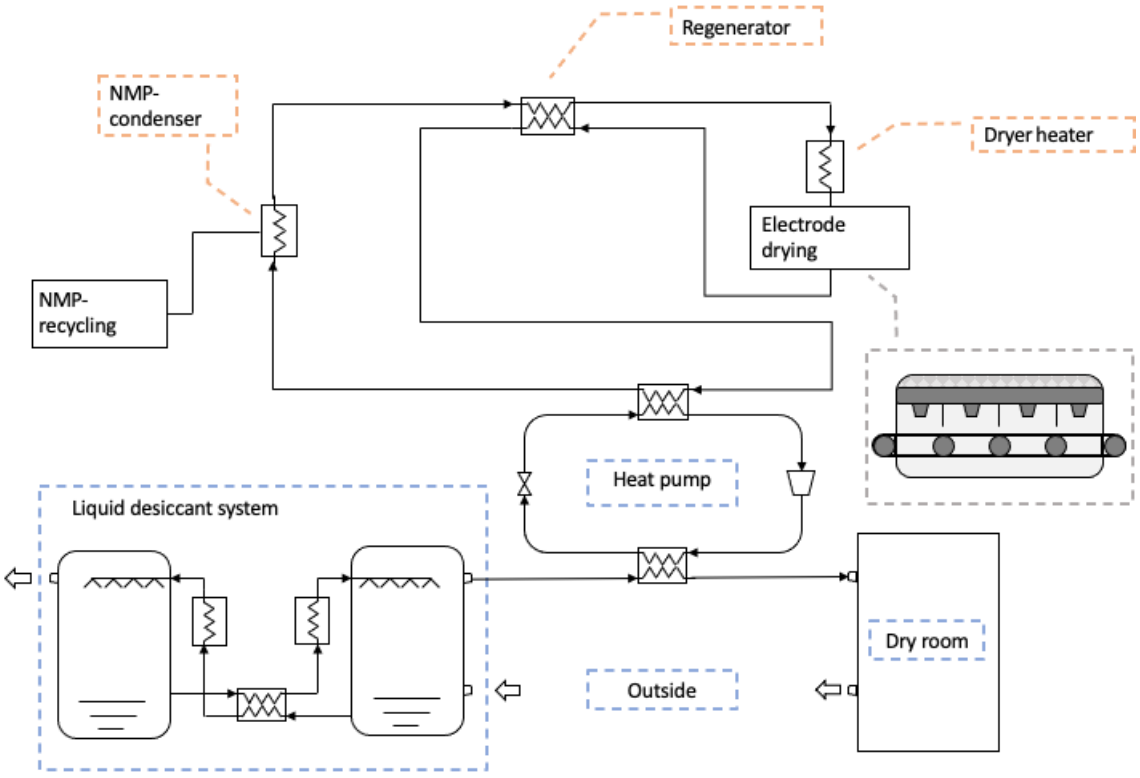

Figure 3.1: *The complete convection process with dryer, heat pump, liquid desiccant system and dry room. The heat pump placement can vary based on different designs. This is one possible configuration. This is also a simplified flowsheet, as the anode and cathode drying units are combined.*

Figure 3.1 depicts how the individual processes of the model are connected. An important note is that Figure 3.1 shows an initial design, and additional, or differently placed, heat exchangers could be more beneficial. The heat pump placement is also reliant on the overall system layout, as should the temperature ranges prove sufficiently high, a regular heat exchanger would be better. Since the heat pump placement is so highly reliant on the rest of the system, the depiction of Figure 3.1 just shows one of the multiple possible configuration for the system. In addition to this, the electrode drying block consists of both the anode and cathode drying. The anode and cathode drying occur separately, but in parallel to one another. Therefore, this schematic is simplified to a greater extend. The anode and cathode drying also contains separate air mass flow. Essentially, there are two of the airflow loops shown in the figure. The anode drying also utilize a regenerator, similarly to the cathode drying process. However, the air does not require any cooling, as it is presumed that water is used as solvent for the anode.

3.2 Evaporation energy for convective drying

This section explains how the evaporation energy and drying time for the convective electrode drying process was found through simulation. It also explains how plots for film thickness, solvent fracture, temperature and drying rate, as a function of time, were created. The total energy for the convective drying consisted of the evaporation energy, explained further in Section 3.4, and the energy required for convection air heating. The model used for air heating and solvent recovery is further explained in Section 3.5. The model is based on the equations presented in Section 2.4.2.

The required evaporation energy and drying time of the convection drying process was simulated using MATLAB. The code used for the simulation consisted of a main script and four additional functions, which derives from the report by Oppegård et al. The first step for modeling the drying process was to declare the initial parameters for the slurry and the ambient air. These initial parameters are displayed in Table 3.1 of Section 4.1.1. The slurry parameters included the individual densities for solvent and solid, as well as specific heat coefficient and molecular weight of the solvent. Equation 2.12 was used to determine the vapor pressure of the ambient air, using its relative humidity and temperature as input variables. The air temperature and air velocity were also preset parameters. However, the parameter for temperature was made adjustable and could be modified to change throughout the process, in order to simulate multistage drying.

Separate functions for total density, transfer coefficients, partial pressure and diffusion coefficient were made in order to calculate the changes in thickness, temperature and solvent concentration of the film over time. The function for density assumed linear relation between solid and solvent, resulting in a total density based on the decreasing solvent fraction. The diffusion coefficient was found similarly by using the volume fraction of the solid, which was calculated from the volume of solvent and solid. Calculation of the diffusion coefficient was done through the implementation of Equation 2.7 in the code, using an activation energy of $7.79 \cdot 10^6$ J/molK and having the empirical constant (γ) set to 1.15. The partial pressure was modeled using the Flory Huggins theory, expressed by Equation 2.11, and using the previously found vapor pressure. Lastly, the heat- and mass transfer coefficient were implemented using Equation 2.3 and 2.9, applying the air velocity as input value, as well as a number of preset parameters displayed in Table 3.1.

With most of the underlying parameters defined, the next step was to specify the simulation time and the subsequent number of steps used for calculation. Similarly to the air velocity, the total simulation time was set to a changeable input parameter. The simulation time was then

divided into steps of 0.01, resulting in calculations for every 0.01 seconds of the total simulation time. The electrode was then divided into 50 different layers, with each step being 0.02 of the total thickness of the film. An increased number of steps resulted in a more accurate simulation. However, the CPU-time in MATLAB drastically increased as a result.

Table 3.1 shows the initial parameters used for the simulation. The density and specific heat coefficient of the solvent was chosen based on NMP, while the density for the solid is an estimation based on the active materials of an arbitrary cathode. The diffusion coefficient was set to a value that issued system stability, while the relative humidity was based on normal room conditions of approximately 35%. The velocity of the air was chosen based on the design in Aspen, which is further explained in section 4.1.5.

Table 3.1: *Initial values used for the simulation of the drying process in MATLAB.*

Initial parameter	**Value**
Thermal conductivity [W/mK]	$30.0 \cdot 10^{-3}$
Dynamic viscosity air [Ns/m^2]	$20.74 \cdot 10^{-6}$
Density air [kg/m^3]	1.009
Air temperature [°C]	140
Air velocity [m/s]	9
Density solvent [kg/m^3]	1030
Density solid [kg/m^3]	4000
Specific heat solvent [J/kgK]	1900
Molecular weight solvent [g/mol]	99.13
Initial film thickness [μm]	157.5
Initial film temperature [K]	330.5
Initial concentration fraction	0.435
Initial diffusion coefficient [m^2/s]	$5.25 \cdot 10^{-9}$
Relative humidity ambient air [%]	35.0

3.2.1 Solving with FDM and FTCS

The modeling was completed using the FDM and the FTCS differential scheme described in Section 2.4.2.8. Applying this to the dimensionless model described in Section 2.4.2.7 resulted in the following equations for thickness (L), temperature (T) and concentration (C):

$$\widetilde{L}^{i+\Delta\widetilde{z}} = -t_0\Delta\widetilde{t}\left(\frac{\kappa_{\mathrm{m}}M_{\mathrm{s}}}{\rho_{\mathrm{f}}RL_0}\right)\cdot\left(\frac{P_{\mathrm{s}}}{\widetilde{T}^iT_0}-\frac{P_{\mathrm{a}}}{T_a}\right)+\widetilde{L}^i$$

$$\widetilde{T}^{i+\Delta\widetilde{z}} = -t_0\Delta\widetilde{t}\left(\frac{\kappa_{\mathrm{m}}M_{\mathrm{s}}\lambda}{\rho_{\mathrm{f}}CpR\widetilde{L}^iL_0}\right)\cdot\left(\frac{P_{\mathrm{s}}}{\widetilde{T}^iT_0^2}-\frac{P_{\mathrm{a}}}{T_aT_0}\right)+\left(\frac{t_0\Delta\widetilde{t}}{\rho_{\mathrm{f}}Cp\widetilde{L}^iL_0T_0}\right)\cdot\dot{q}_{in}-\left(\frac{\widetilde{T}^i\widetilde{L}^{i+\Delta\widetilde{t}}}{\widetilde{L}^i}\right)+2\widetilde{T}^i$$

$$\widetilde{C}_j^{i+\Delta\widetilde{z}} = t_0\Delta\widetilde{t}\left(\frac{\widetilde{D}_j^iD_0}{(\widetilde{L}^iL_0)^2}\right)\cdot\left(\frac{\widetilde{C}_{j+\Delta\widetilde{z}^i}-2\widetilde{C}_j^i+\widetilde{C}_{j-\Delta\widetilde{z}}^i}{\Delta\widetilde{z}^2}\right)+\widetilde{C}_j^i$$

These equations were then implemented. A realistic limit was also set to the film temperature to ensure it did not exceed the temperature of the ambient air. Additionally, a ghost cell was used in order to calculate the concentration of the upper boundary.

3.2.2 Post processing plots

The resulting values for thickness, temperature and concentration at each time of the drying process was saved in the software. Then, the evaporation rate at each stage was found by using Equation 2.16. This evaporation rate was then used to calculate the evaporation energy of the drying process, by the use of Equation 2.15. A condition was then implemented in order to find the time for when the thickness remained approximately constant, signifying the moment of evaporation end. The sum of evaporation energy was then determined using the time period from start to evaporation stop. Subsequent plots could then be made based on the values found. Figure 3.2 shows a flowchart of the approach used for the overall simulation.

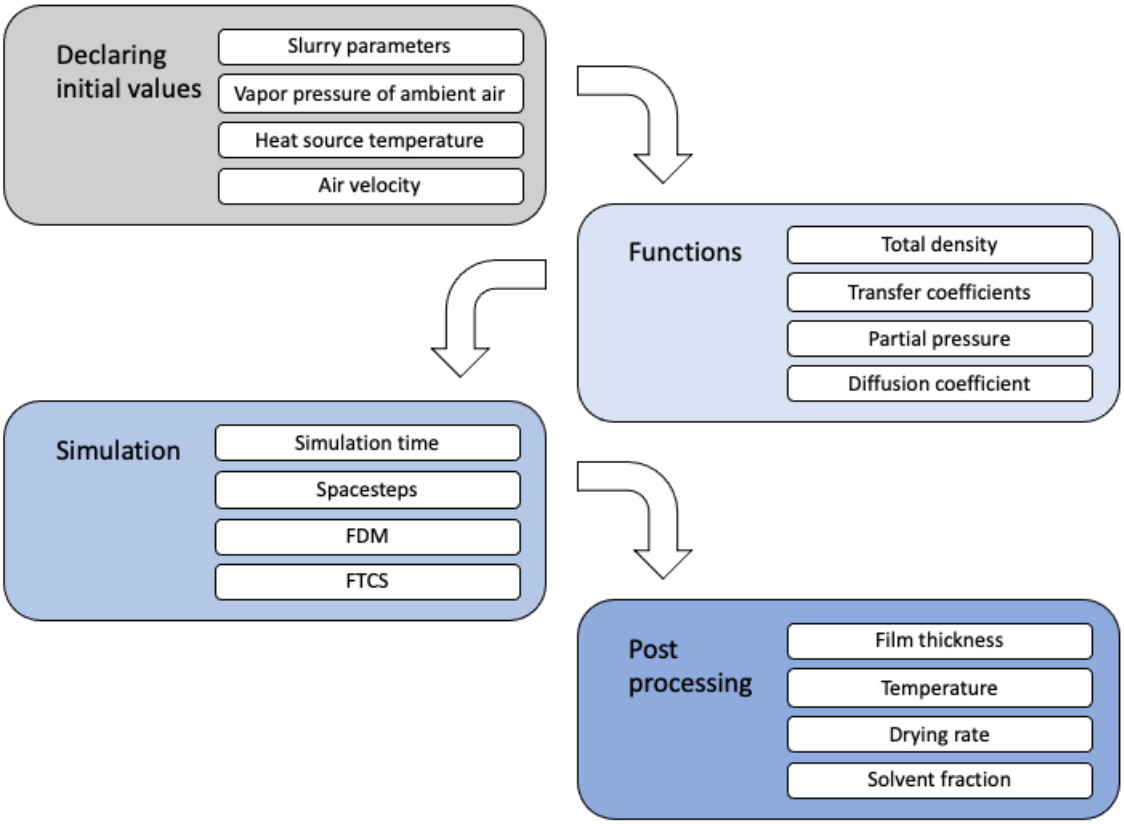

Figure 3.2: *Flowchart depicting the stages used for simulation of the drying process in MATLAB.*

3.3 Evaporation energy for radiation drying

The MATLAB model for simulating the radiation drying process was made similarly to the convection model of Section 3.2. The radiation drying was assumed to have a much lower mass flow rate of air than the convection drying process.

Due to the air not being heated prior to processing, as for convective drying, an additional equation describing the gradual increase in ambient air temperature had to be implemented in the radiation model. This equation for the change in air temperature is based on Equation 2.21, and using the FDM approach result in the following equation for the change in temperature:

$$T_{\mathrm{a,rad}}^{i+\Delta\widetilde{z}} = -t_0\Delta\widetilde{t}\cdot\frac{\kappa_{\mathrm{c}}(T_{\mathrm{b}}-T_{\mathrm{a,rad}}^{i})+\kappa_{\mathrm{c}}(\widetilde{T}^{i}T_0-T_{\mathrm{a}}^{i})+\dot{m}_{\mathrm{evap.}}^{i}Cp(\widetilde{T}^{i}T_0-T_{\mathrm{a,rad}}^{i})}{\rho_{\mathrm{a}}Cp_{\mathrm{a}}+T_{\mathrm{a}}^{i}}$$

The formula for $T_{\mathrm{a,rad}}$ was then implemented in the model of Section 3.2. A limit was also set to hinder the temperature of the air from exceeding the temperature of the new heat source T_{b}. Changes were also made to the heat transfer q_{in}, replacing Equation 2.2 from Section 2.4.1.1 with Equation 2.5 from Section 2.4.1.2.

The initial parameters for thickness, temperature and solvent fraction was set to the values shown in Figure 3.2. Compared to the convective drying process of Section 3.2, the air velocity was changed to 4 m/s and the initial diffusion coefficient was changed to $7.25 \cdot 10^{-9}$ m^2/s. The change was made due to the fundamental difference between the convection and radiation processes, and the diffusion coefficient working as a tuning parameter for the stability of the system. The initial ambient air temperature was set to 27°C. Furthermore, the emissivity was set to an approximated value of 0.725. The option to gradually increase the heat source temperature was also implemented in order to simulate multistage drying. The post processing was executed similarly to the convective drying explained in Section 3.2.2.

Table 3.2: *Initial parameters for the radiation drying simulation in MATLAB.*

Initial parameter	**Value**
Heat source temperature [°C]	140
Air velocity [m/s]	4.00
Density solvent [kg/m^3]	1030
Density solid [kg/m^3]	4000
Specific heat solvent [J/kgK]	1900
Specific heat air [J/kgK]	1000
Molecular weight solvent [g/mol]	99.13
Emissivity	0.725
Initial air temperature [K]	300
Initial film thickness [μm]	157.5
Initial film temperature [K]	330.5
Initial concentration fraction	0.435
Initial diffusion coefficient [nm^2/s]	7.25
Relative humidity ambient air [%]	0.35

3.4 Evaporation energy for different electrode chemistries

Conversion to required power was conducted for the evaporation energy for the convection drying and radiation drying processes. The values for drying time and evaporation energy derive from the simulation method presented in Section 3.2 and 3.3 for convection and radiation, respectively. An approximated 742 m^2 of produced cathode area is chosen for the drying process. A graphite anode is also introduced, using the same produced area of 742 m^2. The densities of each substance is presented in Table 3.3, and the composition of each electrode chemistry is shown in Table 3.4.

Table 3.3: *Densities of the materials present in the electrode chemistries of NMC111, NMC811 and NCA. The anode does not contain any carbon black. Values are derived from the research by Nelson et al.*

	Electrode chemistry	**Active material [kg/m^3]**	**Carbon black [kg/m^3]**	**Binder [kg/m^3]**
Cathode	NMC111	4650	1830	1770
	NMC811	4650	1830	1770
	NCA	4780	1830	1770
Anode	NMC111	2240	-	1100
	NMC811	2200	-	1800
	NCA	2240	-	1100

Table 3.4: *Mixture weight ratio of the electrode chemistries of NMC111, NMC811 and NCA. Values are derived from the research by Nelson et al.*

	Electrode chemistry	**Active material**	**Carbon black**	**Binder**
Cathode	NMC111	0.96	0.02	0.02
	NMC811	0.90	0.05	0.05
	NCA	0.96	0.02	0.02
Anode	NMC111	0.95	0	0.05
	NMC811	0.98	0	0.02
	NCA	0.98	0	0.02

The values of Table 3.3 and 3.4 were then used to determine the density of the solid. With the additional input of solvent density and solvent fraction, the drying time and evaporation energy in kJ/m^2 was found in MATLAB using the approach described in Section 3.2 and 3.3. This in conjunction with the estimated cathode area was then used to determine the required load for the evaporation. Table 3.5 shows the input densities and solvent fraction.

Table 3.5: *Changes to input values used for the MATLAB simulation for convection and radiation, using the electrode chemistries of NMC111, NMC811, NCA and graphite anode.*

	Electrode	**Density solid [kg/m^3]**	**Density solvent [kg/m^3]**	**Solvent fraction**
Cathode	NMC111	4536	1030	0.3243
	NMC811	4365	1030	0.5455
	NCA	4661	1030	0.3243
Anode	NMC111	2183	997	0.5455
	NMC811	2192	997	0.3243
	NCA	2217	997	0.3243

3.5 Convective airflow heating and solvent recovery

For modeling the material stream and energy flow of the electrode drying process, Aspen HYSYS was used. This consisted of defining the material streams out of the electrode drying unit. The material stream from the electrode drying was assumed to be in an enclosed circulation. The stream exits the electrode drying process, and then enters the "Cooling of NMP stream" heat

exchanger where the the stream is cooled and NMP condensate is extracted. The stream is then reheated in a regenerator enabling interplay between the hot and cold stream. The stream is then circulated back to a drying heater, before reentering the electrode drying process. This enclosed circulation of air is displayed at the top of Figure 3.1. The anode and cathode drying were assumed to be parallel processes. The setup for simulation was done by choosing Peng-Robinson as the fluid package and adding air to the composition list. Following this, the menu palette was used to drag and drop streams and components in order to create the flowsheets. For the heat exchangers, the simple model was selected and used. This also includes a basic model for heat loss in the heat exchanger.

For the sake of simplification, a series of assumptions were made. The NMP in the airflow was not accounted for in terms of heat capacity and mass flow rate. The airflow out of the cathode drying unit will in reality contain around 1000 ppm of NMP. However, the airstream composition in Aspen HYSYS was defined as pure air. It is also worth noting that the NMP extraction was not modeled seeing as the majority of the energy consumption is the energy required for the airstream cooling. In reality, NMP would be condensed and removed in the "Cooling of NMP stream" heat exchanger. The NMP condensed from this operation would be further processed in an extraction and collection process. The exact temperature required for a sufficient amount of the NMP to condense from the airflow was also assumed to be 6°C, this was based on Ahmed et al. The exit temperature of the NMP condenser could be set to 6°C as an initial condition. The anode drying system had an almost identical setup, the only difference being that the anode used water as solvent, so no NMP extraction was required. The anode air inlet and outlet was assumed to be 8°C, since this was the assumed ambient temperature.

Further, to optimize the design, a regenerator was incorporated to assist in energy conservation by holding the function of exchanging heat from the hot airflow to the airflow exiting the NMP condenser unit. This significantly lightens the cooling duty of the NMP condenser, while simultaneously assisting in reheating the airstream for reentry into the electrode drying process. The original Aspen HYSYS layout of the electrode drying process design is displayed in Figure 3.3. The connection to the heat pump and the NMP condenser is showed in the bottom right corner of the illustration. The size of this regenerator was designed in order to cater to the required size of the cooling unit of the heat pump system. In other words, the regenerator design had to cover enough of the cooling load so that the energy balance between both sides of the heat pump could be satisfied. This was because the cooling duty of the NMP condenser could not be too large, seeing as this would make interplay using a heat pump between the electrode drying airflow and the airflow into the dry room unnecessary.

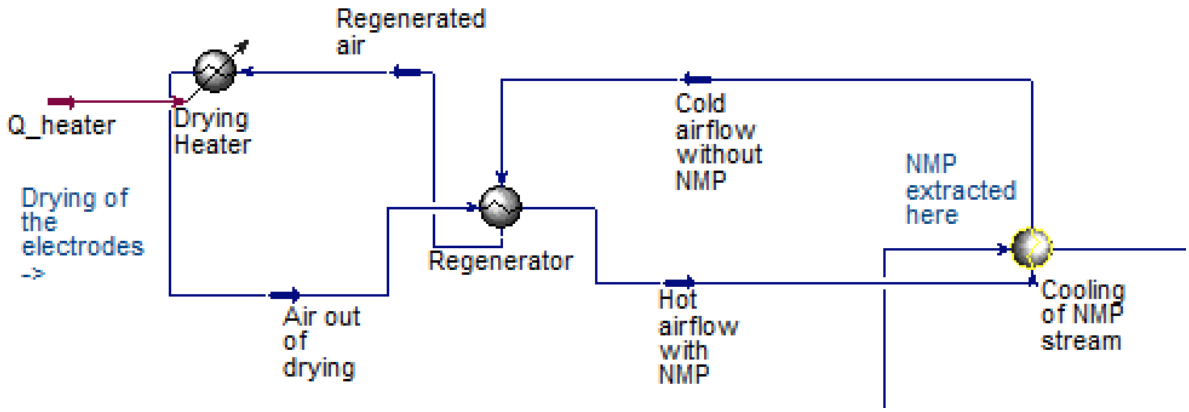

Figure 3.3: *An Aspen HYSYS schematic showing the electrode drying process and how the energy is optimized with a regenerator and heat pump.*

For the heat pump system, which is further explained in Section 3.8, to function, the duty of the condenser and evaporator heat exchangers within the heat pump had to be within ranges of each other. If the regenerator was not sufficiently large, an alternative was to add an additional cooling unit after the heat pump condenser. Depending on the temperature difference between the cold and hot side of the heat pump, a heat pump would be unnecessary and it would be better to use a heat exchanger instead. Incorporating this into the design, allowed the remaining cooling load to be shared by the heat exchanger and the additional cooler, thus still enabling interplay between the electrode drying airflow and the airflow into the dry room.

The added NMP-condenser unit is shown in Figure 3.4. After having implemented this into the flowsheet, the regenerator was tested for different loads, and the impact on the loads of drying heater and NMP condenser were documented. This setup was without the additional heat exchanger or heat pump. The approach used for designing exchanger networks is later presented in Section 3.9. The system was tested for a regenerator sizes of 100 kW, 250 kW and 500 kW. To accomplish this, the duty of regenerator could not be altered directly. Instead, the temperature ranges on both the shell and tube side of the regenerator had to be altered to correspond to the different regenerator loads when testing. These simulations were done for a mass flow rate of 9 kg/s for the airflow from cathode drying.

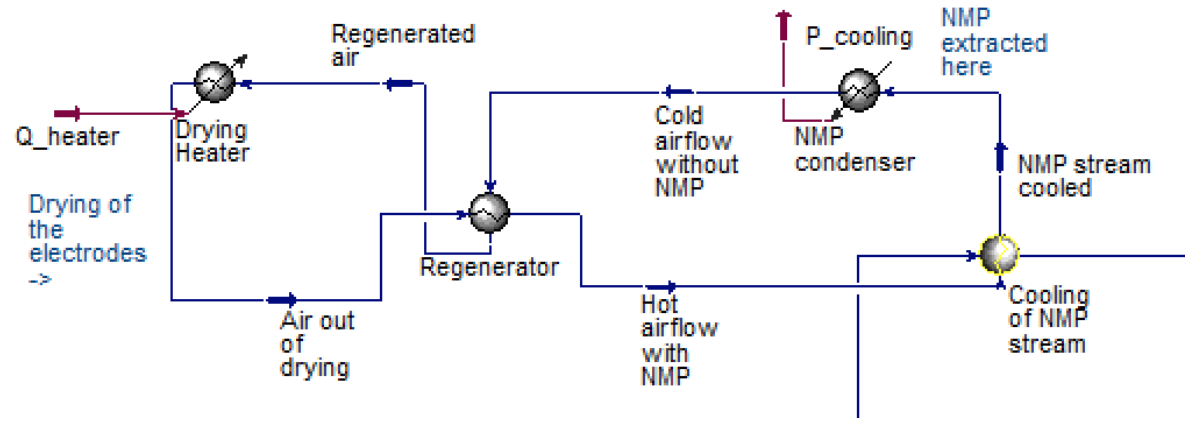

Figure 3.4: *Configuration of the drying-solvent regeneration system with an additional cooler and the heat pump replaced with a heat exchanger.*

The design with the additional cooler to lighten the energy load on the regenerator is displayed in Figure 3.4. Note that components being yellow in Aspen HYSYS generally means that they are either missing input values or unconverged due to overspecification. However, in this case the errors were generally ±1 kW and resulted from slight inconsistencies in the inputted temperature ranges for the shell and tube side of the heat exchanger. Additionally, the contact area for the heat exchangers was also calculated based on the underlying theory presented in Section 2.6.1.1. Different regenerator sizes and duties were tested to regard how the regenerator impacts the total energy consumption.

3.6 Radiation heating

Due to the complexity of modeling a radiation drying heat source, the required load was instead determined based on engineering estimations and an approximated heat flux using Equation 2.5. Table 3.6 list the assumptions made for the radiation drying process. The electrode area per batch was estimated as previously explained in Section 3.4.

Table 3.6: *Assumptions for the radiation drying process.*

Aspect	Assumption
Electrode area per batch	742 m^2
Heat flux	1 kW/m^2
Start temperature	8°C
Target temperature	140°C

3.7 Dry room dehumidification model

The function and setup of the desiccant system is based on the underlying theory explained in Section 2.5.1. The main component used in the desiccant system is an absorber column. The resulting flowsheet and setup used for simulation is displayed in Figure 3.5. In the figure, the absorber column is named ABSCOL. Additionally, the airflow inlet and outlet of the column corresponds to the material streams AIR-IN and AIR-OUT, respectively. The desiccant inlet and outlet streams were also named DES-IN and DES-OUT, respectively. The stream AIR-DR corresponds to the air entering the dry room.

The absorber column design had to be simulated using Aspen Plus, as the Aspen HYSYS software did not have the required material data for the liquid desiccant. The desiccant used for modeling was calcium chloride. As with the HYSYS model, the fluid package was set to Peng-Robinson and the materials were defined before commencing simulation. The working medium of the desiccant system was assumed to be 0.65 mass% water and 0.35 mass% calcium chloride. It is worth noting that changing the composition values or using a different desiccant would have an impact on the results. The desiccant setup in Aspen Plus is shown in Figure 3.5. Here, the airflow inlet and outlet are connected to the absorber column at the right, while the desiccant inlet and outlet streams are located to the left of the absorber column. The airflow inlet is assumed to be 0.05 mass% water and 0.95 mass% air, this corresponds to approximately 70% relative humidity. The desiccant heating and cooling loads are determined by the required temperature ranges for the desiccant. The desiccant outlet is heated to 100°C by the desiccant heater, denoted DES-H, which is assumed to be sufficient for evaporating and removing the previously absorbed water.

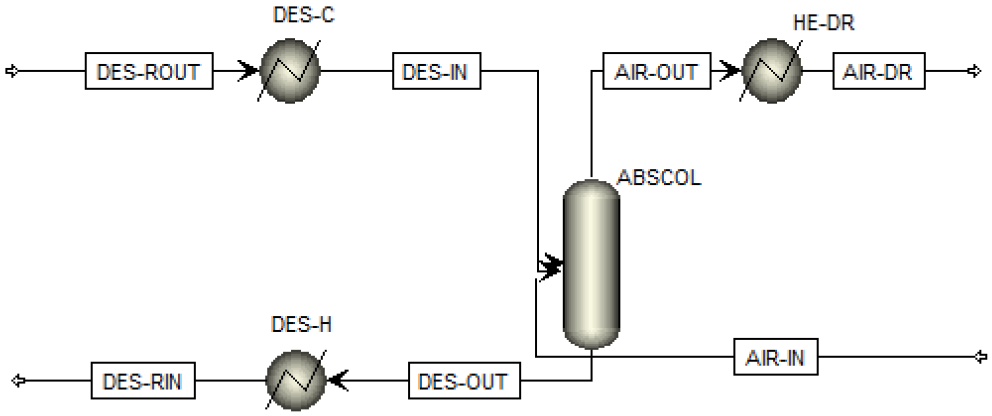

Figure 3.5: *Flowsheet of the desiccant system design in Aspen Plus.*

The absorber column is a simultaneous mass and heat transfer system that is computed by the built in solver in Aspen Plus. Geometry values of the column, such as the height and number of stages, were inputted. Here, a total of 11 stages were used with a total packing height of four meters. The diameter was also changed to one meter in order for the absorber column to be large enough to avoid flooding. After having solved for the desiccant system, values such as the temperature ranges, and required heating and cooling energies within the desiccant system was further implemented into the other systems. The reason being to evaluate the potential for interplay with other streams such as the heat pump. In reality, the desiccant inlet and desiccant outlet streams would be connected to an evaporation unit that removes the excess water content within the desiccant outlet stream. This was not simulated in Aspen Plus. However, the assumption was made that the absorbed water be removed here.

Additionally, the required pressures for the absorber column are relatively high. The pressure for the absorber column can be found iteratively, and through testing different ranges and observing whether the results converge. In reality, a compressor would be required to achieve the required pressures. However, for simplification, this was not implemented into the flowsheet model. The absorber column was set to operate at around 15 bar based on several iterations. The airflow therefore needs to enter at a similar pressure. The desiccant system was tested for different desiccant mass flow rates, inlet temperatures and also for varying air mass flow rates. Table 3.7 shows the parameters used for the simulation in Aspen Plus. The results were documented and summarized. Note that a heat exchanger, or potentially a heat pump, could be connected to the desiccant system. The approach used for exploring the potential of this is explained in further in Section 3.9.

Table 3.7: *Initial parameters used for the desiccant system in Aspen Plus.*

Initial parameter	**Value**
Mass flow ambient air inlet [kg/h]	32 000
Mass flow desiccant inlet [kg/h]	2 000
Temperature ambient air inlet [°C]	8
Temperature desiccant inlet [°C]	25
Temperature dry room [°C]	23
Height of packing [m]	4
Diameter absorber column [m]	1

3.8 Heat pump implementation

This section explains how a heat pump can be implemented and how this is modeled.

3.8.1 Initialization and simulation setup

The first step in the modeling process was creating a new case in Aspen HYSYS and defining materials and composition under the properties section. This was done by searching for all the relevant materials and using the "add" function. This created a component list that can be used for later simulations. The components added in this section were air, water, R-22 (Chlorodifluoromethane), R-134a (Tetrafluoroethane) and R-600a (isobuthane). The reasoning behind the choice of refrigerants was based on availability and additionally their respective thermodynamic characteristics. The condensation and evaporation temperature and pressure characteristics were the most significant for the heat pump to operate under optimal conditions as based on theory presented in Section 2.6.1. Further, a fluid package, or solver method, had to be selected under the fluid packages file in the tree menu. The fluid package chosen depends on the temperature and pressure ranges, as well as the type of components selected in the previous step. Aspen HYSYS provides a wide selection of fluid packages, but for this purpose the Peng-Robinson equation of state was used. Later on, the results were compared with other equations of state such as the SRK package in order to evaluate its significance and determine any error due to equation of state selection. Having selected the initial conditions for the model, the simulation part of the project could start.

3.8.2 Heat pump design

Simulation in Aspen HYSYS was conducted by selecting the simulation tab in the bottom left, and then dragging the relevant components into the the blank project slate provided by the software. For this project, the heat pump schematic was completed last, since the heat pump configuration is reliant on the streams it is connected to. The heat pump schematic was created using the underlying theory presented in Section 2.6.1. The main function of the heat pump was to connect the convective airstream from the electrode drying process and the dry room for design cases where the temperature ranges made it impossible to use a heat exchanger instead. In order to begin setup of the heat pump, initial conditions for mass flow rate and temperatures in certain points of the streams connected to the heat pump were determined. Specifically for the material stream into the dry room, which was connected to the condenser side of the heat pump. The outlet temperature of air from the desiccant system was based on results from the desiccant simulation and was set to 8°C. The mass flow rate was set to 32 000 kg/s for the

air entering the dry room. The electrode drying stream was set to be cooled to 6°C for NMP extraction with a mass flow rate of 9 kg/s. These initial conditions were also required for the airflow exiting the convective electrode drying process. This yielded an estimate towards the required and available energy in the drying room and drying process sections connected by the heat pump.

When designing the heat pump, two shell and tube heat exchangers were used and named NMP stream cooling and dry room heater as seen in Figure 3.6. For the heat exchangers, the minimum temperature difference approach was used. This concept is explained in Section 2.6.1.1. The minimum temperature difference was defined by selecting the heat exchanger, going to specifications and adding a desired value for the minimum temperature difference. For this project, the minimum temperature difference for all heat exchangers was 10°C. The expansion valve and compressor components were also selected from the palette menu to the side in Aspen HYSYS. For the compressor, an energy stream was defined for the electrical power that has to be applied to operate the compressor. To connect the individual components, a material stream from the palette menu was dragged between each component. These material streams could be named, but this is not strictly necessary. Following this, each component was selected and the input and output streams were defined to the corresponding input and output for the component. The final design for the heat pump is displayed in Figure 3.6. The additional material flows that move outside the scope of the figure are connected to the drying room and the electrode drying process.

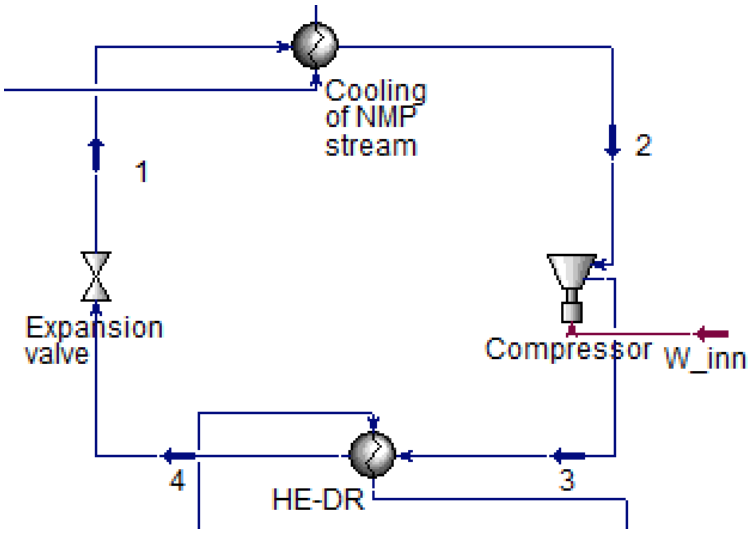

Figure 3.6: *The heat pump layout designed in Aspen HYSYS.*

For the heat pump system, a set of operation parameters were determined for the heat pump to be able to function under optimal conditions. These values were mostly for the mass fractions and phase states of the working medium in the heat pump. The input values and assumptions made for the phase states and other relevant parameters is displayed in Table 3.8. The pressure in stage 1 and in stage 2 of the material streams were set to be equal. This was also the case for the pressure in stage 3 and 4 of the heat pump system. This is based on the underlying theory presented in Section 2.6.1.

Table 3.8: *Initial heat pump input for optimal operating conditions.*

Stage	1	2	3	4
Pressure [bar]	$p_1 = p_2$		$p_3 = p_4$	
Phase fraction	-	1	1	0
Temperature [°C]	$T_1 = T_2$		$T_3 = T_4$	

3.9 Energy optimization using pinch analysis

The pinch analysis was performed using Aspen Energy Analyser. The streams inputted to the software, and how they are connected and related to each other are displayed in Figure 3.7. This was the basis for simulation. The streams shown in the figure are categorized as hot and cold. The cold streams are in need of heating, while hot streams are in need of cooling. The figure also shows all the material streams involved in the production process. These streams consisted of three groups. The first of these group was the anode streams, with both inlet and outlet from the drying process. Secondly, the cathode streams were connected between the drying process and the NMP recycling unit. Finally, the dry room streams consisted of the two streams within the desiccant system, between the absorber and regenerator column, as well as the airflow into the dry room. The streams presented here essentially represent the total system before any connections were made.

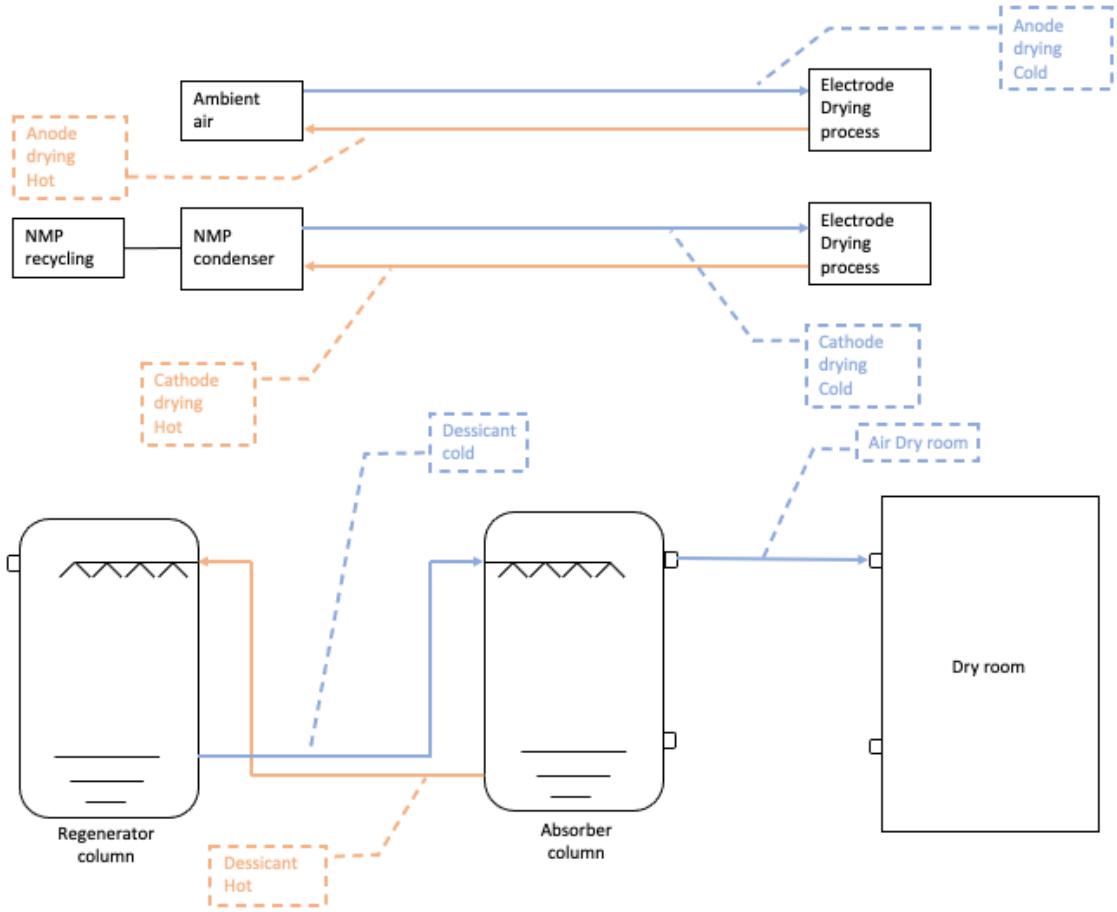

Figure 3.7: *The material streams in the combined process.*

The analysis was started by opening a new project and inputting values for the stream temperatures and mass flow rates. These values were based on assumptions explained in Section 3.5 and 3.7. The initial values are presented in Table 3.9. Note that the heat capacity values for the desiccant was calculated from a mixture of 0.35 mass% $CaCl_2$ and 0.65 mass% water.

Table 3.9: *The input values for the pinch analysis in Aspen Energy Analyser.*

Stream	**Temperature range [°C]**	**Mass flow rate [kg/h]**	**Heat capacity [kJ/kgK]**
Desiccant hot	78-25	2 000	3.71
Desiccant cold	6-100	2 000	3.71
Air Dry room	5-23	32 000	1.00
Cathode hot	140-6	34 200	1.00
Cathode cold	6-140	34 200	1.00
Anode hot	140-8	34 200	1.00
Anode cold	8-140	34 200	1.00

Having inputted the relevant parameters based on figure 3.7, Aspen Energy Analyser then calculated the required heating and cooling for the system based on the pinch approach explained in Section 2.7. Aspen Energy Analyser also yields composite curves and grand composite curves. The pinch temperature is important to keep in mind when evaluating these. The minimum temperature difference was set to 10°C, since this is pretty standard for most industrial processes. Aspen Energy Analyser was also able to design a MER-network, based on the input streams. The number of stream splits allowed was set to none, in order to simplify the design. The design yielded the energy requirements and heat exchanger sizes required for the design. The software then outputted a series of different designs based on the pinch approach. The simplicity of the designs as well as the total costs were considered. The design approach the software uses was based on the pinch principles presented in Section 2.7.

3.10 Calculating total load and watt-hour ratio

The total load was found by adding the individual loads of evaporation energy, heating source and dry room. The loads of these steps were found as explained in Section 3.4, 3.5 and 3.7, respectively. A radiation heat source was also considered, as explained in Section 3.6. By utilizing the number of different setups, and assuming a continuous production of 24 hours a day for 300 days, the total yearly energy demand was found for each process scenario.

Table 3.10: *Estimated electrode parameters.*

Chemistry	**Single cathode [m^2]**	**Capacity per cell [Wh]**	**Cathodes per cell**
NMC111	0.009858	109	75
NMC811	0.008950	108	80
NCA	0.008624	109	85

In Section 3.4 the electrode area was assumed to be 742 m^2 per batch for all electrode chemistries. Table 3.10 shows an estimation of the cathode parameters by Nelson et al. Using these parameters, the yearly capacity was calculated for each electrode chemistry. Dividing the previously found total load of each setup by this calculated value resulted in an estimate for the

watt-hour energy per watt-hour battery. This was done for all the different designs and concepts modeled in order to compare them to each other and the standard industry values.

4 Results

The simulations and results of this section originate from the approach described in Section 3, and are based on the underlying theory presented in Section 2.

4.1 Electrode drying with convection and radiation heating

Two separate process simulation software were used for the convective drying process. These were MATLAB and Aspen HYSYS. For the simulation in MATLAB, only a cathode using NMP as solvent was considered. These simulations were primarily used for plotting the electrode parameters and drying rate as a function of time, as well as calculate the evaporation energy of the electrode and the required time for evaporation. Aspen HYSYS was used in order to determine the energy requirement for maintaining a hot air stream within the dryer. A regenerative unit was also considered for this step. The radiation drying system was similarly simulated in MATLAB, resulting in the same outputs as the convective drying process. The energy needed for the heating units were calculated as well.

4.1.1 Model for electrode drying with convective heating

The simulation for the convective drying of the electrode was conducted in MATLAB as described in section 3.2. Simulation using the initial values of Table 3.1 resulted in an evaporation energy of 49.4 kJ/m^2 with a required drying time of 23.3 minutes. Figure 4.1 shows an overview of changes in film thickness, film temperature, solvent concentration and drying rate.

Analyzing the graphs of Figure 4.1 it is observed that the film thickness and solvent fraction follow a similar pattern, indicating that the thickness of the film decreases as the solvent evaporates. Furthermore, the simulation showed a 67% decrease in the film thickness during the 23.3 minutes of drying. Similarly, the solvent fraction decreased from 0.45 to 0.07 during the same time period. The temperature of the film grew quickly from its initial temperature to the temperature of the ambient air. This takes approximately 54 seconds.

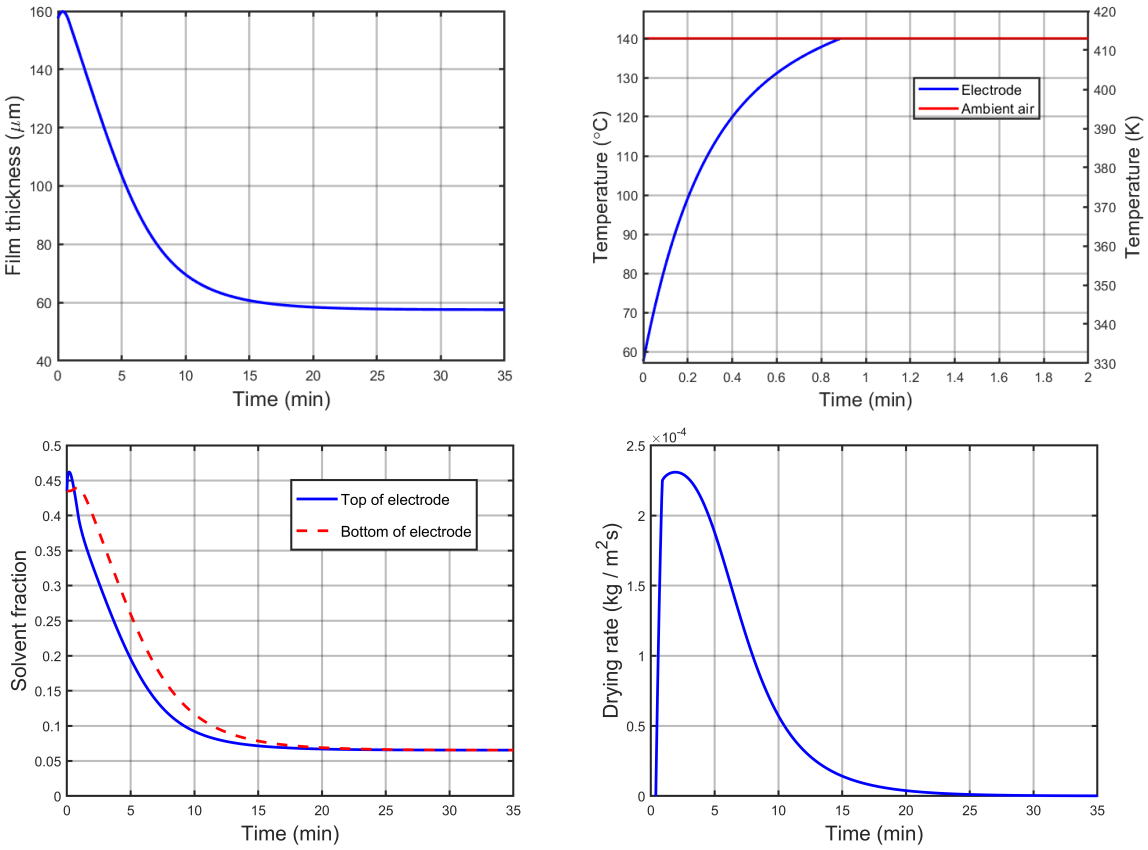

Figure 4.1: *An overview of film thickness, temperatures, solvent concentration and drying rate as a function of time. Graphs derive from the simulations of the convective drying model using the initial parameters of Table 3.1.*

Changes in the initial parameters of the film also exhibit an impact on the final results. Table 4.1 shows how the change in film thickness affect the required evaporation energy and drying time. Similarly, Table 4.2 shows the resulting changes of varying initial solvent fraction. Additionally, Table 4.3 shows the results of changes in initial film temperature, and Table 4.4 shows the results of changes in initial diffusion coefficient.

Increasing the initial film thickness is observed to increase the drying time and required energy for evaporation. An increase in initial solvent fraction, however, causes a decrease in drying time and an increase in evaporation energy. The initial film temperature show minor changes. Meanwhile, the initial diffusion coefficient is paramount for the stability of the system, and as such, display substantial changes in results when changed.

Table 4.1: *The evaporation energy and required drying time for the convective drying process using initial film thickness of between 80 μm and 240 μm.*

Initial film thickness [μm]	**Evaporation energy** [kJ/m^2]	**Time required** [min]
80	26.6	15.5
120	39.5	23.1
160	51.9	30.9
200	64.0	38.9
240	75.7	47.0

Table 4.2: *The evaporation energy and required drying time for the convective drying process using different values for initial solvent fraction.*

Initial solvent fraction	**Evaporation energy** [kJ/m^2]	**Time required** [min]
0.324	43.5	35.0
0.380	47.8	32.4
0.435	51.2	30.4
0.490	54.0	29.0
0.546	56.3	28.0

Table 4.3: *The evaporation energy and required drying time for the convective drying process using initial film temperature values between 10°C and 105°C.*

Initial film temperature [°C]	**Evaporation energy** [kJ/m^2]	**Time required** [min]
10	51.0	30.7
34	51.1	30.6
58	51.2	30.4
82	51.2	30.2
105	51.2	30.0

Table 4.4: *The evaporation energy and required drying time for the convective drying process using different values for initial diffusion coefficient.*

Initial diffusion coef. [m^2/s]	**Evaporation energy** [kJ/m^2]	**Time required** [min]
$0.500 \cdot 10^{-9}$	36.8	97.3
$2.40 \cdot 10^{-9}$	48.2	37.9
$4.30 \cdot 10^{-9}$	50.6	31.7
$6.20 \cdot 10^{-9}$	51.5	29.6
$8.10 \cdot 10^{-9}$	52.0	28.6
$10.0 \cdot 10^{-9}$	52.3	28.0

The ambient air conditions also have significance towards the end results. For this experiment, these external parameters are limited to air velocity, air temperature and air humidity, inside the dryer. Table 4.5, 4.6 and 4.7 shows the effects of different air velocities, temperatures, and humidities, respectively.

From these tables, it is observed that an increase in air velocity and air temperature results in a shorter drying time, as well as a lower evaporation energy. On the other hand, increasing the relative humidity cases an increased drying time. However, the evaporation energy is also decreased as a result.

Table 4.5: *The evaporation energy and required drying time for the convective drying process using air velocities ranging from 4* m/s *to 24* m/s.

Air velocity [m/s]	**Evaporation energy** [kJ/m^2]	**Time required** [min]
4.00	52.2	48.6
8.00	51.4	32.4
12.0	50.6	26.4
16.0	49.8	23.2
20.0	49.1	21.4
24.0	48.4	20.3

Table 4.6: *The evaporation energy and required drying time for the convective drying process using air temperatures ranging from 80*°C *and 140*°C.

Air temperature [°C]	**Evaporation energy** [kJ/m^2]	**Time required** [min]
80	56.9	130
90	55.8	90.2
100	54.6	64.4
110	53.3	47.4
120	52.1	36.1
130	50.8	28.4
140	49.4	23.3

Table 4.7: *The evaporation energy and required drying time for the convective drying process using relative air humidity ranging from 10% to 50%.*

Relative humidity air [%]	**Evaporation energy** [kJ/m^2]	**Time required** [min]
10	53.3	28.3
20	53.2	28.2
30	51.2	30.4
40	47.7	35.6
50	42.3	47.0

Figure 4.2 shows an overview of how the changes in initial film thickness, initial solvent fraction, initial diffusion coefficient, air temperature, air velocity, and relative humidity of the air affect the drying rate of the convective drying process. Here, the graphs derives from the values presented in the aforementioned tables, and their shapes are similar to those presented in the study by Oppegård et al.

The graphs created by the model depicts a right-hand shift in drying rate with an increased film thickness. The same is true for the solvent fraction. Although, this is only accurate for the beginning of the process. A cross occurs at certain point, resulting in a shorter drying time when using higher solvent fractions. The stability of the model is presented by the diffusion coefficient, which at lower values shows a drastic reduction of the drying rate. Examining the graphs for the environmental parameters of ambient air temperature, wind velocity and relative humidity, reveal a noticeable trend. An increase in ambient air temperature and velocity results in a higher initial drying rate, and thus a lower drying time. Meanwhile, an increase in relative humidity results in the opposite, as drying time increases with higher air humidity.

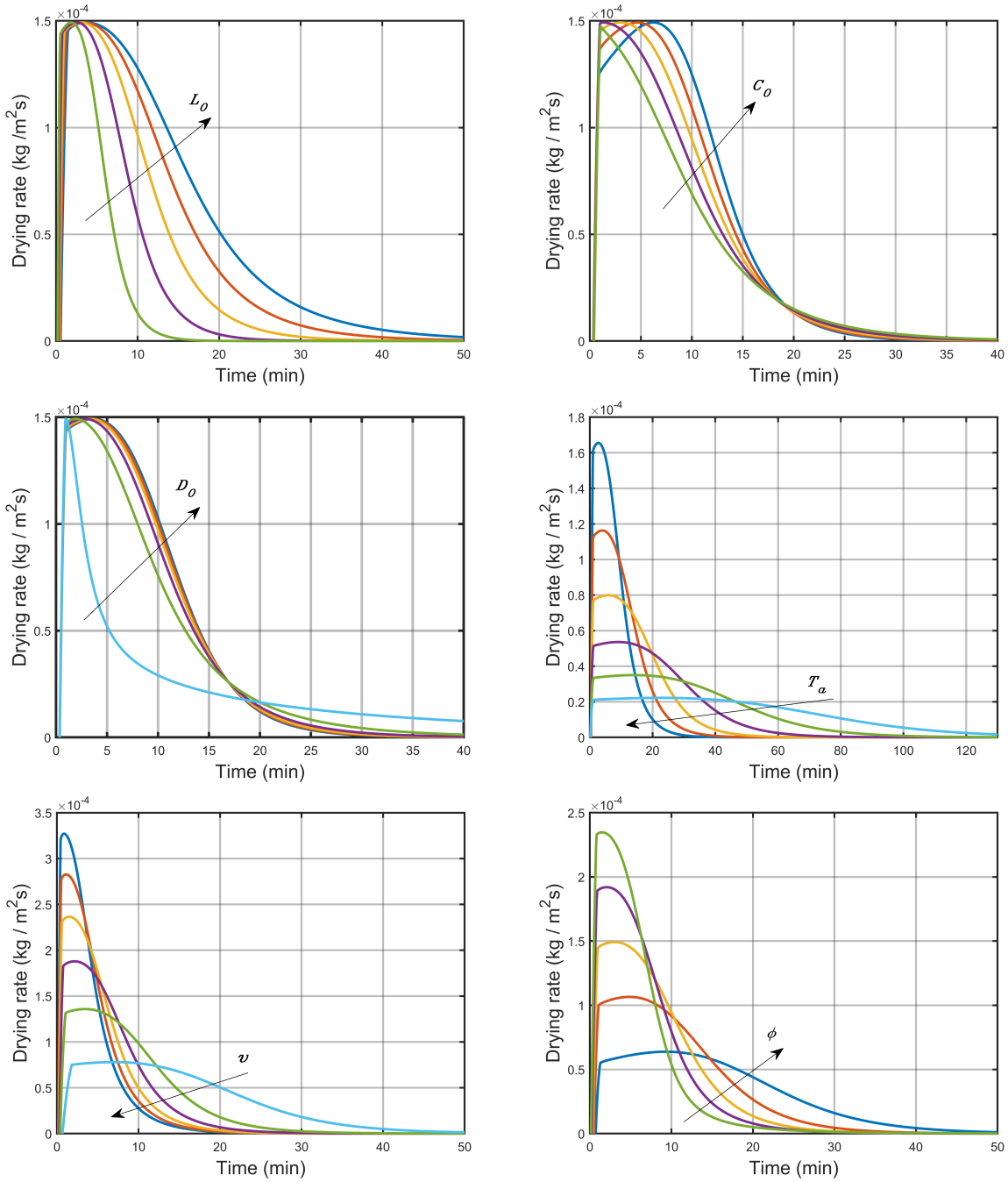

Figure 4.2: *The changes in drying rate caused by adjustments to initial parameters for the convection drying process.* L_0 *is initial thickness,* C_0 *is initial solvent fraction,* D_0 *is initial diffusion coefficient,* T_a *is hot air temperature,* v *is air velocity, and* ϕ *is the relative humidity of the air. The arrow direction represent an increase in input value.*

Figure 4.3 shows how a simulated multistage drying affects the drying rate of the process. The air velocities was set to 14 m/s instead of the 9 m/s used previously. This was done in order to decrease drying time while maintaining lower temperatures, which resulted in easier comparison between the simulations. The air temperature was set to a starting value of 80°C, increasing to 95°C at the 2 minute mark, and 115°C after 5 minutes.

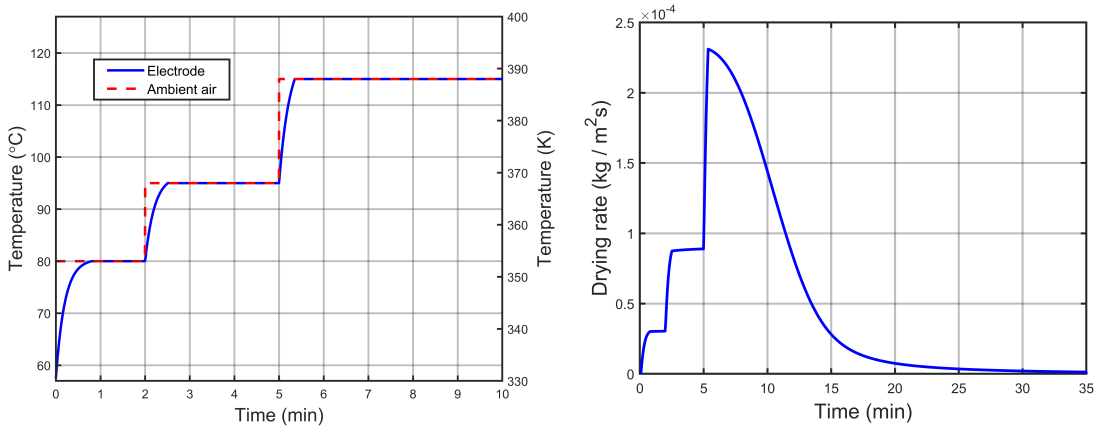

Figure 4.3: *Temperature and drying rate as a function of time in a multistage convective drying process.*

The evaporation energy using multistage drying at an air velocity of 14 m/s resulted in 53.8 kJ/m^2, while the required drying time was 32.3 minutes. A comparison of the drying rates for the different temperature scenarios are shown in Figure 4.4. Table 4.8 displays the evaporation energy and required drying time for each process.

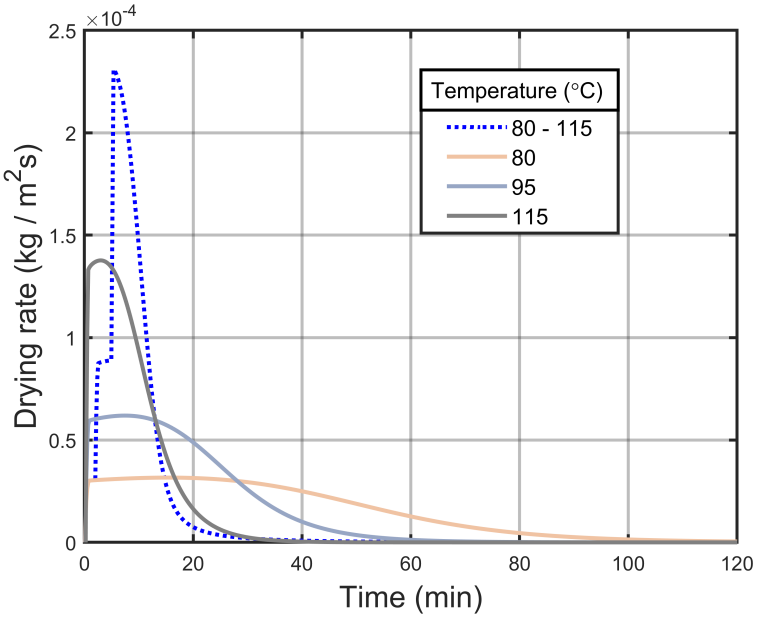

Figure 4.4: *Comparison of drying rates for convective drying. The multi-stage drying utilizes air temperatures between 80°C and 115°C, which is represented by the dotted line. The remaining lines show single-stage drying at temperatures 80°C, 95°C and 115°C, represented by the cyan, orange and grey line, respectively.*

Figure 4.4 shows that the multi-stage drying process experience a noticeable spike in drying rate at the inception of the second temperature increase. The resulting peak in drying rate surpasses that of the single stage process of 115°C by a factor of 1.54. The single-stage drying processes of 80°C, 95°C and 115°C exhibit the same pattern as previously observed in Figure 4.1.

Table 4.8: *The evaporation energy and required drying time for the convective drying simulations using multi-stage compared to single-stage.*

Temperature [°C]	**Evaporation energy** [kJ/m^2]	**Time required** [min]
80 - 115	53.8	32.3
80	57.0	97.7
95	55.0	57.5
115	52.1	32.2

From Table 4.8 it is observed that the drying time of the multi-stage drying process is approximately equal to that of the single-stage for 115°C. A difference in evaporation energy is also noticeable.

4.1.2 Model for electrode drying with radiation heating

The simulation of the radiation drying of the electrode was conducted in MATLAB as described in Section 3.3. Initial parameters are presented similar to that of the convective drying process, shown in Section 4.1.1, which is based on a cathode with NMP solvent drying at 140°C.

Table 3.2 shows the initial values used for the radiation drying simulation. The heat source temperature of 140°C was chosen in order to acquire the lowest possible drying time for the simulation. Meanwhile, the air velocity is a constant for the model design, and thus selected to 4.00 m/s.

Simulation using the initial values of Table 3.2 resulted in a required evaporation energy of 52.8 kJ/m^2 and a drying time of 13.4 minutes for the top of the electrode. Figure 4.5 shows the changes in film thickness, solvent fraction, drying rate, air temperature and electrode temperature as a function of time.

The graph shows a correlation between film thickness and solvent fraction. Through the drying process, the electrode experience an approximately 65% decrease in thickness. Meanwhile, the solvent fraction is reduced from its initial value of 0.435 to zero during the process. The temperature of the electrode is instantaneously increased to the same temperature as the heat source, while the ambient air gradually increases to the same value, albeit from its initial room temperature. The drying rate shows a similar spike in value for the start of the process. Although, it is followed by a steep slope before reaching zero, indicating the end of the drying process.

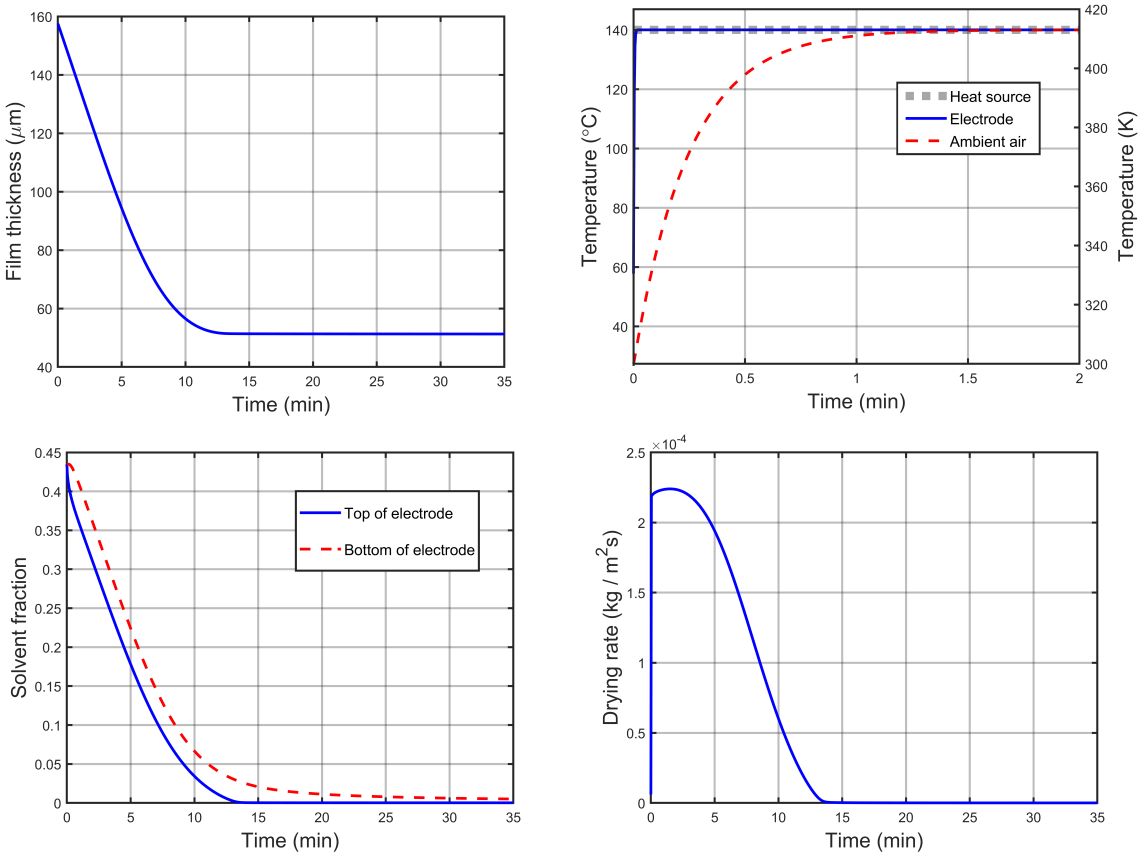

Figure 4.5: *An overview of the graphs for film thickness, temperature, solvent concentration and drying rate as a function of time using the initial parameters of Table 3.1.*

The final results differ by a varying degree based on the values of the initial parameters. Tables 4.9, 4.10 and 4.11 shows how the required evaporation energy and drying time change based on differences in film thickness, solvent fraction, and diffusion coefficient, respectively.

Most notable is the impact of changing the initial film thickness. An increase in this parameter causes an evident increase in drying time and evaporation energy. Similarly, an increase in initial solvent fraction results in an increased evaporation energy. However, the drying time is almost unaffected. The initial diffusion coefficient also exhibits a noteworthy impact on drying time and evaporation energy. This is mainly due to the shift in stability of the system that is caused by its change in value.

Table 4.9: *The evaporation energy and required time for the radiation drying process using different initial film thickness.*

Initial film thickness [μm]	**Evaporation energy** [kJ/m^2]	**Time required** [min]
80	25.5	13.1
120	43.7	17.7
160	56.8	22.3
200	69.1	26.7
240	80.8	30.8

Table 4.10: *The evaporation energy and required time for the radiation drying process using different initial solvent fraction.*

Initial solvent fraction	**Evaporation energy** [kJ/m^2]	**Time required** [min]
0.324	48.3	21.9
0.380	52.6	22.0
0.435	56.0	22.1
0.490	58.7	22.1
0.546	60.8	22.2

Table 4.11: *The evaporation energy and required time for the convective drying process using different initial diffusion coefficients.*

Initial diffusion coef. [m^2/s]	**Evaporation energy** [kJ/m^2]	**Time required** [min]
$2.50 \cdot 10^{-9}$	45.3	17.5
$4.00 \cdot 10^{-9}$	51.4	19.9
$5.50 \cdot 10^{-9}$	54.2	21.2
$7.00 \cdot 10^{-9}$	55.8	22.0
$8.50 \cdot 10^{-9}$	56.8	22.7
$10.0 \cdot 10^{-9}$	57.6	23.2

Relative humidity has neglectable effect on the total drying time and evaporation energy, when using radiation drying. Similarly, the initial film temperature shows no impact on final results due to the rapidness of its temperature increase at the start of the process. Thus, tables for these parameters are not included. The air velocity is considered a constant for all simulations, as its primary function is to transport the vaporised solvent. Table 4.12 shows how changes in heat source temperature influence the resulting evaporation energy and drying time.

Table 4.12: *The evaporation energy and required time for the radiation drying process with heat source temperature ranging from 80°C and 140°C.*

Heat source temperature [°C]	**Evaporation energy** [kJ/m^2]	**Time required** [min]
80	65.2	150
90	63.7	99.0
100	61.9	65.6
110	59.8	43.6
120	57.6	29.2
130	55.3	19.7
140	52.8	13.4

Figure 4.6 shows how changes in the initial parameters for film thickness, solvent fraction, diffusion coefficient and heat source temperature affect the drying rate for the radiation drying process. The values for the graphs derive from the aforementioned tables.

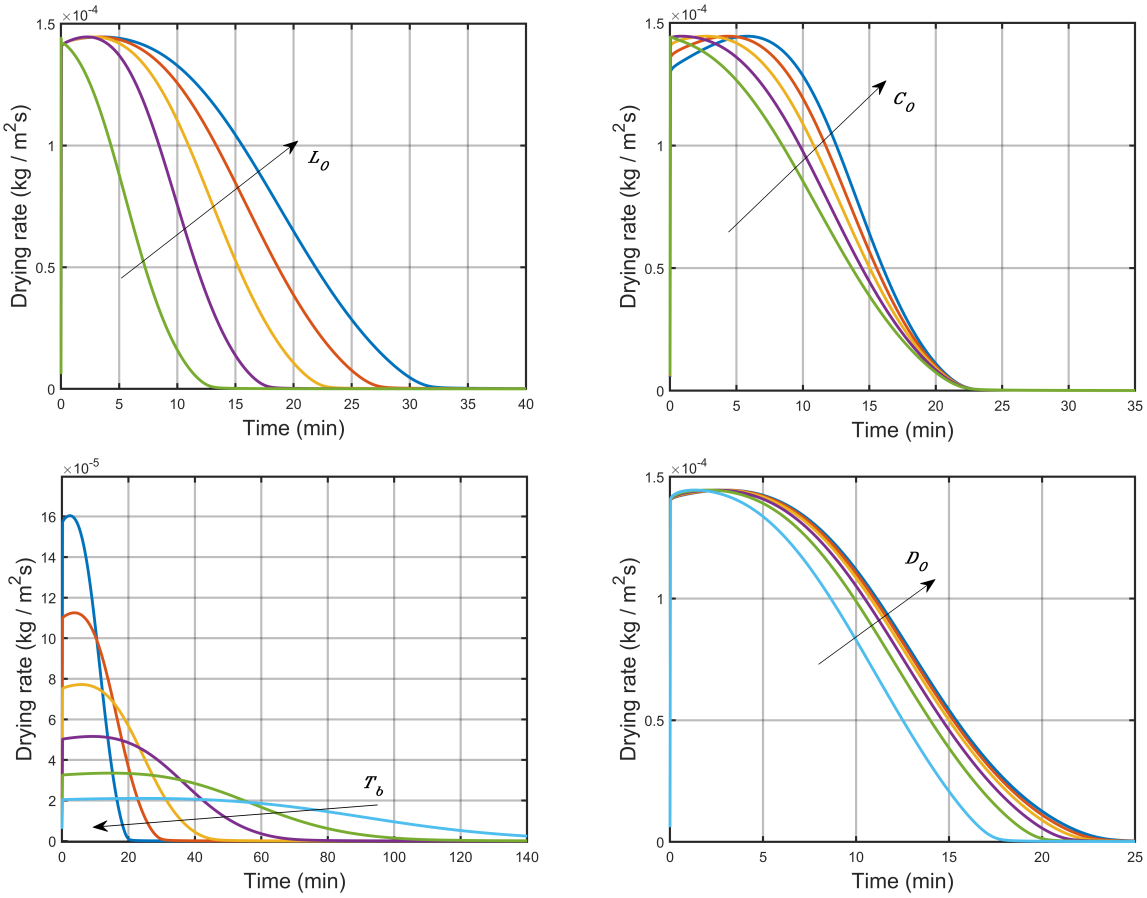

Figure 4.6: *The changes in drying rate caused by adjustments to initial parameters for the radiation drying process.* L_0 *is initial thickness,* C_0 *is initial solvent fraction,* T_b *is heat source temperature, and* D_0 *is initial diffusion coefficient. The arrow direction represent an increase in input value.*

Multi-stage heating was tested for the radiation drying model. The simulation used an initial heat source temperature of 80°C, increasing to 95°C after two minutes, and to 115°C when reaching five minutes. This resulted in a evaporation energy of 59.0 kJ/m^2 with a required drying time of 38.7 minutes. Figure 4.7 shows the resulting plot for the temperatures and drying rate as a function of time. Comparing the multistage drying process with single-stage drying at the respective temperature stages resulted the plot shown in Figure 4.8. The corresponding evaporation energies and time requirements are listed in Table 4.13.

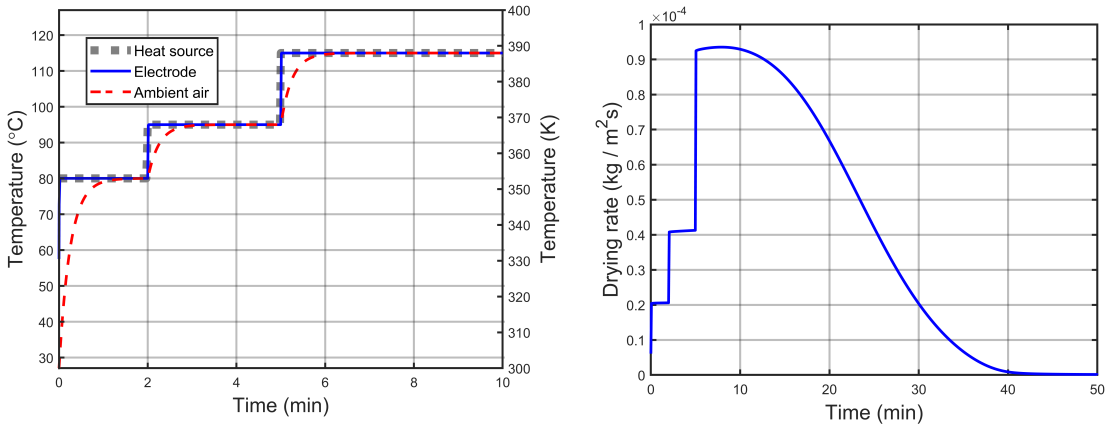

Figure 4.7: *Temperature and drying rate as a function of time in a multistage radiation drying process.*

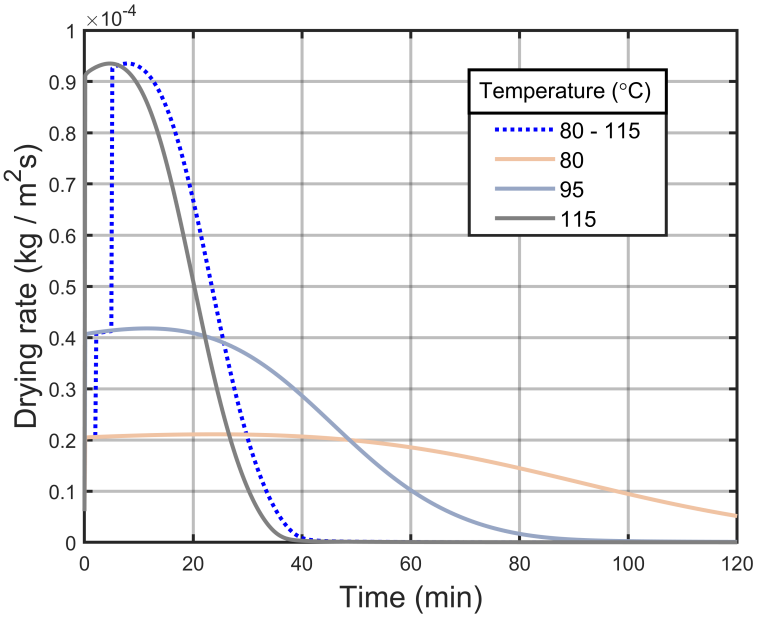

Figure 4.8: *Comparison of drying rates for radiation drying. The multi-stage drying utilizes air temperatures between 80°C and 115°C, which is represented by the dotted line. The remaining lines show single-stage drying at temperatures 80°C, 95°C and 115°C, represented by the cyan, orange and grey line, respectively.*

The drying rate of the multi-stage drying process, displayed in Figure 4.8, exhibit the same trend as its single-stage counterparts. As a result of the lowered initial heat source temperature, the multi-stage process is shifted to the right when compared to the single-stage processes of 95°C and 115°C. Furthermore, the single-stage drying processes of 80°C, 95°C and 115°C are shown to follow the same pattern as previously observed in Figure 4.5.

Table 4.13: *The evaporation energy and required drying time for the radiation drying simulations using multi-stage compared to single-stage.*

Temperature [°C]	**Evaporation energy** [kJ/m^2]	**Time required** [min]
80 - 115	59.0	38.7
80	65.5	149
95	62.8	80.2
115	58.7	35.5

The evaporation energy displayed in Table 4.13 shows a minor difference between the multi-stage drying process, and the single-stage drying process of 115°C. The biggest difference is observed in the drying time, which is shown to be 3.2 minutes slower for the multi-stage process. Meanwhile, the results from using a single-stage process with a lower temperature are shown to have a higher evaporation energy and slower drying time.

4.1.3 Comparison of convection and radiation drying

Comparing the two processes for convective drying and radiation drying, presented in section 4.1.1 and 4.1.2, using their respective initial parameters resulted in the plots shown in Figure 4.9. The plots show the comparisons for film thickness, temperatures, solvent fraction, and drying rate as a function of the time inside the dryer.

One of the most noticeable difference between the two models when looking at the plots is the solvent fraction. For the radiation drying process, the solvent fraction reaches zero at the end of the simulation. Meanwhile, for the convective drying process, the solvent fraction stagnates at a level above zero. This is also reflected in the film thickness, which shows that the radiation drying results in a thinner film than the convection. A difference in film temperature is also apparent when analyzing the plot. The film takes some time to increase its temperature during the convective drying. Meanwhile, for the radiation drying, the film temperature is heated seemingly instantly. Lastly, the drying rate of the two processes look relatively similar. The main difference being the lagging of the convective drying and the subsequent slope.

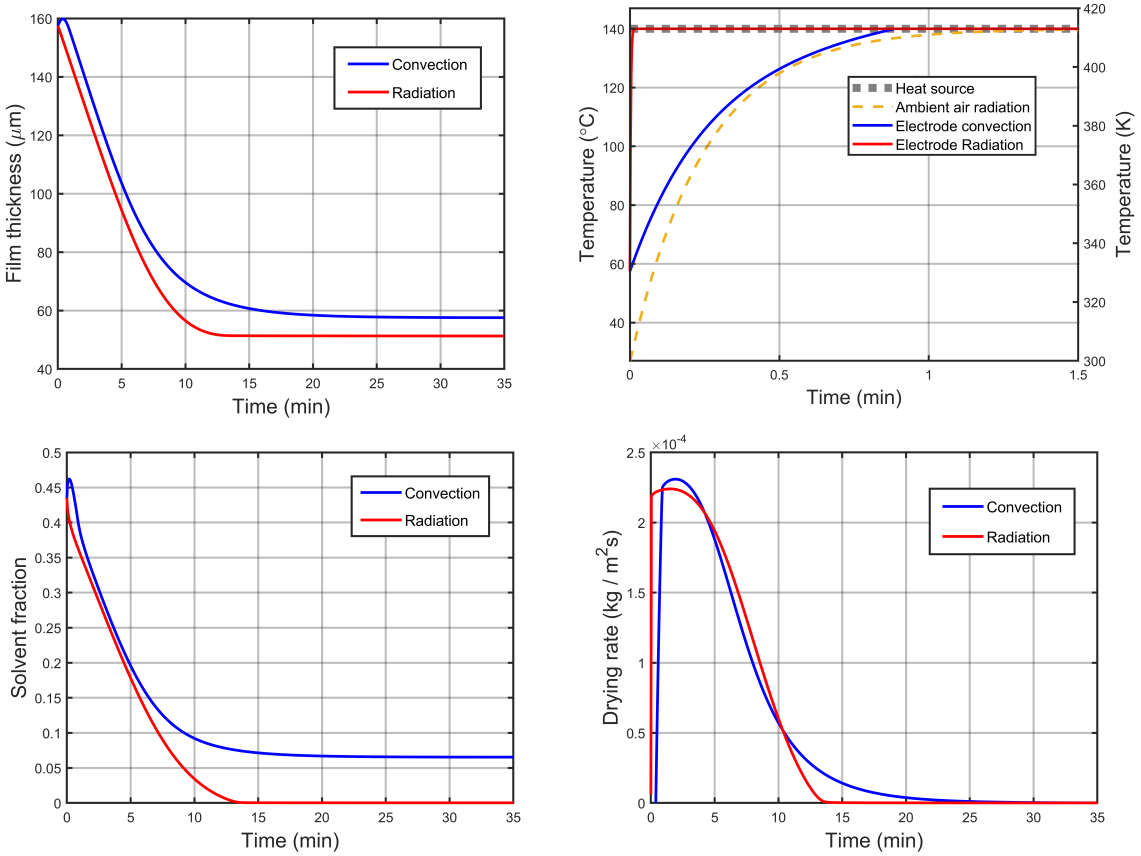

Figure 4.9: *Comparison between convection- and radiation drying using their respective initial values.*

4.1.4 Evaporation power for different electrode chemistries

The results from the evaporation energy are further converted to power to enable comparison to the rest of the loads in production. Table 4.14 shows the resulting conversion to required power for the simulated electrode of Section 4.1.3, based on the approach explained in Section 3.4.

Table 4.14: *The required cathode evaporation energy and power for the convective and radiation drying processes using a heat source temperature of 140°C, with their respective original design.*

	Drying time [s]	**Evap. energy [kJ/m²]**	**Production [m²/s]**	**Power [kW]**
Convection	1398	49.4	0.531	26.2
Radiation	804	52.8	0.923	48.7

Separate simulations for the electrode chemistries NMC111, NMC811 and NCA are also included. The parameters changed from the initial design of Section 4.1.1 and 4.1.2 are displayed in Table 3.5. Using these parameters in the simulations for convection and radiation resulted in the values shown in Table 4.15 for the cathode and Table 4.16 for the anode. Here, the conversion to required power is also included.

Table 4.15: *The required cathode evaporation energy and power for the convective and radiation drying processes using a heat source temperature of 140°C for the electrode chemistries of NMC111, NMC811 and NCA.*

	Cathode	**Drying time [s]**	**Evap. energy [kJ/m^2]**	**Production [m^2/s]**	**Power [kW]**
Convection	NMC111	1150	44.5	0.645	28.7
	NMC811	871	56.4	0.852	48.1
	NCA	1152	44.9	0.644	29.9
Radiation	NMC111	855	47.1	0.868	40.9
	NMC811	854	59.7	0.867	51.8
	NCA	871	47.8	0.852	40.7

Table 4.16: *The required anode evaporation energy and power for the convective and radiation drying processes using a heat source temperature of 140°C for the electrode chemistries of NMC111, NMC811 and NCA.*

	Anode	**Drying time [s]**	**Evap. energy [kJ/m^2]**	**Production [m^2/s]**	**Power [kW]**
Convection	NMC111	823	46.5	0.902	41.9
	NMC811	1087	32.4	0.683	22.1
	NCA	1087	32.6	0.683	22.3
Radiation	NMC111	580	45.5	1.28	58.2
	NMC811	450	28.2	1.65	46.5
	NCA	456	28.5	1.63	46.5

4.1.5 Regeneration and air heating model

Simulation in Aspen HYSYS was conducted in order to determine the heating and cooling loads required for the hot air in the cathode drying process. The approach for this is presented in Section 3.5, and is based on basic thermodynamic principles such as mass and energy balance.

Two scenarios were considered in this case. One process would be for convective drying with an added regenerative heating unit, while the other would run without any regenerative heating or any energy saving techniques. In this case, the regenerator size was set to 0 kW. The convective drying process was tested for heat source temperatures of 140°C and 8°C, with a mass flow of 9 kg/s. The resulting heating and cooling loads are displayed in Table 4.17.

Table 4.17: *Comparison of the impact regenerator size have on heating- and cooling loads of the cathode drying for different temperatures, using Aspen HYSYS as simulation software.*

Temperature [°C]	**Regenerator [kW]**	**Heating load [kW]**	**Cooling load [kW]**	**Cathode drying [kW]**
80	**0**	663	663	1326
	100	563	563	1126
	250	412	412	824
	500	163	163	326
140	**0**	1208	1208	2416
	100	1108	1108	2216
	250	958	958	1916
	500	707	707	1414

The values of Table 4.17 shows a significant decrease in total load for the system through the addition of a regenerative unit. The decrease in required power is linear for the heating and cooling load. Lowering the temperature of the stream also has a significant impact on the power. Regardless of the temperature and the regenerator size, the power requirements are significantly larger than the evaporation power presented in Section 4.1.4. Further experimentation is also presented with the use of differently sized regenerators. Note that these energy values are without any external connections to other streams in the manufacturing process. The effect of external connections is further presented in Section 4.4.

Also, an important note is that these calculations are only for the cathode dryer. An additional dryer for the anode is needed for the battery manufacturing process. For this, it is assumed that the anode drying process require the same mass flow of heated air as the cathode drying, being 9 kg/s. Furthermore, it is assumed that the anode utilizes water as solvent instead of NMP, and as such, does not require a filtration process. This removes the need for cooling. However, a regenerative unit can still be implemented for the anode air stream. The anode heating load would be equal to the cathode heating load of 707 kW for 140°C.

Thus, the concluding assumption is that the total load for the drying process is equal to the combined heating and cooling load for the cathode, in addition to the heating load for the anode. For 140°C and a regenerator size of 500 kW, this total load amounts to 2121 kW. The temperature of the air used in the drying process is assumed to be the same for both the anode and the cathode. Further, the values for the heat exchanger size based on regenerator duty were calculated and are displayed in Table 4.18. These calculations are based on the underlying theory in Section 2.6.1.1.

Table 4.18: *Shows the different regenerator specifications tested for and impact on the total system.*

Regenerator duty [kW]	**Regenerator size [m^2]**
100	75.2
250	188
500	376

4.1.6 Required load for radiation drying

Using the assumptions and approach of Section 3.6, the total capacity required for the radiation heaters is calculated to be 742 kW. Adding to this, the expelled air needs to be cooled in order to filtrate the NMP solvent. Similarly to the calculations of Section 4.1.5, this is done by assuming that the required cooling load is equal to that of the heating load. It is also assumed that no heat exchangers are used in the process.

Another important note is that this only applies to the drying of the cathode. In this case, the electrode is heated by radiation which in turn heats the ambient air of the drying chamber. Assuming conservation of energy, the load needed to cool the same air is equal to the heating load. The cooling duty is needed for extracting the NMP. However, this is not required for the anode, as it utilizes water as solvent instead of NMP. Therefore, the anode cooling load equals zero. The required heating and cooling load without regeneration then amounts to a total of 2226 kW. The load of each step is as shown in Table 4.19.

Table 4.19: *Radiation heating and cooling load for the anode and cathode drying.*

Electrode	**Heating load [kW]**	**Cooling load [kW]**
Cathode	742	742
Anode	742	0

4.2 Desiccant system

This section presents the results of the desiccant system simulated in Aspen Plus, using the approach described in Section 3.7. The input parameters for the desiccant system are presented in Table 3.7. The equations presented in Section 2.5.3 declare the basis for how the results were calculated by Aspen Plus.

Changes in ambient air temperature present a significant impact on the total load required for the system. Table 4.20 shows how the results vary based on a ambient air temperature between -10°C and 20°C, with the remaining parameters set to the values displayed in Table 3.7. From this, it is clear that a lower ambient air temperature results in a overall higher energy consumption.

Table 4.20: *Results from changes in ambient air temperature.*

Temperature ambient air [°C]	**-10**	**0**	**8**	**20**
Temperature of dry air outlet [°C]	-7.00	1.00	8.00	17.0
Temperature of desiccant outlet [°C]	-15.0	-6.00	2.00	13.0
Mass flow of dry air outlet [kg/h]	31 857	31 869	31 883	31 915
Desiccant cooler [kW]	74.32	74.32	74.32	74.32
Desiccant heater [kW]	179.8	163.3	149.9	129.6
Dry room heater [kW]	303.8	231.7	174.7	89.9
Total load [kW]	557.9	412.3	398.9	293.8

Similarly, changes in the two separate mass flows also exhibit a noteworthy impact on the results. Table 4.21 display the changes caused by varying the mass flow of the air at the absorber inlet. By increasing this flow rate, the temperature of the air at the outlet decreases, which in turn

causes an increase in dry room heater load. The required amount of dry air needed for the system is mainly dependent on the size of the dry room. As such, it is important to observe how the system responds when applying a wide range of inlet air mass flow.

Table 4.21: *Results from changing the mass flow of the air at the absorber inlet to between 9000 kg/h and 40 000 kg/h.*

Mass flow air inlet [kg/h]	**9000**	**18 000**	**32 000**	**40 000**
Temperature of dry air outlet [°C]	14.0	10.0	8.00	7.00
Temperature of desiccant outlet [°C]	4.00	3.00	2.00	1.50
Mass flow of dry air outlet [kg/h]	8 971	17 937	31 883	39 853
Desiccant cooler [kW]	74.32	74.32	74.32	74.32
Desiccant heater [kW]	137.8	143.0	149.9	166.3
Dry room heater [kW]	32.6	87.73	174.7	224.5
Total load [kW]	244.7	305.1	398.9	465.1

Table 4.22 shows the result of changes in the mass flow of the liquid desiccant. Points of interest include the dry room cooler and the dry room heater, which shows a substantial increase with an increased mass flow. The mass flow rate also impacts the resulting temperature of the outlets.

Table 4.22: *Results from changing the mass flow of the liquid desiccant at the absorber inlet to between 500 kg/h and 3000 kg/h.*

Mass flow desiccant inlet [kg/h]	**500**	**1000**	**2000**	**3000**
Temperature of dry air outlet [°C]	6.00	6.20	8.00	9
Temperature of desiccant outlet [°C]	0.00	1.00	2.00	3.00
Mass flow of dry air outlet [kg/h]	31 878	31 880	31 883	31 886
Desiccant cooler [kW]	18.58	37.16	74.32	111.5
Desiccant heater [kW]	48.64	82.5	149.9	217.0
Dry room heater [kW]	192.2	186.7	174.7	162.7
Total load [kW]	259.42	306.4	398.9	491.2

4.3 Heat pump implementation

The heat pump system was simulated based on the initial conditions and relations presented in Section 3.8 and the dry room airflow values from Section 4.2. Different refrigerants were also tested, which yielded very different pressure ranges for the condenser and evaporator side of the heat pump. The required compressor energy was also found for the desired operating conditions of the heat pump. It is possible to see that lower pressure ranges also have a higher required compressor power for the heat pump to be able to operate under ideal conditions. Note that these results are for a dry room heater load of 132.1 kW. The results will be different if this load is changed. The heat pump with this design requires a regenerator duty of 1090 kW or alternatively using a heat exchanger connected to the desiccant system to assist in cooling the stream enough to warrant the use of a heat pump. However, using a heat pump still requires a large regenerator, since the heating load for the desiccant system presented in Section 4.2 with a value of 150 kW. This would require a regenerator duty of 940 kW. The resulting temperature ranges of the streams connected to the heat pump are 20-6°C for the electrode drying stream and 8-23°C for the dry room airflow. The temperature difference is too small to use a regular heat exchanger and using a heat pump is therefore viable.

Table 4.23: *The pressure ranges and power required for different refrigerants in the heat pump design.*

Refrigerant	Pressure ranges in heat pump [bar]	Compressor power [kW]	COP factor
R-22a	4.37 - 12.67	9.30	14.1
R-134a	2.53 - 8.25	16.2	8.17
R-600	1.37 - 4.33	20.1	6.58

Table 4.23 displays the compressor power based on different refrigerants for the configuration presented earlier. The pressure ranges are also displayed. The heat pump in this proposed design covers the entire heating load for air entering the dry room as well as contributing to cooling the air stream for NMP extraction. The potential energy savings total 247.9 kW. Although, this is somewhat dependent on the refrigerant used. Note that the heat pump design is highly reliant on characteristics of the other systems.

4.4 Pinch analysis and MER-network designs

The pinch analysis was completed using the approach explained in Section 3.9. The principles of the pinch approach are described in Section 2.7. The composite curve displayed in Figure 4.10 shows that the pinch is towards the lower temperature ranges, at about 10°C. Both the hot side and cold side curves are almost parallel to one another before approaching pinch at 10°C. The streams in the network are mainly air streams, and seeing as the hot and cold side both have the same heat capacity and similar temperature ranges, the curves are mostly parallel. The composite curve displays the characteristics of the network of streams.

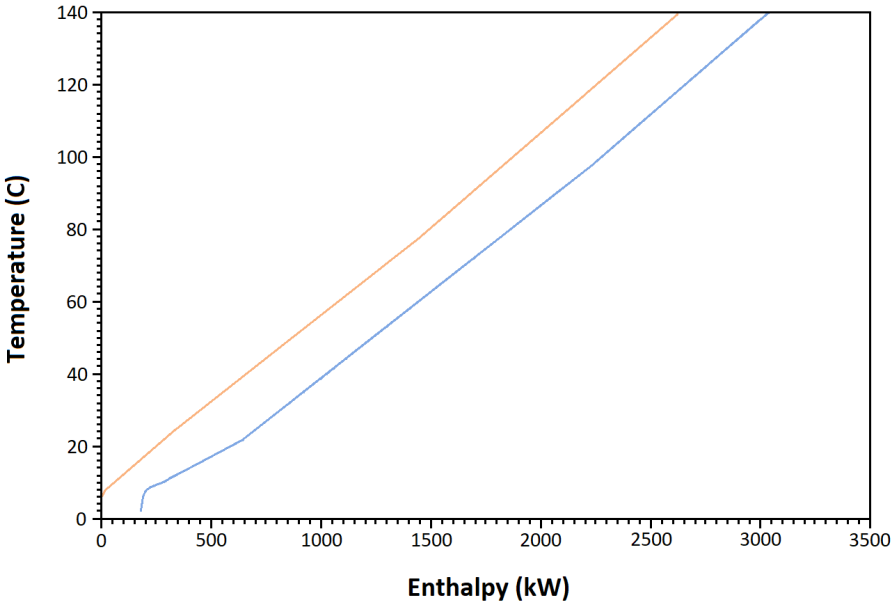

Figure 4.10: *The composite curves for the energy streams.*

The grand composite curve is displayed in Figure 4.11. From the figure, it is possible to see that the grand composite curve has an energy pocket to the bottom left of the in the 0-150 kW range. This is an area with excess energy, but the temperature ranges do not correspond sufficiently for a heat exchanger to be used. Therefore, a heat pump can be installed here. Note that the temperature ranges of the energy pocket corresponds well to the temperature ranges

of the heat pump results in section 4.3. Installing a heat pump in between the cathode airflow and the dry room airflow is therefore also possible for the MER-networks. The energy targets, the minimum heating and cooling load was calculated to be 403.7 kW and 177.6 kW for a total minimum load of 581.1 kW. The target total amount of heat exchangers used is eight. These are idealized values and are not necessarily achievable in reality. Note that this is without any heat-pump and is for both the dry room and electrode drying demand for both the anode and cathode streams. From figure 4.11 it is possible to see that the theoretically, implementing a heat pump in combination with a pinch optimized heat exchanger network has the potential to additionally save around 300 kW, this is a combination of both heating and cooling savings.

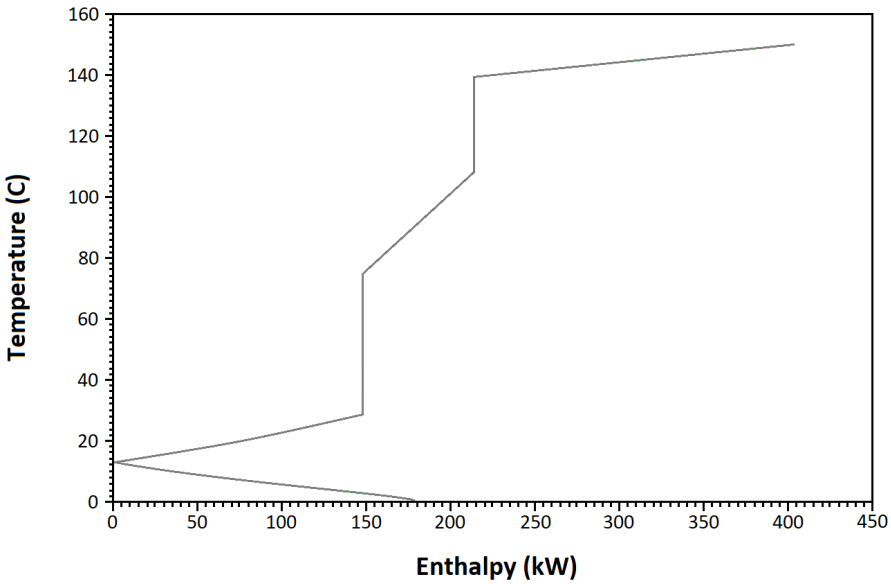

Figure 4.11: *The grand composite curve resulting from the input streams.*

A MER-network design connects the material streams of the process using a number of heat exchangers. The underlying theory of MER-networks is explained in Section 2.7.3, and is the principle used to generate these designs. The material streams are shown in Figure 3.7 without any interconnections. The MER-networks are based on these stream configurations. This illustration shows an overview of the different streams that are evaluated in the following MER-network designs.

One of the resulting designs based on the MER-network principle is displayed in Figure 4.12 and shows the heat exchanger connections between the individual streams. The cold streams are colored blue and the hot streams are colored orange, and are represented by the horizontal lines. The temperature ranges of the streams are also displayed to each side. The figure shows a series of heat exchanger connections, indicated by the vertical connection lines between the streams. The heat exchanger connections are separated into three different types. The regenerator units are grey and represent the interconnections between the different streams. The heating units are orange and connect to the hot utility stream. The cooling units are blue and connect to the cold utility stream. The temperature ranges of the utility streams are somewhat arbitrary as long as they satisfy the minimum temperature requirements set for the network. This can impact the size of the heater and cooler areas.

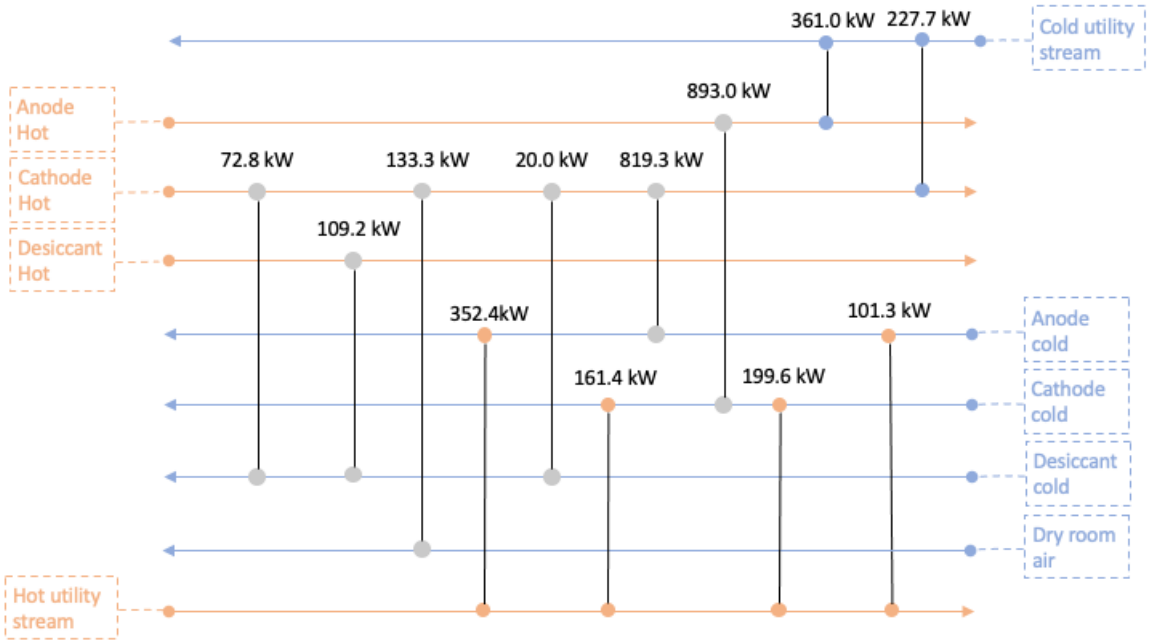

Figure 4.12: *MER network design one (MER-1).*

The MER network of design one is displayed in Figure 4.12. The resulting heat exchanger values from the the first design is displayed in Table 4.24. Here, the values for the duty of each exchanger is displayed. It is important to note that the utility streams chosen were arbitrary seeing as this does not impact the energy demands. However, this impacts the required area of the heat exchangers representing cooling and heating units. The cost is an estimate made by Aspen Energy Analyser. The first design case consists of 12 heat exchangers, where four of them are heaters and two are coolers. The total heating and cooling requirements for this heat exchanger network design are 814.7 kW and 588.7 kW, respectively. This brings the energy consumption to 1403.4 kW for the heating and cooling loads in the process. This is also without a heat pump to compensate for when the temperature ranges do not correspond sufficiently. The largest regenerator area in this design is 775 m^2 and the total heat exchanger size is 2058 m^2. The total estimated capital cost for this heat exchanger network is 764 653 USD.

Table 4.24: *Heat exchanger design values for the first design case (MER-1).*

Heat exchanger type	Duty [kW]	Cost [USD]	Area [m^2]	Number of shells	LMTD [°C]
Regenerator	819.3	251 913	775	7	13
Cooler	227.7	70 713	224	1	17
Regenerator	20.0	11 287	2	1	110
Regenerator	109.2	53 154	103	4	13
Regenerator	893.0	216 662	662	6	17
Regenerator	72.8	16 631	14	1	53
Heater	161.4	13 829	7	1	118
Regenerator	133.3	15 909	12	1	110
Heater	199.6	12 653	4	1	231
Heater	352.4	16 716	14	1	127
Cooler	361.0	73 683	238	1	24
Heater	101.3	11 504	2	1	238

An alternative MER-design, hereafter referred to as design case two, is displayed in Figure 4.13 and consists of a different setup utilizing four heaters and two coolers. The total amount of heat exchangers used is 13, one more than in the first design case. The energy consumption for this design is 864.7 kW for heating and 638.6 kW for cooling for a total energy load of 1503.3 kW. This is slightly higher than for the first design case.

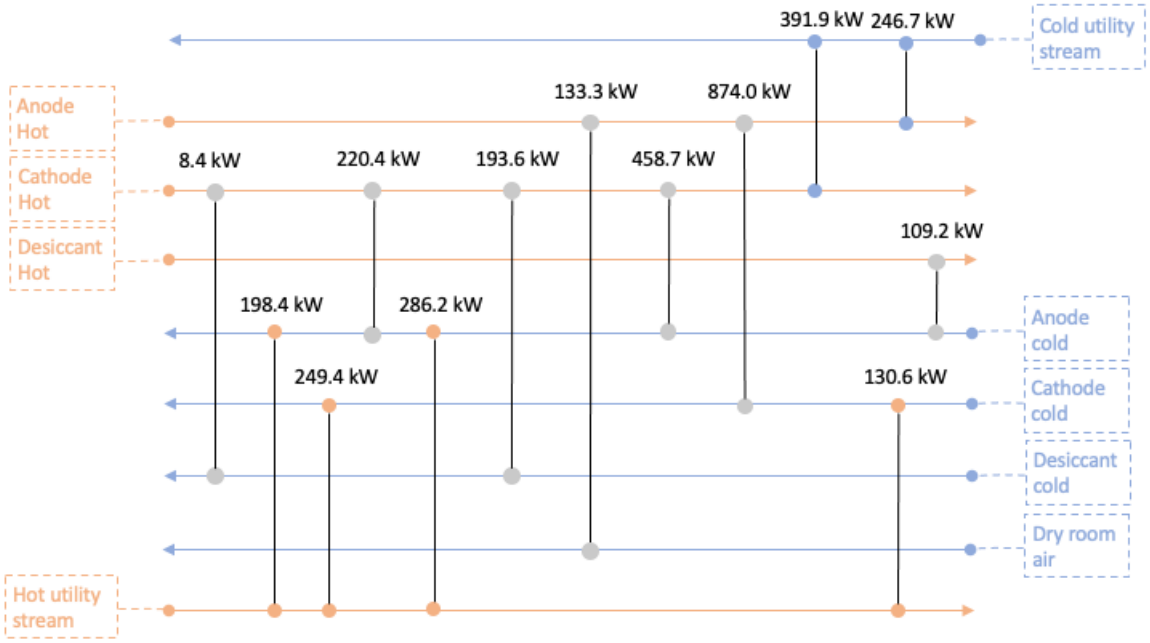

Figure 4.13: *MER-network design two (MER-2).*

The heat exchanger designs corresponding to the setup of design case two is displayed in Table 4.25. This design consists of 12 heat exchangers, four being heaters and three coolers. Note that the heat exchanger sizes are slightly different for this design, and that the largest heat exchanger is 900 m^2 compared to a largest size of 775 m^2 for the first design case. For this design case the total heat exchanger area is 1825 m^2. Additionally, the total cost for this design case amounts to 711 936 USD. The temperature differences also here satisfy the minimum requirement of 10°C.

Table 4.25: *Heat exchanger design values for the second design case (MER-2).*

Heat exchanger type	Duty [kW]	Cost [USD]	Area [m^2]	Number of shells	LMTD [°C]
Regenerator	220.4	57 528	139	2	20
Heater	286.2	14 558	9	1	168
Cooler	391.9	91 011	270	2	23
Heater	130.6	11 866	3	1	234
Regenerator	8.4	11 407	2	1	42
Regenerator	193.6	29 636	46	2	48
Regenerator	133.3	15 597	11	1	117
Regenerator	458.7	72 172	194	2	30
Regenerator	109.2	23 298	34	1	36
Cooler	246.7	65 066	198	1	20
Heater	198.4	14 449	9	1	120
Heater	249.4	15 263	11	1	122
Regenerator	874.0	290 086	900	8	12

The third design case shown in Figure 4.14. The resulting design consists of a total of four heaters and three coolers. This corresponds to a total heating and cooling load of 848.7 kW and 622.5 kW, respectively for a total load of 1471.2 kW. This is comparable to the total loads of the first and second design cases.

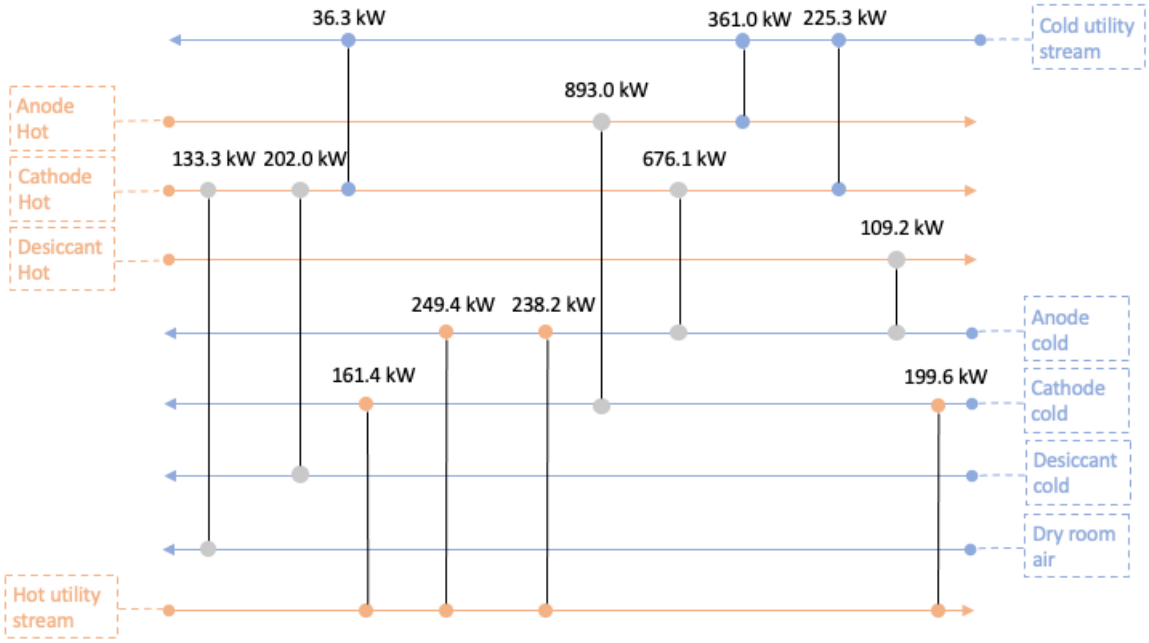

Figure 4.14: *MER-network design three (MER-3).*

The resulting heat exchanger design values for the third MER-network design case are displayed in Table 4.26. The largest heat exchanger in this network is 697 m^2 with a total area of 1928 m^2. Also here the temperature difference satisfies the 10°C minimum requirement. The total cost for this design is estimated to be 719 518 USD.

Table 4.26: *Heat exchanger design values for the third design case (MER-3).*

Heat exchanger type	**Duty [kW]**	**Cost [USD]**	**Area [m^2]**	**Number of shells**	**LMTD [°C]**
Regenerator	133.3	15 597	11	1	117
Cooler	36.3	12 981	5	1	98
Regenerator	893.0	216 662	662	6	17
Cooler	225.3	68 975	216	1	17
Heater	161.4	13 822	7	1	118
Regenerator	676.1	225 337	697	6	12
Regenerator	109.2	23 298	34	1	36
Heater	249.4	15 259	11	1	122
Regenerator	202.0	27 910	41	2	56
Heater	199.6	12 653	4	1	230
Heater	238.2	14 360	8	1	148
Cooler	361.0	72 664	233	1	25

All of the networks share some common characteristics, such as the two low temperature coolers at the top right in all the design layouts. Additionally, all of the designs have a remaining low temperature heating load to the bottom left. There is potential for connecting a heat exchanger between these two parts of the network. This can be done for all the networks and the energy consumption would then be even lower.

4.5 Total energy comparison

This section contains a summary of the energy requirements for the process scenarios mentioned in the previous sections, as well as a calculation for watt-hour energy per watt-hour battery for each configuration. Figure 4.15 shows the different layouts ranked from highest to lowest in regards to total power demand. Additionally, each process is split into colored sections, representing different process steps.

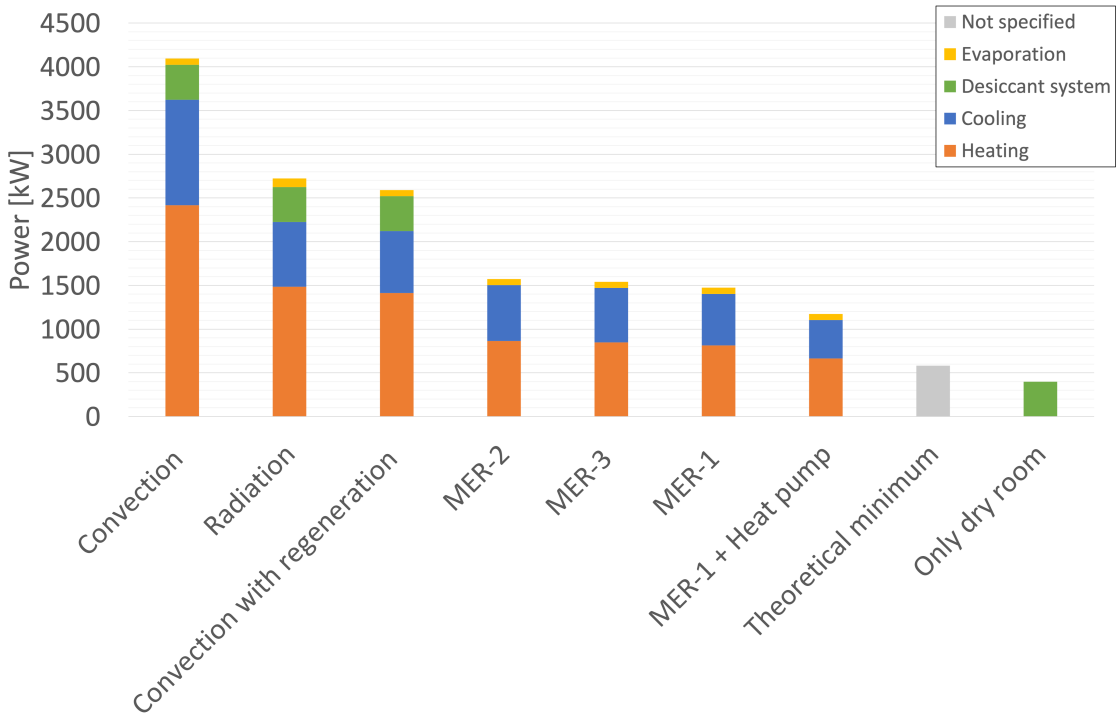

Figure 4.15: *Bar chart comparing the total power requirement for the different drying processes.*

Figure 4.15 shows that a convective drying process without regeneration require the most amount of energy. It is then followed by the radiation drying process without any heat exchange. With the addition of a regenerator, the energy demand for the convective drying process is decreased by approximately 2000 kW. The MER-network designs are close to identical in terms of required load, varying only by 100 kW between MER-1 and MER-2. By implementing a heat pump in the MER-1 design, the load is further decreased by 300 kW. This estimate is approximated from the grand composite curves.

Aspen Energy Analyzer also provides the theoretical minimum energy requirement for the convection drying MER-network. This minimum is estimated to 581 kW, which is also included in Figure 4.15. Lastly, the energy requirement for only the dry room is included. This is to show how much the energy requirement can be cut if the drying process is removed entirely.

Assuming an hourly cell production rate, it is possible to approximate a correlation between watt-hour energy input per watt-hour battery output. Table 4.27 shows an estimation for the cathode chemistries of NMC111, NMC811 and NCA. By further assuming that a yearly production include 24 hour operation over 300 workdays, the cell production rate per year can be derived. This is also presented in Table 4.27.

Table 4.27: *Estimated cell production rates for the cathodes NMC111, NMC811 and NCA.*

	Cathode	Cell production [kWh/hr]	Cell production [GWh/yr]
Convection	NMC111	85.12	0.613
	NMC811	78.48	0.565
	NCA	110.4	0.793
Radiation	NMC111	89.97	0.648
	NMC811	78.48	0.565
	NCA	116.7	0.841

Figure 4.16 shows the estimated energy as Wh/Wh-ratio using the technologies of Figure 4.15 and the cell production rates for the cathode chemistries presented in Table 4.27.

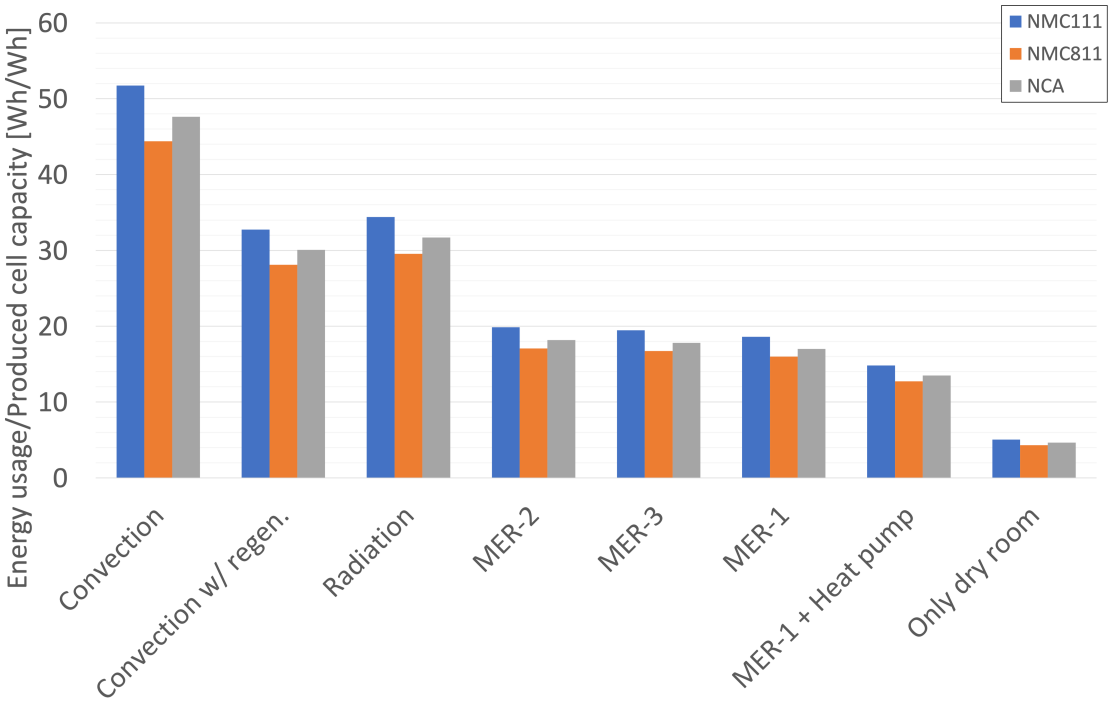

Figure 4.16: *Bar chart comparing the energy input with the battery capacity output in watt-hour per watt-hour for different processes and battery types.*

5 Discussion

This section contains a discussion of the results presented in Section 4. Conclusions related to the thesis are drawn based on the discussion presented in the following sections.

5.1 The drying process

This section discusses the results from the convective and radiation drying processes. The heating and cooling loads, as well as the evaporation energies, are considered.

5.1.1 Convective drying

Simulation of the convective drying was conducted using a combination of MATLAB and Aspen HYSYS. The prior was used to calculate the drying time, as well as the energy for evaporating the solvent from the slurry. The latter was used to determine the energy required for heating and cooling of the hot air stream. The simulations in MATLAB unraveled an overall trend for the film thickness, film temperature, solvent fraction and drying rate. This trend shows an introductory steep decline in film thickness and solvent fraction as a function of time, before leveling at a certain stage. This is in line with realistic expectations, as the removal of the solvent would decrease the overall mass of the film. The temperature of the film experience a relatively rapid increase from its initial temperature, to the temperature of the heat source, which in this case is the hot ambient air of the dryer. As a result, the determined drying rate of the electrode shows a peak rate around the point where film temperature equal the heat source temperature, which is a bit prior to one minute into the drying process when simulating for a temperature of 140°C. The drying rate then decreases as time progress, and ends at approximately zero. This indicates the end of the drying process.

The rate of which the film thickness, film temperature and solvent fraction changes is found to be highly dependent on the ambient hot air temperature, and the velocity said air is blowing at the electrode surface. An increase in air velocity or air temperature results in a significant decrease in the required drying time. In this model, the impact the drying rate has on the electrochemical performance of the electrode is not considered. However, it can be assumed to be an important factor in regards to cracking and overall integrity. A possible solution is to alternatively use a lower air temperature or velocity, or multistage drying which is further explained in Section 5.1.2. Additionally, by increasing the air temperature or flow rate, the subsequent loads required for the dryer also increase. The energy needed to vaporize the solvent from the electrode exhibit a modest change based on these parameters. However, a sizable change is observed in the drying time, ranging from 130 minutes at 80°C to 23.3 minutes at 140°C. Despite the increase in drying time, which would reduce the production rate, the lowered energy requirement would also affect the Wh/Wh ratio.

The evaporation energy necessary for the drying process is instead observed to be mostly dependent on the initial parameters of the electrode. Nonetheless, specifications such as the densities of the solvent and solid, the specific heat, and molecular weight of the solvent are determined by the electrode composition and solvent selection. As such, these values are usually predetermined based on the battery design in manufacturing. The same can be argued for the initial film thickness, and also potentially the solvent concentration needed for the electrode. However, these parameters are easier to modify and experiment with. Still, they are of high importance to the resulting energy requirement and drying time, as well as the quality of the

produced electrode. This is especially true for the initial film thickness, where an increase in thickness seems to result in an equal percentage increase in required evaporation energy and evaporation time. An increase in the solvent fraction also results in a noteworthy increase in evaporation energy. An interesting observation, as seen in Table 4.2, is that an increase in solvent fraction seems to result in a decrease in drying time according to the simulation. This can be justified by the partial pressure causing a shift in drying rate, pushing the peak rate to a later stage of the process. As a result, the total drying rate for the initial minutes of the process is increased by the increased solvent fraction. This may also hold merit in reality, as the driving force for evaporation becomes bigger. Simultaneously, the high air velocity quickly removes the evaporated solvent, inhibiting the air from reaching saturated state.

When analyzing changes in initial film temperature, there is almost no impact on the evaporation energy or drying time. This is most likely due to the electrode being heated to maximum temperature relatively quickly in the simulation. Usually within one minute, regardless of initial values selected. Due to the relatively long average drying time, the energy required to heat the film to the same temperature as the heat source becomes virtually neglectable in comparison.

Further observation shows that the solvent fraction of the film stagnates before reaching zero. In other words, there is some solvent not being evaporated during the convective drying process. This would imply a need for additional drying at a later manufacturing stage. In standardized manufacturing, vacuum drying is a usual practice for this purpose. In the simulations, however, this phenomenon is likely caused by the stagnation in driving force. As the pressure difference between the film interface and ambient air goes to zero, so does the drying rate. The result is thus a stagnation in solvent fraction and film thickness. In reality, the electrode would continue to dry even at room temperature. Nevertheless, the overall trend could arguably be accurate given the need for additional drying in large scale production.

Another parameter of interest in the simulation is the initial diffusion coefficient. Changes in this parameter causes an increase or decrease in divergence between the solvent fraction of the top and bottom of the film. A too low initial diffusion coefficient causes the bottom of the film to dry considerably slower than the top, resulting in an increased total drying time. Additionally, a change in final film thickness is observed with the change of this parameter. By increasing the initial diffusion coefficient, the resulting thickness of the film becomes thinner. As this parameter is mainly dependent on environmental conditions and structural circumstances, which are difficult to accurately describe in a model, it is determined that it can be changed selectively based on the remaining parameters. As such, it works as a tuning factor for the stability of the model. The results from the simulation therefore vary by some margin based on the value selected. Thus, the event of an inaccurate assumption of this parameter, the values presented by the simulation should regarded while considering the diffusion coefficient.

The relative humidity of the air is also highly conditional to the ambient conditions. However, it is an important parameter to the convective drying process, whose impact on the results equal that of air velocity and air temperature. Increasing the humidity results in a decrease in drying rate and thus an increase in drying time. This is coherent, as less solvent can be absorbed by air that is already moisturized. A case can therefore be made for the practicality of such a process in regions of high humidity. In extreme cases, this might require a desiccant system in order to filter the make-up air before used for drying.

5.1.2 Multi-stage convective drying

The difference between single-stage and multi-stage drying processes is noticeable when analyzing the drying rates for the individual processes. The impact of a gradually increasing air temperature shows merit in regard to drying rate, and thus energy conservation. This is apparent in the results presented in Figure 4.4. As previously observed, an individual single-stage drying process exhibit an preliminary high drying rate before declining as time progresses. However, for a multi-stage drying process, the peak drying rate becomes exceedingly higher and occurs at a later stage in the drying process. It is especially interesting to compare the multi-stage drying to the single-stage drying of temperature 115°C, which is also depicted in Figure 4.4. Even though their maximum air temperature is the same, the multi-stage drying surpasses the single-stage process by a factor of 1.54 in regards to peak drying rate. This could be undesirable, seeing as cracking is directly connected to the peak drying rate. Ideally, the multi-stage drying process should probably be structured differently. Simulation also unveil a minimal difference in drying time between these two processes. The multi-stage process needs 32.3 minutes, while the single-stage process, using a temperature of 115°C, has a drying time of 32.2 minutes. Meanwhile, the evaporation energy of the multi-stage process require 53.8 kJ/m^2, while the single-stage of 115°C require 52.1 kJ/m^2. However, these differences is arguably neglectable when compared to the savings of having a lower initial air temperature. It is debatable whether the difference in drying time becomes accumulative in industrial scale manufacturing. Still, in that case it is most likely also financially acceptable when compared to the amount of supplementary energy required for the additional heating of the hot air stream. However, the setup required for multi-stage convection heating may require multiple drying chambers for the different stages. Such a design would conceivably be more complicated compared to single-stage, and might harm the scalability of the factory setup.

Through testing with a start temperature of 80°C, it was determined that using an interval of two minutes for the first temperature increase of 15°C, and an additional three minutes for the following final temperature increase of 20°C, resulted in a drying time closest to that of a process using only the highest temperature. With these conditions, the drying is completed at approximately the same time, yet the multi-stage process requires less energy for air heating. Using any extended intervals causes the drying rate to shift accordingly, leading to a longer drying time. This could potentially reduce the probability of crack formations. Meanwhile, increasing the temperature to accommodate for this shift also defeats the purpose of multi-stage drying, which essentially is to save energy through the use of lower initial air temperatures. This may also be the case with a more gradual increase in temperature, as each temperature increase causes a noticeable spike in drying rate. However, the simulations are based on a limited temperature range and only two instances of temperature increase. As such, they could prove inaccurate at higher or lower temperature ranges, or through the use of additional steps. It is possible that additional temperature increasing steps, focused towards the later parts of drying, would be more beneficial in terms of the peak drying rate.

The difference in total energy between single-stage and multi-stage drying is not accurately presented by the results of the simulation, as the output is limited to evaporation energy and drying time. However, the difference becomes more noticeable when considering the volume of air that needs to be heated. The obvious advantage that the multi-stage process has in this comparison, is that a lower mass flow of air has to be heated to high temperatures at the start of the drying process. This results in an overall lower energy requirement for the system, especially

when considering that the main disadvantage of utilizing any convective dryer is the energy sink that is increasing the temperature of the air. This becomes evident when operating at higher air velocities, as the mass flow increases, which in turn increases the required loads. Such a comparison is highly advantageous for the multi-stage drying process. Additionally, if multiple drying chambers at different temperatures are used, these chambers can be heated by multiple streams with different temperatures, this would decrease the energy requirement for heating and cooling of the airflow for NMP removal. However, this may be difficult to accomplish in a realistic setting.

The advantages of the multi-stage process might be reduced when opening up for the possibility of implementing the energy of the heated air elsewhere. The principle of heat exchanging would also apply for the single-stage process, but with a higher average temperature compared to multi-stage. The high temperature air flow at the outlet of the dryer can administer energy to other parts of the production process through the use of heat exchangers. Such utilization can include, but is not limited to, regeneration between anode and cathode, the dry room and floor heating.

With the procured results from the simulation, and the arguments of various subjects, a case can be made for a multi-stage convective oven having clear advantages over a single-stage convective oven. The results show minor differences in drying time, and a neglectable increase in evaporation energy. Thus, when neglecting the possibility of crack formation, the energy savings from the lowered air temperature becomes dominant. There is also the possibility of tweaking the multi-stage drying model, which can result in different observations.

5.1.3 Convection airflow energy

In addition to the evaporation energy for convective drying, separate steps for air heating and NMP removal are required to determine the total load of the process. One of the most energy demanding stages in convective drying is found to be the heating and cooling of the cathode air flow. Aspen HYSYS calculated the heating load required for increasing an air stream of 9 kg/s from 6°C to 140°C to be 1208 kW. This hot air stream leaving the dryer then needs to be subsequently cooled in order to condense the NMP solvent. Without regeneration, the cooling required for the cathode airflow is also 1208 kW. To minimize the energy consumption of this step, a heat exchanger between the two streams is implemented. The simulation of this yielded the energy requirements for the residual heating and cooling load. From Table 4.17, the size of the heating and cooling load is observed to decrease proportionally to the change in regenerator size. These results are in line with the underlying theory, and are expected. However, the higher duty regenerators will be far larger, and as a result more costly. The duty of the regenerator scales linearly with regenerator size. Still, the cost of the regenerator does most likely not have a strictly linear relation to size.

The energy requirements are seen to be proportional to the mass flow rate. As such, reducing this parameter can reduce the overall energy consumption. However, doing so can also potentially negatively impact the cell production rate, seeing as the mass flow rate and production rate can be assumed to be correlated. The mass flow rate is therefore a fixed parameter for the simulation, and is assumed to be the same for NMC111, NMC811 and NCA. The mass flow rate and the required regenerator size can also be assumed to be proportional. An increased regenerator size can therefore become an issue in larger setups seeing as high duty air-to-air heat exchangers can be excessively large and expensive. According to simulations, the energy

savings by implementing a regenerator is directly correlated to its size. This linear correlation is displayed in Table 4.18. A possible alternative for reducing the required regenerator sizes could therefore be to have several drying chambers for the cathode and anode, enabling a reduction in mass flow rate without reducing the production output. Using additional connections to the other manufacturing processes is another alternative, which is further discussed in section 5.4. Energy requirements for fans or compressors required to maintain the mass flow rate of the forced convection are not accounted for. The energy impact of this assumption is somewhat arguable, since the energy requirements are assumed to be very small compared with the heating and cooling load and therefore not a significant contribution to the total energy requirement.

The temperature ranges for the convective heating process is another parameter that significantly impacts the energy consumption, for this study a temperature of 140°C was used. This value also impacts the drying rate however, so reducing the temperature of the air used for drying could reduce produced capacity. However, it is important to note that a very high temperature cannot be used, seeing as this would result in a rapid drying rate and cracking. The assumption made that the cathode airflow needs to be reduced to 6°C is based on the value used by Ahmed et al. This assumption could contribute to some inaccuracy. However, this is deemed a reasonable assumption and the required temperature for NMP condensation will conceivably be relatively similar in most setups. For the anode side, the stream is assumed to be cooled to 8°C, corresponding to the assumed ambient temperature. However, since the anode stream does not contain NMP, the stream does not necessarily require much cooling beyond the amount needed to achieve water condensation. Still, the amount of water that condenses is reliant on the temperature range. A setup where the anode stream is cooled to around 80°C is also a possibility. However, by viewing the anode drying as a closed loop, having a 80°C temperature range will result in a higher required mass flow rate. Further, since less water can be absorbed by the airflow in the evaporation process due to less water being condensed as a result of the high temperature. It is possible that a desiccant system could be used to remove humidity from the anode stream. However, this requires a further analysis of energy usage. Therefore, the air is assumed to be 8°C. The cooling energy required for the anode is neglected, seeing as it does not contain NMP. This should not significantly impact the results. Make-up air will be required regardless and there are a lot of other energy requirements such as heat losses. These parameters will impact the end result of required power in the opposite direction to the implications of the anode temperature range assumption.

The total installation cost for a system that allows for NMP recovery can be expensive, depending on the size of the factory and production scale. As shown in Figure 2.10, the removal system is quite complex, and consists of a lot of expensive units beyond the air heating and cooling, as previously mentioned. A solid desiccant, such as a Zeolite wheel, can be used to recover any residual NMP not collected by the condenser. There is also a need for a tank when storing the NMP. The energy requirements and initial costs of this system, as well as maintenance and operation, can prove to be expensive. However, these elements are not accounted for in this model. Note that this can have some implications on the total energy requirements, but ultimately the air flow heating and cooling loads are deemed more significant. The total energy for the convective drying process can therefore be assumed to be somewhat higher than simulated.

Another possibility for reducing the energy consumption can be lowering the amount of NMP used in the slurry. As shown in Figure 4.1, the initial solvent fraction is set to approximately 45%

of the total mass of the slurry. This is a relatively high amount, and a lot of solvent needs to be evaporated accordingly. This in turn requires a high air mass flow rate, that can potentially be reduced if a reduction of the NMP content in the slurry is possible. Therefore, if the amount of solvent in the slurry can be reduced, the amount of airflow heating and cooling required can also be reduced. This will also affect the drying time, possibly allowing for an increased production rate. However, the amount of NMP used in the slurry is generally a fixed parameter due to electrode integrity and structure. As of now, the possibility of reducing the content of NMP in the slurry by any significant amount might not be viable.

One of the major assumptions made to simplify the Aspen HYSYS model was that the airflow exiting the electrode drying was composed of only pure air, thus not containing any NMP solvent. This assumption was made for convenience, as it eliminates the necessity for complex simulations for NMP condensation and extraction. Instead, the condition for the hypothetical NMP removal is for the airflow to be cooled to 6°C. Any deviance resulting from this simplification would be due to the difference in heat capacity between air and NMP, as well as the additional energy corresponding to the latent heat of condensation for NMP. So in reality, the cooling power required for NMP solvent condensation would be slightly higher. This is seeing as NMP has a higher heat capacity than air and the heat capacity is directly proportional to the heat required for cooling. Arguably, the impact of this simplification is very low due to low gravimetric content of NMP in the airflow exiting the electrode drying process. The evaporation energy and condensation energy of the NMP was also not accounted for in the Aspen HYSYS model. However, the evaporation energy calculated by MATLAB proved low compared to the overall energy requirement for air heating and cooling.

The total power needed for the convection heating of cathode and anode, as well as the subsequent NMP cooling is calculated to be 3624 kW, which results in a 51.7 Wh/Wh. The same process using a regenerator with a duty of 500 kW, yields a required power of 2121 kW, which equals to 32.7 Wh/Wh. This difference underlines the benefit of implementing a regenerator in a convective drying process. However, the energy per produced capacity ratio may be somewhat higher when accounting for the assumptions listed for the model. Additionally, this does not account for stages of the production such as formation energy, additional vacuum drying and mixing. Accounting for this, these values are comparable to values from standard factory setups of around 30-60 Wh/Wh for efficient setups.

5.1.4 Radiation drying

The simulation of the radiation drying process is modeled purely in MATLAB. Granted the model does not yield results for the energy required for the heat source, it helps to give insightful understanding into how an electrode responds to an alternative drying method. This also made comparison between radiation and convection possible.

From the simulations presented by Figure 4.5, a pattern is observed for the parameters of film thickness, film temperature, solvent fraction and drying rate. The film thickness and solvent fraction show a seemingly linear decrease throughout the drying process, only dwindling slightly towards the end. The correlation between the two parameters are clear, seeing as extracting the solvent from the film decreases the remaining mass, which in turn is displayed by the shrinking thickness. The drying process occurs until the solvent fraction reaches approximately zero. Seeing as no solvent remains, there is also no need for additional drying in later stages of the manufacturing process. The drying rate follow a somewhat similar pattern, nearly reaching peak

value at the beginning of the drying process, before gradually decreasing as time progress. A notable observation is that the drying rate reaches zero at the same time as the solvent fraction. The electrode is explained to be directly heated through radiation in this process. As a result, film temperature increase drastically from initial value, reaching the same temperature as the heat source almost immediately in the simulations. The ambient air is subsequently warmed by convection from the electrode. This temperature is lagging by between one and two minutes compared to the electrode. These temperature changes is also shown in Figure 4.5.

Altering the initial parameters results in various changes in evaporation energy and drying time. Increasing or decreasing initial film thickness is shown to have a noticeable impact on the evaporation energy. However, the time required for drying seem to change at a constant pace with the change of this parameter. A doubling in initial thickness prompts an approximated doubling in evaporation energy, while drying time increases by around four minutes for each 40 μm increase. An increase in evaporation energy is logical, as the increased volume of the electrode will have a significant impact on the energy required to extract the increased amount of solvent. It is arguable whether this increase is realistically accurate. It could potentially be higher, as the simulation is based on a simplified model. This argument also applies for the drying time. However, the growth in drying time increases at a different pace, and not directly relative to initial thickness.

Seemingly, the initial solvent fraction only has a noticeable impact on evaporation energy. When using a solvent fraction of 32.4 vol%, the resulting drying time becomes 21.9 minutes, while for 54.6 vol%, it becomes 22.2 minutes. Similarly, the evaporation energy changes from 48.3 kJ/m^2 to 60.8 kJ/m^2, for the same values. An explanation for the small change in drying time could be the that the effects of the partial pressure are minimal in regards to drying rate. Analyzing Figure 4.6 shows that the drying rate is shifted to the right when increasing the initial solvent fraction. However, all the plots converge before the end of the drying process. Further, the initial diffusion coefficient is mainly used as a tuning parameter, as it changes based on environmental conditions and is thus difficult to describe though simulation. Still, it is worth mentioning its impact on the final results, as lower values can limit the drying time and final film thickness. Another observation of an environmental parameter is that relative humidity has a neglectable effect on the resulting evaporation energy and drying time during radiation drying. This could be caused by the low air velocity of the process. Due to a lowered air velocity, the air mass flow is also decreased. This could imply that the radiation drying process is not as reliant on the surrounding air conditions as other drying processes might be. As such, drying by radiation could be highly applicable even in regions of high humidity.

The main objective of the air velocity in radiation drying is to transport the vaporized solvent. This air velocity for the simulations are set to a constant 4 m/s. This is mainly due to an estimation of the fundamental workings of the process. By increasing the air velocity, the drying time decreases immensely. This increased drying rate may compromise the integrity of the electrode, causing cracks in its structure. As previously mentioned, the temperature of the electrode increases drastically in a radiation drying process. An increased air velocity may also function as a cooling measure in this regard. Therefore, increasing the air velocity could simply cause more stress on the electrode, which may lead to further cracking or other damages in the electrode structure.

Analyzing the changes caused by adjusting the heat source temperature confirms that it is the most important factor for the drying time in a radiation drying process. A drying time of 150

minutes is observed when when using a heat source of 80°C. Meanwhile, the drying time when using a temperature of 140°C becomes 13.4 minutes. The evaporation energy also decreases with the increased heat source temperature, being 65.2 kJ/m^2 for 80°C, and 52.8 kJ/m^2 for 140°C. Further observation of Figure 4.6 shows a larger spike in drying rate with higher heat source temperature. The drying time is thus naturally shortened as a result. Due to the seemingly instantaneous increase in film temperature, the initial film temperature is virtually neglectable, as it shows no impact on results for evaporation energy or drying time.

5.1.5 Multi-stage radiation drying

The step-by-step increase in temperature and its effects on the drying rate of the electrode is shown in Figure 4.7. Changes in heat source temperature is tested by multiple configurations. However, the same trend is observed regardless. The opted arrangement of Figure 4.7 is an increase by 15°C after two minutes and an additional 20°C at the five minute mark. Observing the gradual increase in temperature for the electrode seems to conclude in a mare delay of the drying rate, as it follows the same pattern as the drying rates for each individual temperature. The peak drying rate also has the same value as its single-stage counterpart. The difference in evaporation energy is also small when comparing multi-stage to single-stage with a temperature of 115°C. This evaporation energy is 59.0 kJ/m^2 for the multi-stage process, and 58.7 kJ/m^2 for the single-stage. Still, the multi-stage process shows some merit in regards to drying time. The single-stage process at a temperature of of 115°C has a drying time of 35.5 minutes, while the multi-stage process use 38.7 minutes. An argument can be made for whether the savings made from the lower initial heat source temperature outweigh the additional drying time. However, this difference in drying time may become accumulative when considering industrial scale manufacturing. Therefore, it may not be feasible when adjusting for the reduction in sales.

Due to the multi-stage drying process following the exact pattern of its single-stage counterpart, it becomes seemingly impossible for a multi-stage radiation drying process to result in a lower evaporation energy and drying time than a single-stage process using the same maximum temperature. However, the simulations are only considering a two step temperature increase. Section 5.5.2 explores the idea of using a specialized laser technology in order to achieve more stages. Although this does not result in a lower drying time or required energy for evaporation, it may show benefits in electrode structure and thus the efficiency and lifetime of the batteries produced.

Another hypothesis on the topic of electrode integrity is that a gradual increase in temperature might help prevent the formation of cracking and other damages caused by a rapid increase in drying rate. Thus, the multi-stage radiation drying process could improve the quality of the finalized battery, compared to a single-stage process. As the model does not account for porosity, no conclusion can be made. However, further research on the matter can be done through laboratory testing.

5.1.6 Radiation heating energy

The energy required for the heaters in the radiation drying process is found primarily from engineering estimations. As such, it is a somewhat gray area due to the lack of available and reliable sources for parameters such as heat flux for radiation heaters in electrode drying. The heat flux is instead found through the use of Equation 2.5, which gives a simple correlation between the required load and electrode production.

The resulting heating and cooling loads for the radiation drying process accumulates to 2226 kW. This is considering the drying of both the anode and cathode, with a heat source temperature of 140°C. The anode is assumed to be utilizing water as solvent, and as such does not require cooling. Using these values the energy per produced capacity ratio becomes 34.4 Wh/Wh, which is comparable to the 30-60 Wh/Wh range of standard factories. It is also difficult to estimate any form of heat exchange between the radiation drying and other manufacturing steps, such as the dry room. This is mainly due to the lack of reasonable assumptions regarding the surrounding air temperature and mass flow rate. As discussed earlier, the film is heated directly by radiation. The air is then subsequently heated by convection from the film. Such a convection process can be lengthy, as previously simulated, and when also considering the air velocity transporting the evaporated solvent, it becomes exceedingly complex to determine the air temperature at the dryer outlet. Therefore, the results from the radiation heating is only accounting for a process without heat exchange. Still, this provides good insight on the required amount of energy for an unoptimized process, and serves as a benchmark for the optimized convection drying process. Further optimization of radiation could therefore prove promising.

5.1.7 Comparison of convection and radiation drying

Comparing the simulation results of convection and radiation drying, using a heat source temperature of 140°C for both processes, unveils some key characteristics. Figure 4.9 shows a comparison of these processes from the simulations in MATLAB. The most noticeable part is the film temperature behaving differently. For the radiation drying, it takes upwards of one minute for the film to reach the same temperature using convective drying. This is coherent with the underlying theory, where heat transfer by convection is seen as a slow process. The difference in film temperature is further reflected in the plots for film thickness and solvent fraction, which shows an immediate incline when using radiation, whereas the graph for convection is shifted to the right due to the lagging film temperature. The drying rates also illustrate this by showing the convection drying quickly increasing compared to radiation, where it starts at a high value. After reaching peak value, the drying rate is also steeper for convection than for radiation. Additionally, the drying rate during convection ends with a gentle slope, whereas for radiation the drying rate ends more abruptly. This may suggest that radiation drying has a more stable evaporation process, and has no problem extracting all the solvent from the film.

This is also evident when observing the solvent fraction. Simulation of the convection drying shows that some solvent is unable to evaporate. In a realistic setting, this would not be the case, as the evaporation would still continue even at room temperature. A possible explanation for this is the stagnating driving force of the model, which was previously explained in Section 5.1.1. Assuming the model is accurate up to the point of stagnation, it would imply a need for additional drying when using convection as the primary drying method.

Another key difference between the two processes is the ambient air temperature. For the convection drying process, the air is preheated. For the radiation drying process, the electrode is heated directly, which in turn increases the temperature of the ambient air. From Figure 4.9, the heating of the air during radiation drying is shown to be approximately 1.2 minutes. This heating is from room temperature to the same temperature as the film, which in this case is from 27°C to 140°C.

The evaporation energy is shown in Table 4.14 to be relatively low compared to the energy needed for either air heating or radiation heating. Assuming a fixed production of 742 m^2 for

NMC111, the evaporation energy needed for convection and radiation is 26.2 kW and 48.7 kW, respectively. Meanwhile, the required energy for air flow heating and cooling for both the anode and cathode, considering a temperature of 140 **°C** and no heat regeneration, is 3624 kW for convection, and 2226 kW for radiation. The difference is thus eminently apparent. Additional calculations for the cathode chemistries of NMC811 and NCA result in contrasting values based on the drying method. This is displayed in Table 4.15. From analyzing the table, it is clear that NMC811 in convective drying is an outlier. The lowered drying time is most likely caused by the solvent fraction used during simulation. As previously discussed, an increased solvent fraction results in a lowered drying time.

The most noticeable sources of inaccuracy are caused by the simplification of the model. It is assumed that no capillary forces are present, and porosity is also not accounted for. Additionally, the diffusion coefficient is an estimate based on the environmental conditions of the drying oven ambience, as well as the properties of the active material used for the film. Heating of the foil is also not considered in the simulations. This further implies that the heat transfer from the film is also neglected.

5.1.8 Electrode integrity

The integrity of the electrode can be discussed when looking at the drying characteristics of the convection and radiation drying shown in figure 5.1.7. Binder migration and cracking are caused with aggressive drying with a short drying time. The drying rate for both the convection and radiation drying increases rapidly and reaches a peak drying rate before dropping. These characteristics seem to be somewhat similar between the two drying techniques. Both of them does not linger at a high drying rate for long, which reduces the amount of time for binder migration and cracking to occur. Multi-stage drying with convection experiences a spike in the drying rate that is more intense than multi-stage radiation drying and general single-stage drying. As such, it is arguable whether the electrode integrity and crack formation are affected with the use of multi-stage drying. Either the introductory lowered temperature is beneficial in preventing malformation in the electrode structure, or the subsequent peak in drying rate could be destructive and essentially cause cracking. As porosity and capillary effects are not accounted for in the simulation model, further study could be made on the subject. Nevertheless, from an energy saving point of view, the multi-stage drying process proves superior.

5.2 Dry room

The resulting load needed for the operation of the dry room is calculated to be 399 kW based on the initial values of Table 3.7. However, this result is heavily dependent on a number of factors, and is based on assumed ambient conditions. One such factor is the temperature of the ambient air. Table 4.20 shows that the power needed for the system is 557.9 kW when the ambient temperature is -10°C. Meanwhile, the power is decreased to 293.8 kW when the ambient temperature is 20°C. This observation seem to suggest that regions with high ambient temperature are more suitable than locations with colder climate. Additionally, the energy requirement can be said to be seasonally dependent. It is also likely that changes in humidity has an impact on the resulting load, further supporting the importance of geographic location.

Another observation involves the mass flow rates of air and liquid desiccant. The logical deduction of the values presented in Table 4.21 and 4.22 is that an increase in either of the mass flow rates will cause an increase in total load required for the system. However, the

increase in load does not scale linearly with the change of one mass flow. It is probable that a optimal ratio exists between these mass flow rates. Such an analysis is not conducted in this case study. Nevertheless, seeing as these flow rates are directly proportional to the size of the dry room, it is worth mentioning. The size of the dry room will also be correlated to the production rate if the dry room is the bottleneck of the combined system.

The ratio between the mass flow of air entering the dry room from the desiccant system, and the electrode drying airflow is highly significant for the resulting ratio between the energy consumption of the two stages. The amount of dry air needed to satisfy the ISO-8 requirements for dry rooms. This requirement is reliant on factors such as the amount of people in the room, as well as its size. The energy requirement for just the dry room can therefore vary highly based on factory design, since the required dry room energy is directly correlated to the airflow into the room. As previously mentioned, both the ambient temperature and relative humidity also play an important role in the total energy consumption of the dry room. Estimating an accurate total load for the dry room is therefore exceedingly difficult as it changes based on factory design and ambient conditions.

A possibility for minimizing the energy load of the dry room could be to reduce the size of the dry room or the amount of people needed for the production steps. The production stages inside the dry room could ideally be fully automated, thus reducing the required airflow, which in turn reduces the energy consumption required in order to to achieve the desired room conditions. Another energy saving alternative is using a heat exchanger between the inlet and outlet air streams of the dry room, using the expelled air to pre-heat the new fresh air. This method of balanced ventilation has the potential to reduce the heating load of the dry room heater. Alternatively, a heat pump system can be connected to ambient air in order to heat the air entering the dry room. However, such a heat pump would not be able to make use of both the heating and cooling effect already present in the system. Therefore, using a heat pump for interconnections between streams is generally better if possible. Still, for manufacturing setups that do not require drying, this might be a possibility. A heat exchanger can also be implemented inside the liquid desiccant system where the temperature ranges, connecting the heating and cooling stages to create interplay.

Since the optimal desiccant mass flow rate is highly susceptible to changes in the ambient air temperature and relative humidity, it can also be beneficial to alter the desiccant flow rate depending on these parameters. As previously indicated, a higher desiccant flow rate seems to generally result in a higher energy consumption for the desiccant heater and cooler. Therefore, it can be considered highly inefficient to maintain a higher flow rate than strictly necessary to absorb the water content in the air flow. In order to optimize this, a measurement device could input ambient air temperature and humidity into a regulator that in turn is connected to a pump controlling the mass flow rate of the desiccant system. However, this could be difficult to accomplish in cases where the desiccant heater and cooler has interconnections to the electrode drying streams, since the connected streams would be affected. Which in turn could possibly result in additional heating or cooling loads for other air flows in the combined system depending on the desiccant mass flow rate.

Other potential sources of error can be the equation of state used for the Aspen Plus model can be a cause of inaccuracy, however as stated previously, this is not a major source of error. Furthermore, it is assumed that there are no losses in the desiccant system, and thus the calculated values will be lower than in a realistic setting. Additionally, there is assumed to

be no loss of desiccant. In reality, some of the desiccant would evaporate together with the water, requiring new desiccant to be introduced, this further increases the energy requirement. The compressor power for increasing the pressure entering the absorber column is also not accounted for in the dry room energy calculation.

From Figure 4.15, the energy consumption per capacity of battery produced for only the dry room system is showed to be 5 Wh/Wh based on the initial values of Table 3.7. Although, this number contains a high degree of uncertainty as it is directly tied to the power consumption of the dry room. The dry room load can vary substantially based on the ambient conditions as discussed previously. Additionally, for processes that remove the need for electrode drying entirely, the formation energy and the energy required to operate machinery can also become a more significant factor in production. For production methods that do not require drying, this also does not account for formation and mixing energy. Thus, it is deemed reasonable to assume that a total energy requirement for such a process would be in the range of 10-20 Wh/Wh.

5.3 Heat pump design

The heat pump design yields results that are highly dependent on the regenerator size, in regards to the potential energy savings. The regenerator size also determines if it would be optimal to use a regular heat exchanger instead. This is because, with a small regenerator, the temperature difference of the streams would be sufficient to use a heat exchanger in place of the heat pump. The required energy load of the heat pump is also fixed based on the required heating of the airflow entering the dry room. The residual heat from the electrode drying process needs to be partially removed by the regenerator before the heat pump. In a sense, the feasibility of the heat pump is directly correlated to the feasibility of the regenerator design since it was found that a regenerator size of 1090 kW would be required to warrant the use of a heat pump. Arguably, it is also possible to introduce another cooling connection to the air exiting the electrode drying by connecting this airflow to the heater in the desiccant system. The feasibility of this alternative would be reliant on the heating required for the desiccant system and the piping layout challenges such a design necessitates. Since the heating requirement for the desiccant is 150 kW according to the dry room simulations, this would reduce the required regenerator size to 940 kW in order to implement the heat pump. However, this is a very large heat exchanger and an economic feasibility analysis would be necessary. Such a design is starting to bear a semblance to the MER-network designs later explained in section 5.4. Such a design would also have a similar power requirement to the MER-networks. The points presented here imply that using a heat exchanger is only beneficial if there already is sufficient energy regeneration. If not, using heat exchangers to achieve sufficient energy regeneration possible.

The results from Section 4.2 shows the required heating for the desiccant system can become quite significant depending on the inlet air mass flow rate, air temperature and humidity of the air. It would however also be possible to also connect a heat pump to the desiccant heater in order to make use of the excess heat from the electrode drying process and reduce the load of the NMP airstream cooling. The feasibility of this is however dependent on the temperature ranges. As mentioned previously, the heating and cooling load for the desiccant system can be supplemented by a regenerator within the desiccant system. The required energy for the desiccant heater would therefore be highly reliant on the duty of the desiccant regenerator. Assuming the entire cooling load of the desiccant system is satisfied by the regenerator, the remaining heating required is 74 kW. Depending on the size of the electrode drying regenerator,

this heating load could be satisfied by residual energy from the electrode drying airflow. This would therefore be a type of dual interplay system, where the electrode drying stream could satisfy the heating duty of both the dry room airflow and the desiccant heater. This method of connecting heat exchangers resembles a MER-network, and is a solution that would contribute to optimising the energy demand of the production process. If the temperatures ranges of both sides of the energy exchange correspond sufficiently, it would also be possible to use a regular heat exchanger in place of a heat pump system, also for the desiccant connection. This would arguably contribute to lowering the installation and maintenance cost compared to using a heat pump. It is also worth noting that a smaller regenerator in the electrode drying loop, makes the available energy for the other heating loads higher. Adjusting the regenerator size to match the duty requirements of the dry room and the desiccant heater is a viable option. However, lowering the regenerator size also makes the heating load of the electrode drying process higher. An economic analysis comparing a design with a smaller regenerator, but higher available heat to a system with a larger regenerator, would be highly relevant. It is also a possibility that the installation and maintenance cost of such a system would outweigh the benefits when compared to using a larger regenerator.

The heat pump refrigerants that were tested were chosen based on tables for thermodynamic properties and how well they correspond to the temperature ranges within the suggested heat pump design. Theoretically, this should yield the refrigerants best suited for the heat pump design in question. It is, however, easily possible to miss relevant refrigerant alternatives to the ones simulated here. For industrial application and realisation of design, this should be more rigorously tested. The input and conditions for the heat pump are presented in Section 3.8.2. These input conditions are based on the underlying theory, and their optimal operating conditions. Testing R-22a, R-134a and R-600 as refrigerants in Aspen HYSYS yielded results presented in Section 4.3. These results show an inverse correlation between the pressure ranges within the heat pump and the required compressor power. At first glance, these results seem arguably strange, seeing as power is directly proportional to the required power. This also makes choosing the optimal refrigerant somewhat difficult, seeing as low required compressor power is desirable, but high pressure ranges are undesirable. Since it is possible that higher pressures will cause strain on equipment, which may lead to higher maintenance frequency and costs. R-22a has the highest COP factor of 14.1, corresponding to a required compressor power of 9.3 kW. However, this compressor power is negligible compared to the energy requirements for the total system. Thus, the choice of refrigerant is not very significant. It is possible that, since the compressor power is relatively small compared to the total power, it would be more beneficial to chose the refrigerant with the lowest pressure range. The suitable refrigerant is therefore R-600, with a pressure range of 1.37-4.33 bar, which has a slightly higher compressor power of 20.1 kW.

In some heat pump designs, turbines have been used to extract the energy as a result of expansion. However, this may result in high maintenance costs due to the nature of the phase change that occurs during the expansion. The phase change could possibly cause cavitation, seeing as the refrigerant will be very close to the evaporation point concurrent with the pressure decrease that occurs during the expansion. The amount of energy that would be possible to extract would be reliant on the difference in available energy from the electrode drying process, as well as the required energy. However, with an efficient setup, and potentially connecting to both the desiccant heater and the dry room heater, it should be possible to achieve a balance between the available and required energy on both sides. Therefore a case can be made against the use of a turbine, since the amount of energy savings relative to the additional maintenance

costs could conceivably be insufficient to justify this solution. Additionally, the energy spot price would have to be considered in relation to the maintenance costs to evaluate a potential economic benefit. Ultimately, it is highly likely that using a regular expansion valve is the most viable solution.

Seeing as the heat pump system as well as the combined system was simulated using Aspen HYSYS, this introduces simplifications and potential minor inaccuracies in the results that needs to be addressed. First of all, the choice of fluid package and solver in Aspen can result in inconsistencies dependent on the temperature and pressure ranges regarded in the model. These inconsistencies can vary based on the type of fluid package used. Seeing as both the SRK and Peng-Robinson was tested for, and minimal changes were observed in the results, the choice of fluid package was thus deemed to not be a very minor source of error. Additionally, due to the temperature and pressure ranges for this model not being very high, the similarity of the results for different fluid packages is expected. This also supports the conclusion that the fluid package is a very minor source of error.

Other possible sources of error are the simplifications made by Aspen HYSYS. These are simplifications related to the loss in the expansion valve of the heat pump, as well as the heat loss in the heat exchangers representing the condenser and expander in the heat pump system. The expansion valve does not account for losses, and only holds the function of decreasing the pressure of the stream as it partially changes phase. This can be deducted from the observation that the energy of the dry room side of the heat pump is equal to the sum of the compressor power and the drying process heat exchanger. Aspen HYSYS estimates loss in the heat exchangers based on different models that can be selected. Seeing as the simple model for the heat exchangers was used, this might not account for all the losses and thus is a source of error for the combined system.

5.4 Pinch analysis and MER-network designs

The heat exchanger networks generated by Aspen Energy Analyzer show that there is much potential for performing a pinch analysis on the system. The three MER-networks chosen for the report satisfy criteria which may make them viable for different manufacturers. Still there are a number of designs not mentioned in this report which may be viable for a particular manufacturer with specific interests. The MER-network designs generally hold very similar characteristics and heat exchanger placements.

5.4.1 Composite curve and grand composite curve

Figure 4.10 describes the potential the combined system has for undergoing a pinch analysis, and determines the characteristics of the combined system. The pinch point is placed at a fairly low temperature of 10°C and enthalpy level. This means that there is barely room for heat to be exchanged below the pinch point. However, above the pinch point there is a possibility to implement a number of heat exchangers. The composite curves are relatively parallel, this is due to both the hot and cold streams mostly being composed of air. Towards the lower temperature ranges, the desiccant also becomes a part of the combined stream compositions, and is the reason for the change in slope towards the end.

The grand composite curve, shown in Figure 4.11, shows the potential for implementing a heat pump in the system. There is an energy pocket located across pinch. However, due to the

rules of pinch analysis there cannot be placed any heat exchangers at this point in the system. Instead, it is possible to utilize a heat pump, which allows for heat to be transferred from below to above pinch. Doing this would allow 150 kW of latent heat to be transferred from below pinch to above pinch. In practice, this would decrease the energy demand by a total of 300 kW, seeing as 150 kW of heat is removed from the heat source and 150 kW is added to the heat sink. When implementing a heat pump in the system, one can therefore assume a 300 kW reduction in power for the ideal system. However, this does not factor in the power required to operate the heat pump. This is further explained in section 5.4.3.

5.4.2 MER-network designs

Design 1 can be summarized as the design with the lowest total load, but the highest investment cost and heat exchanger area. This design could prove to be the most affordable of the designs, if the design is implemented in an area with high cost of energy. In such cases, the accumulated savings may exceed that of the investment costs. For achieving the most energy efficient design, further work on design 1 would show the most potential. Design 2 can be summarized as the design with the lowest investment cost and smallest heat exchanger area, but highest total load. For energy saving purposes, this design is the least efficient of the designs. However, the total load of the design is still significantly lower than that of the other conventional manufacturing processes discussed in this thesis.

It is important to note that the differences between the three MER-network designs are minor in comparison to the power difference to the conventional manufacturing processes. Design 2, which has the highest power requirement of 1503.3 kW, still has a power requirement that is 1017 kW lower than that of convection with a 500 kW regenerator, which has a power requirement of 2520 kW. This implies that a MER-network would probably be the best way to minimize energy usage, when using convection heating of air for drying. Steps can be taken to further improve conventional convection heating, for example by implementing a heat pump, using a larger regenerator or utilizing district heating. However, there is no reason why those same measures cannot be used to also further increase the viability of a MER-network.

The MER-network design approach will arguably always be the better option when compared to conventional convective setups. A comparison to radiation heating might prove difficult as it is still a developing technology. Additionally, implementing MER-networks would increase the complexity of a factory setup, and therefore potentially reduce the scalability. Maintenance costs might also increase depending on how the heat exchanger network is integrated.

Further improvement on the MER-designs could decrease the total load to a value that is closer to the theoretical minimum. However, this would include high investment costs. The main reason for the large relative difference between the minimum power of around 600 kW and the MER-designs of 1400-1500 kW is due to the software factoring in costs and heat exchanger feasibility. Regarding an ideal setup, yielding a total power of 600 kW may be impossible to realistically implement into an actual factory setup.

Another point of discussion in the model, is the need for cooling of the hot anode stream. The model does not recycle all the hot air being used for drying the anode. The need for excess cooling of this air before removal is thus redundant. Any additional cooling load would further decrease the MER-networks total load by between 247 to 361 kW, depending on the

design regarded. However, as mentioned previously, when assuming a closed loop for the anode airflow, the temperature of the airflow is directly correlated to the amount of water that can be condensed, and removed from the system. This can translate to less water vapor being absorbed by the air flow, and thus make an increase in mass flow necessary. This in turn would increase the heating and cooling power since this is directly proportional to the mass flow rate. In examining whether or not it is possible to remove the cooling load of the hot anode stream this is highly important. If the entire cooling load can be removed, this yields even more efficient networks.

5.4.3 Heat pump in MER-network

Heat pumps are generally best applied to networks where energy efficiency measures, such as heat exchangers, are already implemented. Integrating a heat pump in the MER-network is definitely viable as seen in the grand composite curve. However, since there are multiple streams with temperature ranges that correspond to the pinch temperatures, it is possible that more than one heat pump would be required to be able to harness all of the available energy. Installing multiple heat pumps at different locations within an already complex MER-network might negatively impact the scalability of the combined system. The assumption that implementing a heat pump for the MER-network case will save 300 kW is somewhat simplified, as this does not account for compressor power or losses in the heat exchangers. However, this estimate could still be somewhat accurate. The total power for the design case 1 would therefore be 1174 kW, which corresponds to an energy per produced capacity ratio of 14.8 Wh/Wh. Note that this is for the ideal network. For the actual design cases, a heat pump can potentially replace the low temperature cooling units to the top right of each of the MER-design figures in Section 4.4. These streams can then be connected to one or more streams with low temperature heating to the bottom right. These heat exchanger characteristics are similar for all the designs. However, the size of the heat exchangers vary somewhat for each design case. Designs that have a larger heating requirement for this bottom right heater, such as design case 3, can potentially benefit more from installing a heat exchanger here. For design case 3, the size of this heat exchanger could be 199.6 kW, making it possible to save approximately 400 kW when accounting for both sides of the heat pump. Although, this is not considering the required compressor energy. Heat exchangers can also be connected to the heaters with higher temperature ranges to the left of the diagram. However, here the temperature difference will be higher, and thus the efficiency of the heat pump would be lower. Further, external heat pump connections to the ambient environment could also be possible, especially since the pinch temperature is just 10°C. Since a heat exchanger is connected over pinch, this results in low temperature differences and thus an efficient heat pump.

5.5 Alternative options and technologies

This section discusses and evaluates the potential for use of alternative technologies.

5.5.1 Semi-solid battery electrodes

Semi-solid and all-solid state electrode technology presents an entirely different production process than that of a conventional electrode manufacturing process, such as convection or radiation. However, the technology is experimental, as well as mostly confidential, so a great deal of simplifications and estimations has to be made to be able to compare these technologies to conventional technologies. Based on the information presented in Sections 2.3.1 and 2.3.2,

it can be assumed that savings made through the use of semi-solid state technology can be approximated to the elimination of the drying process. As such, the dry room is the only process step being assessed. According to Jinasena et al., the energy usage in a convective drying process is 96% for the combined drying and dry room, leaving 3% to formation and 1% to other processes. Although, it could be argued that energy consumption in formation would increase due to the increased viscosity.

5.5.1.1 Energy comparison

The concept of a semi-solid battery electrode consists of removing the drying process altogether. In practice, the energy that is required for drying the slurry, whether utilizing convective or radiation heating, is simply removed from the energy calculation. This has the potential to reduce the required energy for production by a significant amount. Figure 2.3 shows that the drying process alone is responsible for approximately 48% of the total energy requirement. This implies that replacing the conventional manufacturing process has the potential to cut the total energy requirement by almost half. However, this is based on a series of assumptions, such as neglecting the possibility of increased required mixing energy due to the different viscous properties of the slurry. Still, the mixing process is assumed to account for a minor contribution, relative to the overall energy consumption, that increasing the energy requirement of this step has an arguably negligible impact on the total energy requirement.

The introduction of this new technology will undoubtedly require the installation of new processing steps, each with their own energy requirements. For semi-solid battery manufacturing, the available information is limited, so assumptions have to be made. The energy demand for potential pre-processing, and crushing of the suspension particles, is dependent on whether the process is completed on site or off-site. As such, it may be more relevant to account for this in a full life cycle analysis. If the suspension particles are crushed on-site, it would introduce a certain energy requirement of unknown caliber, given the possibility of additional equipment and machinery. This is all dependent on the scale of the manufacturing. Further, the mixing of the slurry can be assumed to be performed in a conventional manner, so the energy requirement can thus be assumed to be of equal proportions to that of the conventional method. However, the higher viscosity of the semi-solid slurry could result in higher mixing time and energy. The energy requirements for molding and insertion are highly speculative as not much is known about the process, but these values can arguably be assumed to be relatively low compared with other energy requirements. While high viscosity processing can be time consuming depending on the setup it does not likely impact the total energy perspective by any significant amount. Since the extrusion die contributes to determining the properties of the electrode, this may also eliminate the need for calendaring altogether. The other alternative for insertion is to utilize nozzles to discharge the slurry in an electrode canister. As with high viscosity processing, this can be assumed to not be especially energy consuming. However, the energy consumption could prove to be somewhat higher if concepts such as mechanical vibrations, centrifuging or sonifications are introduced as post processing methods to help achieve uniform distribution of suspension particles. This could also result in higher production time and thus a reduced amount of battery capacity produced. Seeing as production steps that are time consuming and difficult to scale can impact the production rate, this can also impact the watt-hour energy per watt-hour produced capacity ratio for the factory setup. The rest of the manufacturing process can arguably be assumed to be similar to the conventional process. Accounting for the dry room energy ratio of 5 Wh/Wh, and additional energy requirements

mentioned here, the energy demand for the semi-solid production is estimated to be around 10-20 Wh/Wh.

From what is known about the technology, the potential to reduce the required amount of energy compared to a conventional process is significant. This is assuming the energy required from the drying process can be neglected in the total energy calculation. With the removal of the need for solvent, the environmental benefit increases even more. Most solvents being used today are environmentally destructive, and need to be collected and reused. This is a costly process. Therefore, the removal of solvents from the production process is greatly beneficial. However, from an economic standpoint utilizing this technology is not necessarily beneficial due to the potential cost of a patent lease. If this is economically viable or not, is dependent on the added cost of local electricity that would be required to cover the heating and cooling loads. Thus, an economic analysis accounting for patent lease cost should be performed when determining choice of technology.

5.5.1.2 Scalability

Concerning the potential for scalability, the main issue is identifying the bottleneck of the production process. Despite the storage and aging process being very time consuming, this is not necessarily the bottleneck if storage space is sufficient relative to the rest of the production setup. The cost of installing additional equipment also has to be considered for each segment of the production when determining the scalability bottleneck. The time consumption of the extrusion process would be reliant on the viscosity of the slurry. However, for the quality of the cell it is beneficial to maintain a high viscosity and thus this makes the process more time consuming. Despite the extrusion process being relatively simple in nature, the addition of post processing techniques has the potential to make the process less scaleable due to how specific the technology required is. Both the use of sonifications and vibrations could prove to be difficult to integrate, and be potentially time consuming relative to the extrusion process itself, thus impairing the scalability potential of the technology.

5.5.1.3 Performance

Assessing the performance of a semi-solid electrode concept relative to the performance of a conventional electrode is also highly relevant. However, this is based mostly on assumptions. The performance of the semi-solid electrode will be highly reliant on the degree of uniformity for the distribution of the suspension particles. Uneven distribution could conceivably result in an uneven distribution of charge, which could yield problems related to battery lifetime and general performance. Therefore, the post processing methods are a critical step with regards to the resulting battery performance. The uniformity will also be highly reliant on the viscosity of the electrode semi-solid structure, seeing as a more viscous fluid can create larger capillary forces, thus positively impacting the interparticle dynamics, and further the uniformity of the distribution within the electrode.

5.5.2 Laser drying

The energy consumption of laser drying is also based on assumptions. The required evaporation energy of the electrode slurry would remain the same regardless of the drying techniques. Therefore, it is conceivable that any energy requirements beyond this is the result of losses from the laser ablation process. As a result, the energy requirements for laser drying is highly

reliant on the absorption characteristics of the slurry. Laser drying would be a similar solution to radiation, and thus also require far less heating and cooling for the air streams from the electrode drying process. The main benefit of laser heating over radiation is the possibility of alternating the laser frequency throughout the drying process, allowing for a very high degree of control over the temperature and drying rate of the electrode. This is possible since cracking of the electrodes while drying is tied to the drying rate, and not the temperature. For this reason it could be possible to reduce the laser frequency, and thus increase the power of the laser towards the end of the drying process. Laser heating would therefore ideally be completed in combination with a regulator system that utilises temperature readings from an infrared sensor as input. The regulator would then control the laser frequency for optimal drying rate while avoiding cracks or structural damage to the electrode. This high degree of control over the drying process could also potentially allow for optimisation of the electrode quality and performance of the resulting product.

The potential cost of implementing laser drying is difficult to predict without building a model for electrode laser drying. Additionally, the technology is not commonly used in current battery production, making the accessibility of the technology somewhat limited. The scalability and expansion potential for a factory setup using laser heating should in theory be achievable, assuming that the accessibility of lasers appropriate for battery production is sufficient. For drying applications, it is likely that a setup using several lasers with focal points distributed across the electrode interface would improve heat diffusion and therefore be optimal. This would also reduce the need for high power lasers, seeing as a combination of several individual lasers could be used instead, this could potentially increase the availability of sufficiently suitable lasers.

If laser based production has the potential to increases the overall electrode quality, due to the resulting characteristics of the cell as a result of laser drying, then the the process is highly viable compared to conventional drying techniques. Despite the potential, laser drying as an alternative still requires extensive research in order to fully determine the viability compared to conventional setups.

5.5.3 District heating

As an alternative to the energy saving measures proposed, it could be possible to make use of an already existing district heating infrastructure. However, the viability of this alternative is highly reliant on the temperature ranges of the district heating network and how well they correlate to the temperature ranges of streams in need of heating. Assuming a temperature of 60°C, the district heating network would not be able to provide sufficient heating for the desiccant heater, with temperature ranges up to 100°C. This would also be the case for the airflow heater for the electrode drying process. Therefore this would require additional heating. The main argument for the use of district heating is considering the economic aspects. Seeing as the installation cost of the heat pump and regenerators could be somewhat costly, however the infrastructure required for implementing district heating could also be costly. Despite this, in production solutions that bypass the requirement for a electrode drying stage, this could be highly relevant. This is due to the fact that there would be no excess energy from the electrode drying process that could be utilized. For the semi-solid production, the use of district heating could be highly relevant. District heating could also assist in floor heating for the dry room and general heating needs for a factory building. Arguably, it would be conceivable to implement

some of the energy saving measures presented previously as well as district heating. This would be reliant on the total residual energy demand and thus the size of the regenerators in the heat exchanger networks. In areas where district heating infrastructure is not present, it could be possible to utilise residual heat from other nearby industrial processes if available.

6 Conclusion

The evaporation energy from the simulations in MATLAB amounts to a small portion of the total energy requirement of the manufacturing process. Based on different cathode chemistries, the evaporation energy lies in the range of 26-40 kW for convection, and 40-51 kW for radiation. This is assuming a single-stage drying process at a temperature of 140°C. The simulations are deemed to be an accurate representation of the overall trend of the drying process. However, the film thickness and solvent fraction for the convection drying simulation displayed an unrealistic stagnation. Still, the trend depicts a need for additional drying. Despite this, the model is an accurate portrayal of the drying process.

The heating and cooling of the air is by far the most energy demanding part of the convective manufacturing process. Simulation in Aspen HYSYS of a process without any regeneration yields a combined load of 4094 kW, which is equal to 51.7 Wh/Wh ratio. With a regenerative unit, this value is decreased to 2591 kW, or 32.7 Wh/Wh, which is comparable to the industry standard of 30-60 Wh/Wh. The combined load for the radiation drying is estimated to be 2724 kW, which corresponds to 34.4 Wh/Wh. However, the radiation drying estimate has a higher degree of uncertainty.

The dry room and desiccant system yielded results that were highly reliant on parameters such as the ambient temperature, mass flow rates and relative humidity. Therefore the energy estimates made in this section have a high degree of uncertainty based on these parameters. The final resulting energy requirement of the dry room was 399 kW, which corresponds to an energy per produced cell capacity ratio of around 5 Wh/Wh. In order to minimize energy consumption, the mass flow rate of the desiccant should not be higher than necessary.

Installing heat pumps to enable interplay is definitely feasible. However, heat exchangers need to already be implemented into the system for this to be viable. If the temperature difference does not require a heat pump, installing a heat exchanger would be a better alternative. Nevertheless, heat pumps are a great way to further improve the energy efficiency, and has the potential to save around 200-400 kW depending on how the rest of the network is connected. Heat pumps have even greater potential when integrated together with MER-networks.

The MER-networks yielded energy values that were significantly lower than conventional designs by utilizing interconnections between the different sub-systems in the manufacturing process. The MER-networks can be complicated, and result in a less scalable design due to the complexity of the combined system. The theoretical minimum for combined heating and cooling was 581 kW. However, such a design would be infeasible. The suggested designs have a total power of 1400-1500 kW, corresponding to an energy per capacity ratio of 18-20 Wh/Wh depending on the cathode chemistry. In reality the energy consumption would be slightly higher due to simplifications made in the models. Still, utilizing the pinch approach is highly favorable when compared to the industry standard of 30-60 Wh/Wh.

Semi-solid electrode structures are also an option for decreasing the energy consumption. For manufacturing methods that are able to bypass the drying stage, the energy ratio is estimated to be 10-20 Wh/Wh, when factoring in the dry room, and additional energy demand. This technology holds potential, and viability is mostly tied to the resulting quality and performance of the produced electrode. Laser drying also holds potential, and altering the frequency throughout the drying process can give a high degree of control over the resulting electrode structure. Both of these technologies seem promising and should be further evaluated.

7 Future work

This section highlights suggestions for continued work related to this topic.

7.1 MER-networks

The MER network design design approach can also be applied to larger factory setups than presented in these designs. Upscaling would alter the mass flow rates, and change the energy requirements for production. Additionally, exploring how MER-networks would perform using only local heat exchanger connections compared to unrestricted designs could also be of interest. Further optimization of the MER-networks would consist of designing a heat pump specifically for the MER-designs. Simulating such a setup would give results for the required compressor power for different setups, and the energy consumption could then be compared to a conventional design.

7.2 Laser modeling

Building a functional laser model is required to determine the full viability of laser drying compared to the energy used in conventional setups. A full scale study investigating the availability of the technology, and potentially performing an economic comparison, specifically for battery production, is also intriguing. Designing a regulator system specifically for altering the laser frequency throughout the electrode drying process is also highly relevant. This can include an in depth comparison of the cell quality using an electron microscope to visualize the electrode structure. This could additionally include testing the coulombic efficiency of the produced electrode. Investigating the option for using multiple lower power lasers would also be interesting, since such a setup could have multiple focal points distributed across the electrode surface. Exploring different setups, and viewing the impact of this on the drying rate is also relevant.

7.3 Semi-solid electrodes

Semi-solid electrodes bypass the need for drying in the manufacturing process. The total load for the semi-solid technology consists of more than just the dry room, as modeled in this thesis. An in depth study could be performed. This study could include a complete model for the power needed in other stages of the production, such as the formation and mixing steps. Additionally, the power of several pumps and compressors present in the system could also be accounted for. This would give a more exact value of the power requirement for producing the semi-solid electrodes. Further, the quality of the produced semi-solid electrode can be compared to conventional production techniques. Further research on post processing techniques in order to achieve uniform distribution of suspension particles is also relevant. Optimization of the dry room could also contribute to this. Designing a regulator based on inputs from ambient conditions in order to control the mass flow rate of the desiccant could be of interest. Additional energy saving measures, such as the use of district heating and heat pumps, could also be implemented specifically for the dry room.

7.4 Economic aspects

A full scale economic analysis based on the initial investment cost, and the economic savings due to energy savings is also an interesting continuation of this study. The investment costs for

the energy saving solutions in this thesis can be expensive. Sizable heat exchangers are utilized in these designs, as well as an intricate solvent recovery system. An analysis that compares the total investment costs with the energy savings from implementation, would give a good understanding of the economic benefits gained from utilization. The computer programs being used in this thesis include an economical analysis tool, which can be used as a reference for comparison.

A further study into scalability of production beyond a certain economic threshold could also be conducted. A study of this type could explore when the cost of a set production volume expands beyond the price of production for this volume, which would yield an economic surplus. This study would need to take into consideration the budget for a battery manufacturing plant, and compare this to the trend of supply and demand, as well as price in the battery market.

7.5 Improving the current model

Regarding some of the smaller energy contributions such as mixing, formation energy and turbomachinery would result in an even more comprehensive model for the energy required in battery manufacturing. Additionally, implementing a more detailed description of the driving forces, and using variable heat- and mass transfer coefficients would result in a more accurate estimation of the drying time and evaporation energy. The model could also account for capillary forces, as well as porosity and heat transfer from the foil. This could more accurately predict cracking and binder migration.

References

[1] International Energy Agency. *Global EV Outlook 2020 - Entering the decade of electric drive?* Paris, France: Technical Report; International Energy Agency, 2020. DOI: doi:10.1787/d394399e-en.

[2] Asanthi Jinasena, Odne Stokke Burheim, and Anders Hammer Strømman. "A Flexible Model for Benchmarking the Energy Usage of Automotive Lithium-Ion Battery Cell Manufacturing". In: *Batteries* 7 (2021). ISSN: 2313-0105. DOI: 10.3390/batteries7010014.

[3] Inc. 24M Technologies. *Electrochemical cells having semi-solid electrodes and methods of manufacturing the same.* US Patent #10,886,521. 2020.

[4] Keith Oldham, Jan Myland, and Alan Bond. *Electrochemical Science and Technology: Fundamentals and Applications.* Hoboken: John Wiley & Sons, 2011. ISBN: 0-470-71085-3.

[5] Reiner Korthauer. *Lithium-Ion Batteries: Basics and Applications.* 1st ed. 2018. Springer Berlin Heidelberg, 2018. ISBN: 3-662-53071-6.

[6] MengChu Zhou, Han-Xiong Li, and Margot Weijnen, eds. *Advances in Battery Manufacturing, Service, and Management Systems.* Piscataway, N.J: Wiley, 2016. ISBN: 978-1-119-05649-2.

[7] Heiner Hans Heimes. *Lithium-ion Battery Cell Production Process.* 2021. URL: https://www.pem.rwth-aachen.de/cms/PEM/Der-Lehrstuhl/~hwpp/Jahresbericht-2014/lidx/1/ (visited on 05/12/2021).

[8] Paul A. Nelson, Shabbir Ahmed, Kevin G. Gallagher, and Dennis W. Dees. "Modeling the Performance and Cost of Lithium-Ion Batteries for Electric-Drive Vehicles, Second Edition". In: (Dec. 2012). DOI: 10.2172/1503280.

[9] Jana Kumberg, Marcus Müller, Ralf Diehm, Sandro Spiegel, Christian Wachsmann, Werner Bauer, Philip Scharfer, and Wilhelm Schabel. "Drying of Lithium-Ion Battery Anodes for Use in High-Energy Cells: Influence of Electrode Thickness on Drying Time, Adhesion, and Crack Formation". In: *Energy Technology* 7.11 (2019), p. 1900722. ISSN: 2194-4296. DOI: https://doi.org/10.1002/ente.201900722.

[10] Kelsey Rollag, Daniel Juarez-Robles, Zhijia Du, David L. Wood, and Partha P. Mukherjee. "Drying Temperature and Capillarity-Driven Crack Formation in Aqueous Processing of Li-Ion Battery Electrodes". In: *ACS Applied Energy Materials* 2.6 (June 24, 2019), pp. 4464–4476. DOI: 10.1021/acsaem.9b00704.

[11] F. Font, B. Protas, G. Richardson, and J.M. Foster. "Binder migration during drying of lithium-ion battery electrodes: Modelling and comparison to experiment". In: *Journal of Power Sources* 393 (2018), pp. 177–185. ISSN: 0378-7753. DOI: https://doi.org/10.1016/j.jpowsour.2018.04.097.

[12] Emil Oppegård, Asanthi Jinasena, Anders Hammer Strømman, Jon Are Suul, and Odne Stokke Burheim. "Study of an Industrial Electrode Dryer of a Lithium-Ion Battery Manufacturing Plant: Dynamic Modelling". In: *Proceedings of the 61st Conference on Modelling and Simulation (SIMS 61)* (2020).

[13] J. Robinson, John Ruppert, Hongxu Dong, and Gary Koenig. "Sintered electrode full cells for high energy density lithium-ion batteries". In: *Journal of Applied Electrochemistry* 48 (Aug. 2018). DOI: 10.1007/s10800-018-1242-y.

[14] Mihai Duduta, Bryan Ho, Vanessa Wood, Pimpa Limthongkul, Victor Brunini, W. Carter, and Yet-Ming Chiang. "Semi-Solid Lithium Rechargeable Flow Battery". In: *Advanced Energy Materials* 1 (July 2011), pp. 511 –516. DOI: 10.1002/aenm.201100152.

[15] David L. Wood, Jianlin Li, and Claus Daniel. "Prospects for reducing the processing cost of lithium ion batteries". In: *Journal of Power Sources* 275 (2015), pp. 234–242. ISSN: 0378-7753. DOI: https://doi.org/10.1016/j.jpowsour.2014.11.019.

[16] Inc. 24M Technologies. *Asymmetric battery having a semi-solid cathode and high energy density anode*. US Patent #10,522,870. 2019.

[17] Nina Verdier, Gabrielle Foran, David Lepage, Arnaud Prébé, David Aymé-Perrot, and Mickaël Dollé. "Challenges in Solvent-Free Methods for Manufacturing Electrodes and Electrolytes for Lithium-Based Batteries". In: *Polymers* 13 (Jan. 2021), p. 323. DOI: 10.3390/polym13030323.

[18] P. Kurzweil and J. Garche. "2 - Overview of batteries for future automobiles". In: *Lead-Acid Batteries for Future Automobiles*. Ed. by Jürgen Garche, Eckhard Karden, Patrick T. Moseley, and David A.J. Rand. Amsterdam: Elsevier, 2017, pp. 27–96. ISBN: 978-0-444-63700-0. DOI: https://doi.org/10.1016/B978-0-444-63700-0.00002-7.

[19] Wilhelm Pfleging. "A Review of Laser Electrode Processing for Development and Manufacturing of Lithium-ion Batteries". In: *Nanophotonics* 7.3 (2018), pp. 549–573. DOI: doi:10.1515/nanoph-2017-0044.

[20] Qisheng Peng, Asta Juzeniene, Jiyao Chen, Lars Svaasand, Trond Warloe, Karl-Erik Giercksky, and Johan Moan. "Lasers in medicine". In: *Reports on Progress in Physics* 71 (Apr. 2008), p. 056701. DOI: 10.1088/0034-4885/71/5/056701.

[21] Christian Vedder, Dominik Hawelka, Mareike Wolter, Diana Leiva, Jochen Stollenwerk, and Konrad Wissenbach. "Laser-based drying of battery electrode layers". In: *International Congress on Applications of Lasers & Electro-Optics* 2016.1 (2016), N501. DOI: 10.2351/1.5118636.

[22] William C. Whitman, William M. Johnson, John A. Tomczyk, and Eugene Silberstein. *Refrigeration & Air Conditioning Technology*. 7th ed. Delmar, Cengage Learning, 2013. ISBN: 978-1-111-64447-5.

[23] Michael J. Moran, ed. *Fundamentals of Engineering Thermodynamics*. 8th ed. Hoboken, N.J: Wiley, 2014. ISBN: 978-1-118-41293-0.

[24] Naresh Susarla, Shabbir Ahmed, and Dennis W. Dees. "Modeling and analysis of solvent removal during Li-ion battery electrode drying". In: *Journal of Power Sources* (2018). ISSN: 0378-7753. DOI: https://doi.org/10.1016/j.jpowsour.2018.01.007.

[25] Ali Mesbah, Ashlee Ford Versypt, Xiaoxiang Zhu, and Richard Braatz. "Nonlinear Model-Based Control of Thin-Film Drying for Continuous Pharmaceutical Manufacturing". In: *Industrial & Engineering Chemistry Research* (2013). DOI: 10.1021/ie402837c.

[26] Alejandro Datas, ed. *Ultra-High Temperature Thermal Energy Storage, Transfer and Conversion*. Elsevier, 2020. ISBN: 978-0-12-819955-8. DOI: https://doi.org/10.1016/C2019-0-00964-8.

[27] Dale A. Anderson, John C. Tannehill, and Richard H. Pletcher. *Computational Fluid Mechanics and Heat Transfer*. Elsevier, 2020. ISBN: 0070503281.

[28] Shabbir Ahmed, Paul A. Nelson, and Dennis W. Dees. "Study of a dry room in a battery manufacturing plant using a process model". In: *Journal of Power Sources* 326 (2016). ISSN: 0378-7753. DOI: https://doi.org/10.1016/j.jpowsour.2016.06.107.

[29] *ISO - Standards*. ISO. URL: https://www.iso.org/standards.html (visited on 03/04/2021).

[30] ISO 14644-1:2015. *Cleanrooms and Associated Controlled Environmentss—Part 1: Classification of Air Cleanliness by Particle Concentration*. Geneva, Switzerland, 2015.

[31] Mohammad G. Rasul, Abdul K. Azad, and Subhash Sharam. *Clean energy for sustainable development : comparisons and contrasts of new approaches*. Queensland, Australia: Elsevier, 2017. ISBN: 978-0-12-805423-9.

[32] I Sarbu and C. Sebarchievici. *Solar Heating and Cooling Systems; Fundamentals, Experiments and Applications*. Elsevier, 2017. ISBN: 978-0-12-811662-3.

[33] S. Bouzenada, L. Frainkin, and A. Léonard. "Experimental investigation on vapor pressure of desiccant for air conditioning application". In: *Procedia Computer Science* 109 (2017). 8th International Conference on Ambient Systems, Networks and Technologies, ANT-2017 and the 7th International Conference on Sustainable Energy Information Technology, SEIT 2017, 16-19 May 2017, Madeira, Portugal, pp. 817–824. ISSN: 1877-0509. DOI: https://doi.org/10.1016/j.procs.2017.05.338. URL: https://www.sciencedirect.com/science/article/pii/S1877050917310062.

[34] Xinli Wang, Wenjian Cai, Jiangang Lu, Youxian Sun, and Xudong Ding. "A hybrid dehumidifier model for real-time performance monitoring, control and optimization in liquid desiccant dehumidification system". In: *Applied Energy* 111 (2013), pp. 449–455. ISSN: 0306-2619. DOI: https://doi.org/10.1016/j.apenergy.2013.05.026.

[35] Shabbir Ahmed, Paul A. Nelson, Kevin G. Gallagher, and Dennis W. Dees. "Energy impact of cathode drying and solvent recovery during lithium-ion battery manufacturing". In: *Journal of Power Sources* 322 (2016). ISSN: 0378-7753. DOI: https://doi.org/10.1016/j.jpowsour.2016.04.102.

[36] J. M. Coulson, J. F. Richardson, J. R. Backhurst, and J.H. Harker, eds. *Chemical Engineering*. Oxford: Elsevier, 1999. ISBN: 978-0-7506-4444-0.

[37] Suraya Hanim Abu Bakar, Mohd. Kamaruddin Abd Hamid, Sharifah Rafidah Wan Alwi, and Zainuddin Abdul Manan. "Selection of minimum temperature difference (Tmin) for heat exchanger network synthesis based on trade-off plot". eng. In: *Applied energy* 162 (2016), pp. 1259–1271. ISSN: 0306-2619.

[38] *N-Methyl-2-PyrrolidoneNMP Price Market Analysis - Echemi*. URL: https://www.echemi.com/productsInformation/pd20150901242-n-methyl-pyrrolidone.html (visited on 04/15/2021).

[39] Ian C. Kemp. *Pinch analysis and process integration*. Elsevier, 2007. ISBN: 978-0-75068-260-2.

[40] D Olsen, Y Abdelouadoud, P Liem, S Hoffmann, and B Wellig. "Integration of Heat Pumps in Industrial Processes with Pinch Analysis". In: (2017), p. 11. URL: https://hpc2017.org/.

Energy Optimization for Lithium-ion Electrode Manufacturing Processes

NTNU

Kunnskap for en bedre verden